Experimental Study on the Confinement of Electron Plasma and Formation of Flow of Neutral Plasma in an Internal Conductor System

Directed by Prof. YOSHIDA Zensho

内部導体系における電子プラズマの閉じ込めと中性プラズマの流れ駆動に関する実験的研究

指導教官 吉田善章教授

Submitted to Department of Advanced Energy
Graduate School of Frontier Sciences, University of Tokyo
December 17, 2004 (Revised on March 3, 2005)

東京大学大学院新領域創成科学研究科
先端エネルギー工学専攻
平成 16 年 12 月 17 日提出（平成 17 年 3 月 3 日改訂）

学生証番号 27201 齋藤晴彦 (SAITOH Haruhiko)

概要

流れを持つ磁化プラズマの研究において，プラズマ流の動圧の効果により極めて高いβ値を実現し得る平衡状態（double Beltrami state）が理論的に予測され，その実験的検証を目指す基礎研究が行われている．こうした研究に必要とされる流れを駆動する方法として，dipole磁場中に閉じ込めた内部電場構造を持つプラズマのドリフト運動を利用する事が検討され，外部からの電子注入や電子損失によるプラズマの非中性化，あるいはバイアス電極を用いた内部電場形成に関する実験研究が進行中である．

また近年の原子物理学，粒子線源技術等の分野における学際的な研究の進展に伴い，陽電子や反陽子等を含む新しい荷電粒子の閉じ込めに関する活発な研究開発が進められている．このような特異な粒子群の挙動は，純粋なプラズマ物理学の観点から興味深いだけでなく，反物質粒子を含む各種原子等の合成やその応用を目指す上でも，その特性を明らかにする事が必要とされている．こうした多様な荷電粒子の良好な閉じ込めを実現する事を目的として，単一種類粒子から構成される非中性プラズマに留まらず，異なる符号を持つ荷電粒子群の同時閉じ込め配位の実現を目的とした研究が進められている．

トーラス系を用いた内部電場を持つプラズマの閉じ込め方式は，磁力線方向の静電ポテンシャルを使用しない，荷電粒子の安定な純磁場閉じ込めを実現する可能性を備えており，任意の非中性度を持つプラズマの閉じ込め配位の実現に向けた可能性が期待出来る．トーラス系における非中性プラズマ物理学の分野では，従来，純トロイダル磁場配位を用いた研究が行われてきたが，近年，トロイダル磁気面配位による非中性プラズマの閉じ込め方式が提案され，内部導体系やヘリカル系を用いた研究が進められている．上述のような，高速流を持つプラズマの平衡の探求や，あるいは各種荷電粒子の安定な閉じ込めを実現する上で，内部電場を持つ荷電粒子群の良好な閉じ込め配位を確立し，その基本的特性を実験的に明らかにする事は極めて重要である．

本論文では，内部導体型・トロイダル磁気面配位系であるProto-RT（Prototype-Ring Trap）装置において，内部自己電場を持つプラズマの研究を行った．まず，トロイダル純電子プラズマを使用して，磁気面配位における非中性プラズマの閉じ込め特性を明らかにする実験研究を行った．この段階の研究は，高速流を持つプラズマの平衡状態の検証を目指す一つの段階であると共に，また様々な荷電粒子群の安定な閉じ込め実現に向けた基礎研究としても位置付けられる．次に，これにより内部導体系の自己電場を持つプラズマの基本特性を明らか

にした上で，電極及び電子入射を用いた水素プラズマ中の電位勾配形成実験を行い，トロイダル磁気面配位における磁化プラズマ中の流れ駆動に関する基礎特性を明らかにする事を目指した．

純電子プラズマを使用した実験から，トロイダル磁気面配位においては，プラズマ内部の等ポテンシャル面と磁気面を近付ける事により，中性粒子との衝突による古典拡散時間に達する長時間に渡って非中性プラズマが閉じ込められる事が観測された．また，中性プラズマによる実験では，プラズマ内部で電極による負バイアスを与える事により，トロイダル方向にイオン音速を超えるプラズマ流が形成された．本研究を通して，トロイダル磁気面配位における非中性プラズマの閉じ込め特性及び，低プラズマ密度領域における径方向電場制御に関して基本的な理解が得られたものと考えられる．但し，現在のパラメータは静電的な領域に留まっており，流れの動圧の効果がプラズマの閉じ込め性能に与える影響の評価には至っていない．

Abstract

In the study of magnetized flowing plasmas, a new relaxation theory of high-β plasma that includes the effects of plasma flow (double Beltrami state) has recently been proposed. Experimental investigation for the equilibria of flowing plasmas is currently being conducted by using the drift motion of plasmas with internal electric field. As for the formation of electric field or flow inside the plasma, several methods are planned to be used, such as electron injection, loss of fast tail electrons, or electrode bias on the plasma.

Technologies for the confinement of charged particles are also attracting renewed interest in the fields of atomic and particle physics as well as in plasma physics. It is accompanied by the recent advances of the trap of exotic particles including anti-matters, such as positrons, anti-protons, and its mixtures aiming for the experiments of positron-electron plasma or creation of anti-atoms and high precision test for the CPT invariance. Several trap configurations are both theoretically and experimentally investigated, aiming at the simultaneous confinement of these multiple charges with different signs.

Toroidal geometries might be advantageous for the confinement of charged particles with arbitrary non-neutrality, because toroidal geometry uses no plugging electrostatic potential along the magnetic field lines, thus it has a potential ability to trap charged particles in a pure magnetic field. For the confinement of non-neutral plasmas in a toroidal geometry, several studies have been carried out using a pure toroidal magnetic field configuration. Recently, toroidal confinement of non-neutral plasmas in a magnetic surface configuration has been proposed, and experiments in internal conductor devices or helical systems are conducted or under construction. Realization of the stable confinement of plasmas with internal electric field is one of the essential issues for the investigation of the aforementioned advanced studies in plasma physics.

In this thesis, plasmas with internal electric field were investigated in a magnetic surface configuration. Confinement properties of non-neutralized plasma were tested using pure toroidal electron plasma in an internal conductor device Proto-RT (Prototype-Ring Trap). When the equi-potential contours of the plasma were adjusted to the magnetic surfaces, initial fluctuations of the plasma were damped, and stable confinement of toroidal electron plasma was realized. The obtained confinement time is sub-second order, and it is comparable to the classical diffusion time due to collisions with residual neutral gas in the present experiment. As well as applications for various kinds

of particle traps, this result may also be placed as one step toward the experimental investigation of flowing high β plasma in a toroidal geometry.

In neutral (hydrogen) plasma, formation of radial electric field and toroidal flow was demonstrated by means of electrode bias and electron injection. Although electric field or flow was successfully generated in the plasma, the obtained plasma parameters are still in the electrostatic regime, mainly due to the relatively low electron density of the present experiment.

Contents

List of Figures

List of Tables

Chapter 1

Introduction

1.1 Electromagnetic confinement of plasmas

Electromagnetic confinement of charged particles is one of the fundamental principles in plasma physics [1, 2] and atomic physics [3]. In the field of plasma sciences, magnetic trap of charged particles has been intensively studied especially aiming at thermonuclear fusion for power production [1] as well as various industrial applications [4]. Confinement of charged particles also plays fundamental role in the broad research areas of atomic physics, including the recent study of exotic particles like anti-matters [5–7,30]. Configurations for the electromagnetic confinement of charged particles are classified as open field system and closed toroidal system, as shown in Fig. 1.1. According to the total macroscopic charge of trapped particles, classification by the charge neutrality is also possible, as shown in the figure. Basic overview of several electromagnetic confinement methods of charged particles is described in this section.

1.1.1 Non-neutral plasmas in a linear geometry

The fundamental principle governing the magnetic trapping of a non-neutral plasma is the production of a spontaneous flow of particles in a magnetic field so that the self-electric field is neutralized in the co-moving frame. So-called “thermal equilibrium” may be achieved in a homogeneous magnetic field with the help of an appropriate external longitudinal electric field. This equilibrium is considered to be a relaxed state under the constraint on the canonical angular momentum of the rotation flow [8–10].

Vlasov-Maxwell description of plasmas

Behavior of collisionless plasmas can be treated by two levels of theoretical descriptions [2]. A fluid description is based on momentum-Maxwell equations, and both equilibrium and stability

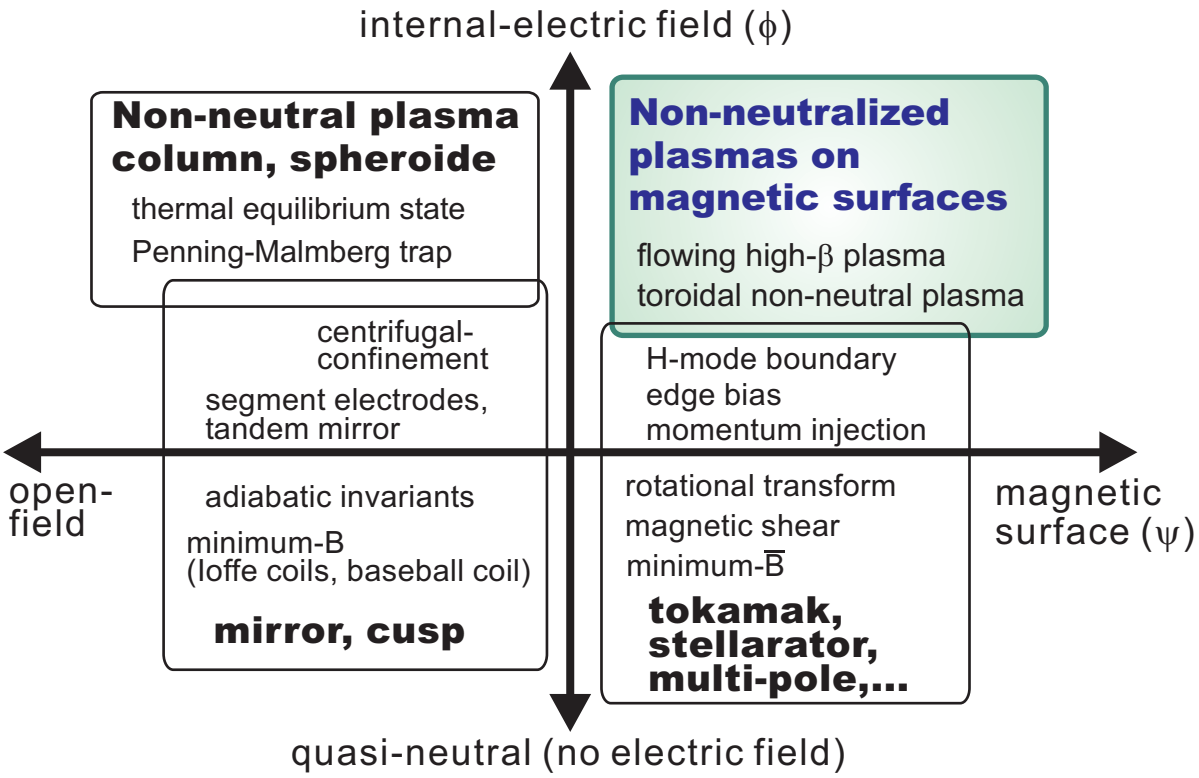

Figure 1.1: Diagram of various kinds of electromagnetic confinement of plasmas.

properties of plasmas can be discussed in a macroscopic scope. Especially when the plasma is cold, pressure gradient terms are neglected, and it leads to a rather simple closed description on number density: $n_\alpha(\mathbf{r},t)$, mean velocity: $\mathbf{v}_\alpha(\mathbf{r},t)$, mean electric field: $\mathbf{E}_\alpha(\mathbf{r},t)$, and mean magnetic field: $\mathbf{B}_\alpha(\mathbf{r},t)$ based on the continuity equation, equation of fluid motion, and Maxwell equations. Here α denotes the α-th component of the plasma, $\mathbf{r}$ is space coordinate, and t is time.

Another framework is a kinetic model based on Vlasov-Maxwell equations that directly includes the momentum-space distribution function of plasmas. Assuming that the plasma is collisionless (the time scale is shorter than typical collision time), Boltzmann equation reduces to Vlasov equation:

$$\frac{\partial f_\alpha(\mathbf{r},\mathbf{p},t)}{\partial t} + \mathbf{v}\cdot\nabla f_\alpha(\mathbf{r},\mathbf{p},t) + q_\alpha(\mathbf{E}+\mathbf{v}\times\mathbf{B})\cdot\frac{\partial f_\alpha(\mathbf{r},\mathbf{p},t)}{\partial \mathbf{p}} = 0. \tag{1.1}$$

Using Hamilton's equation of motion

$$\frac{d\mathbf{r}}{dt} = \frac{\partial \mathcal{H}}{\partial \mathbf{p}} \tag{1.2}$$

$$\frac{d\mathbf{p}}{dt} = -\frac{\partial \mathcal{H}}{\partial \mathbf{r}}, \tag{1.3}$$

it is seen that (1.1) is equivalent to Liouville's theorem for incompressible motion in the six di-

mensional phase space $(\mathbf{r},\mathbf{p})$:

$$\frac{\partial f}{\partial t} + [f,H] = 0. \tag{1.4}$$

Here

$$[u,v] \equiv \sum_i \left(\frac{\partial u}{\partial q_\mathrm{i}} \frac{\partial v}{\partial p_\mathrm{i}} - \frac{\partial u}{\partial p_\mathrm{i}} \frac{\partial v}{\partial q_\mathrm{i}} \right) \tag{1.5}$$

is Poisson bracket.

For equilibrium analysis, $\partial/\partial t = 0$ and steady state Vlasov equation is

$$\left[\mathbf{v}\cdot\nabla + q_\alpha \left(\mathbf{E}^0 + \mathbf{v}\times\mathbf{B}^0 \right) \cdot \frac{\partial}{\partial \mathbf{p}} \right] f_\alpha(\mathbf{r},\mathbf{p}) = 0. \tag{1.6}$$

Steady state electric field $\mathbf{E}^0(\mathbf{r},t)$ and magnetic field $\mathbf{B}^0(\mathbf{r},t)$ must be determined self-consistently from steady state Maxwell equations:

$$\nabla\cdot\mathbf{E}^0 = \frac{1}{\varepsilon_0} \left(\sum_\alpha q_\alpha \int d^3p\, f_\alpha^0 + \rho_\mathrm{ext} \right) \tag{1.7}$$

$$\nabla\cdot\mathbf{B}^0 = 0 \tag{1.8}$$

$$\nabla\times\mathbf{E}^0 = 0 \tag{1.9}$$

$$\nabla\times\mathbf{B}^0 = \mu_0 \left(\sum_\alpha q_\alpha \int d^3p\, \mathbf{v} f_\alpha^0 + \mathbf{j}_\mathrm{ext} \right), \tag{1.10}$$

where ρ_ext and $\mathbf{j}_\mathrm{ext}$ represents the external charge and current.

Axisymmetric rigid-rotor equilibrium

Equilibrium properties of collisionless plasmas are analyzed using Vlasov-Maxwell equations in an axisymmetric geometry. An infinitely long single component plasma in a uniform axial magnetic field is assumed as shown in Fig. 1.2, and $\partial/\partial\theta = \partial/\partial z = 0$. Electric field has only radial component and

$$\mathbf{E}^0(\mathbf{r}) = E_r^0(r)\hat{\mathbf{e}}_r. \tag{1.11}$$

Radial electric field is expressed as

$$E_r^0(r) = -\frac{\partial}{\partial r}\phi^0(\mathbf{r}), \tag{1.12}$$

using steady state electrostatic potential $\phi^0(\mathbf{r})$. Total equilibrium magnetic field including the effects of plasma current is given by

$$\mathbf{B}^0(\mathbf{r}) = B_0\hat{\mathbf{e}}_z + B_\theta(r)\hat{\mathbf{e}}_\theta + B_z(r)\hat{\mathbf{e}}_z. \tag{1.13}$$

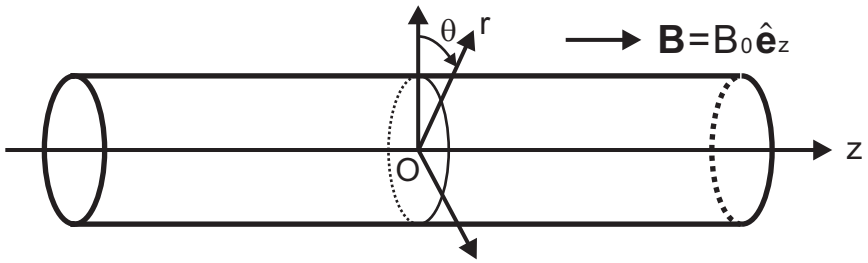

Figure 1.2: Axisymmetric infinite plasma column in a uniform axial magnetic field.

In the above representation of electromagnetic fields in the axisymmetric system, and by using equation of motion of the charged particle, Hamiltonian

$$\mathcal{H} = \frac{p_{\mathrm{r}}^2 + p_\theta^2 + p_{\mathrm{z}}^2}{2m} + q_\alpha \phi(\mathbf{r}) \tag{1.14}$$

and canonical momentum angular momentum

$$P_\theta = r p_\theta + q r A_\theta(r) \tag{1.15}$$

are single particle constants of the motion. When the plasma is assumed to be sufficiently low density, magnetic field is approximated as

$$\mathbf{B}^0(\mathbf{r}) \simeq B_0 \hat{\mathbf{e}}_z = \nabla \times \mathbf{A}_0(\mathbf{r}), \tag{1.16}$$

where $\mathbf{A}_0 = rB_0/2\hat{\mathbf{e}}_\theta$. Any distribution function $f_\alpha(\mathbf{r},\mathbf{p})$ that depends only on the single particle constants of the motion

$$f_\alpha^0(\mathbf{r},\mathbf{p}) = f_\alpha^0(\mathcal{H}, P_\theta) \tag{1.17}$$

is a solution of the steady state Vlasov-Maxwell equations.

Among these solutions, especially when f_α^0 is function of the linear combination of $\mathcal{H}$ and P_θ, $f_\alpha^0(\mathcal{H} - \omega P_\theta)$, shear-free rigid rotating solution is obtained.

$$v_\theta = \frac{\int d^3p v_\theta f_\alpha^0}{\int d^3p f_\alpha^0} = \omega r, \tag{1.18}$$

where ω gives the angular velocity around the z axis. When viscous forces act on shear flow in the plasma, the flow produces entropy and the system cannot be in the state of maximum entropy [9]. In rigid rotating non-neutral plasmas, states close to thermal equilibrium have been realized for both pure electron and ions, where the distribution function is given by

$$f_\alpha^0 = n_0 \left(\frac{m}{2\pi k_{\mathrm{B}} T}\right)^{3/2} \exp\left(-\frac{\mathcal{H} + \omega p_\theta}{k_{\mathrm{B}} T}\right), \tag{1.19}$$

$$\mathcal{H} + \omega p_\theta = \frac{m}{2}(v_\theta + \omega r)^2 + q\phi - \frac{m r^2 \omega^2}{2} + \frac{qB\omega r^2}{2}. \tag{1.20}$$

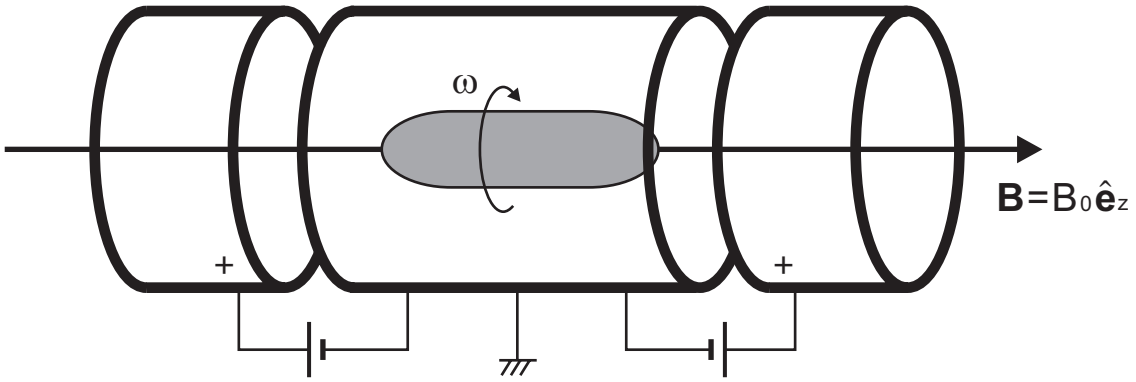

Figure 1.3: Penning-Malmberg trap for positive charged particles.

Malmberg-Penning traps

In contrast to neutral plasmas, plasmas with a single sign of charge can be trapped for a long time in static electric and magnetic fields [2, 9, 10]. Malmberg-Penning trap is the most generally used device for the confinement of non-neutral plasmas. As shown in Fig. 1.3, charged particles are confined in a uniform axial magnetic field $\mathbf{B} = B_0\hat{\mathbf{e}}_z$ and electrostatic fields in z direction generated by plugging electrodes. Here (r,θ,z) is a cylindrical coordinate and the device axis is set as the z-axis. Charged particles feel repulsive forces in the radial direction due to the self-electric field, pressure, and centrifugal forces, and these outgoing forces are balanced by the Lorentz force $e\mathbf{v}\times\mathbf{B}$ when charged particles rotate around the z-axis with velocity $\mathbf{v} = r\omega\hat{\mathbf{e}}_\theta$. The particles do not feel net radial electromagnetic forces in the rotating frame, and thus rotation in the magnetic field may be considered as neutralization of self electrostatic potential.

Assuming that the total energy of the confined particles is conserved and that the trap geometry is cylindrically symmetric, Hamiltonian $\mathcal{H}$ and canonical angular momentum P_θ are constants of the motion of the system. When $\mathcal{H}$ is conserved, axial confinement of the particles is realized by applying sufficiently high voltage on the plugging electrodes. On the other hand, conservation of P_θ warrants the radial confinement of non-neutral plasmas. The total canonical angular momentum of the system is given by

$$P_\theta = \sum_i (mr_{\rm i}v_{\theta{\rm i}} + er_{\rm i}A_\theta) = \sum_i (r_{\rm i}p_{\theta{\rm i}} + er_{\rm i}A_\theta), \tag{1.21}$$

where $p_{\rm i}$ is the mechanical angular momentum of each particle, and sum is over the all particles in the system. When diamagnetic effects are neglected (which can be applied to low density and low velocity non-neutral plasmas), θ-component of the vector potential solely consists of the external field: $A_\theta = B_0 r/2$. In a strong magnetic field, mechanical angular momentum can be neglected,

and the conservation of the total canonical angular momentum reduces to

$$P_\theta \simeq \frac{eB_0}{2}\sum_i r_{\mathrm{i}}^2 = const. \tag{1.22}$$

The conservation of $\sum r_{\mathrm{i}}^2$ imposes strong constraint on the radial expansion or compression of non-neutral plasmas in the Penning-Malmberg trap. In contrast, when plasma consists of multiple species, the conservation of P_θ leads to $\sum q_{\mathrm{i}} r_{\mathrm{i}}^2 = const.$, and thus quasi-neutral plasmas are not easily confined in a finite region.

In real experiments, Hamiltonian $\mathcal{H}$ and canonical angular momentum P_θ of the system are not perfectly time independent. The effects of asymmetric experimental configuration, radiation from charged particles in acceleration motions, collisions of plasmas with neutrals, etc. lead to the dissipation of $\mathcal{H}$ and P_θ of trapped plasmas. Another problem is the image charge effects caused by the finite device length in the conventional Malmberg-Penning traps [11]. Due to the many experimental techniques, including the compensation of the slowly damping torque of the plasma by a "rotating wall" external electric field [12], the use of multi-ring electrodes and formation of spheroidal plasmas [11], together with the use of ultra-high vacuum and precisely aligned symmetric field and device geometry, extremely long confinement of non-neutral plasmas has been realized in linear devices.

As well as experiments on the diverse fundamental properties of non-neutral plasmas [9], the linear devices also play important roles in various scientific applications in the fields of both plasma physics and atomic physics. Among these topics, linear traps for non-neutral plasmas are applied to the confinement and production of anti-matters [5–7, 13–19]. Deceleration and capture of antiprotons was demonstrated in a Penning trap [13]. Confinement of positron plasma was realized in liner geometry [14, 15] and interactions between electron beam and positron plasma [16, 17] were investigated. Aiming at the production of antimatter atoms and other composition of matter and antimatters [18], simultaneous confinement of low energy antiprotons and positrons was studied [19], and recent years, production of large number of anti-hydrogen atoms [5, 6] and slow antiproton beam [7] were successfully demonstrated. In linear devices, nested potential profile are generated by multi-ring electrodes for the realization of the interaction between charges of different sign, and small amount of each charged particles are overlapped to synthesize antimatter atoms.

1.1.2 Open field geometry for the trap of charged particles

Magnetic mirror

Assuming static and inhomogeneous magnetic field primarily pointed in z direction, and when the field is axisymmetric ($\partial/\partial\theta = 0$), $\mathbf{B}$ has two finite components of B_{r} and B_{z}, which satisfies

$$\nabla\cdot\mathbf{B} = \frac{1}{r}\frac{\partial}{\partial r}(rB_{\mathrm{r}}) + \frac{\partial B_{\mathrm{z}}}{\partial z} = 0, \tag{1.23}$$

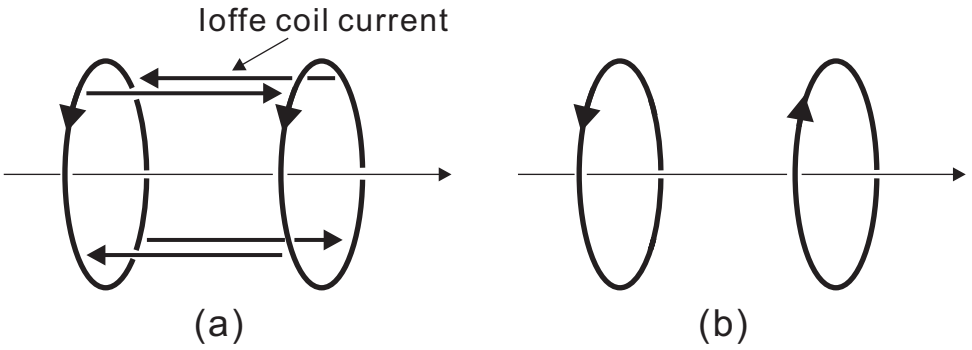

Figure 1.4: (a) Magnetic mirror and (b) cusp coil currents.

and radial field is approximated as

$$B_{\mathrm{r}} = -\frac{r}{2}\left(\frac{\partial B_{\mathrm{z}}}{\partial z}\right)\bigg|_{r=0}. \tag{1.24}$$

The axial component of the Lotrentz force is then

$$F_{\mathrm{z}} = -qv_\theta B_{\mathrm{r}} = \frac{qv_\theta B_{\mathrm{r}}}{2}\frac{\partial B_{\mathrm{z}}}{\partial z}. \tag{1.25}$$

For a particle whose guiding center is on the z axis, where $v_\theta = const.$,

$$F_{\mathrm{z}} = m\frac{dv_\perp}{dt} = -\mu\frac{\partial B_{\mathrm{z}}}{\partial z}, \tag{1.26}$$

where μ is the magnetic moment of the gyro-rotating particle defined as

$$\mu \equiv \frac{mv_\perp^2}{2B}. \tag{1.27}$$

Multiplying $v_\parallel$,

$$\frac{d}{dt}\left(\frac{1}{2}mv_\parallel^2\right) = -\mu\frac{\partial B}{\partial z}\frac{dz}{dt} = \mu\frac{dB}{dt}. \tag{1.28}$$

On the other hand, from conservation of the energy of the particle,

$$\frac{d}{dt}\left(\frac{1}{2}mv_\parallel^2 + \frac{1}{2}mv_\perp^2\right) = \frac{d}{dt}\left(\frac{1}{2}mv_\parallel^2 + \mu B\right) = 0. \tag{1.29}$$

Combining Eqs. (1.28) and (1.29),

$$-\mu\frac{dB}{dt} + \frac{d}{dt}(\mu B) = 0, \tag{1.30}$$

and thus μ is invariant:

$$\frac{d\mu}{dt} = 0. \tag{1.31}$$

When the energy of the particle satisfies

$$W = \frac{1}{2}mv_{\parallel}^2 + \mu B(z) < \mu B_{\max}, \tag{1.32}$$

where $B_{\max}$ is the maximum strength of the field at the "throat" in Fig. 1.4 (a), $v_{\parallel}$ becomes 0 before reaching the "throat", and charged particles are confined in the magnetic mirror. Taking the field strength at the midplane $B_{\min}$ and pitch angle θ_0, Eq. (1.32) is

$$\theta_0 > \sin^{-1}\left(\frac{B_{\min}}{B_{\max}}\right)^{1/2}, \tag{1.33}$$

indicating that particles with large $v_{\parallel}$ (in the loss cone) are not mirror trapped [20]. In the open field devices, magnetic field lines inevitably intersect the device walls, and reduction of these end loss must be considered.

Stable condition for MHD instability (flute instability) [1] is given by

$$\delta \int \frac{dl}{B} < 0, \tag{1.34}$$

and because the field lines of the mirror is concave toward the plasma near the midplane, the conventional mirror configuration is not stable for the flute instability. In order to produce minimum B field (field lines are convex toward the plasmas), Ioffe bar coils (Fig. 1.4 (a)) or "baseball" coils are used, while the axisymetry of the system is destroyed [20]. When the direction of one coil current is reversed, as shown in Fig. 1.4 (b), minimum B cusp configuration is generated. Although a plasma in a cusp configuration has better stability, B vanishes at the center of the device, and μ is not conserved, resulting a large particle loss from line and point cusps.

Confinement of charged particles in the transverse direction is realized due to the second adiabatic invariant (the longitudal invariant)

$$J = \int v_{\parallel} ds, \tag{1.35}$$

where ds is taken along a magnetic field line. When a particle is confined between two magnetic mirrors and reflected at two turning points a and b,

$$J = \int_a^b v_{\parallel} ds, \tag{1.36}$$

and it determines the length of the field line between the turning points. Because no two field lines have the same length between positions of the same $|B|$, the particle returns to the same line of force as it rotates around the center axis of the mirror field.

Plasmas in mirror devices

In the experiments at tandem Mirror machines, creation of thermal barrier and formation of plugging potential have been conducted and end-loss reduction of the trapped ions was demonstrated at *GAMMA 10* [21]. Applying electrode bias by the concentric electrode plate at the end of the mirror, the effects of radial electric field on the transport properties were also studied [22].

Aiming for advanced fusion concepts, creation of fast plasma flow and test for the centrifugal confinement is conducted [23–26] in modified mirror device *Maryland Centrifugal Experiment*. In this experiment, an axial bias electrode is installed as a center core of a mirror device, and flow is induced in the $\mathbf{E}\times\mathbf{B}$ direction. The resultant centrifugal force is expected to reduce the end loss of plasmas, and also the generated velocity is effective for the stabilization and heating of the confined plasmas. Spectroscopic measurements was done for the plasma rotation, and creation of the flow of Mach numbers of 1-2 is realized [25].

As well as neutral plasmas, non-neutral plasmas are also trapped in varying magnetic field [27–30]. Equilibrium properties [27], enhancement of the particle transport due to the addition of quadrupole field [28] were studied, and the use of higher-order multipole magnetic field for the anti-matter atoms [29] are proposed. The use of trap consists of a magnetic cusp and an electric octupole for the creation of antihydrogen [30] is also considered.

1.1.3 Toroidal confinement of plasmas

In contrast to the linear devices, toroidal traps can produce closed magnetic field lines inside the device geometry. In the study of high temperature fusion plasmas in toroidal devices, confinement of plasmas is realized by the combination of coil currents and internal plasma currents (tokamaks) or only by external coil currents (stellarators, multi pole devices). In tokamaks, toroidal magnetic field B_ϕ is inhomogeneous ($\propto 1/R$) and when plasma consists of ions and electrons, the resultant ∇B drift induces vertical charge separation. In a simple torus with pure toroidal field, the generated electric field causes the radially outgoing $\mathbf{E}\times\mathbf{B}$ drift of charged particles, and plasmas are not confined. Thus poloidal field B_θ is generated by means of toroidal plasma current (rotational transform), and magnetic field lines are modified to form closed magnetic surfaces [1].

Orbit motion in a magnetic surface

Magnetic surfaces are defined as $\psi(\mathbf{r})$ planes, where magnetic field lines lie on $\psi(\mathbf{r}) = const.$ and thus

$$\nabla\psi(\mathbf{r})\cdot\mathbf{B} = 0 \tag{1.37}$$

is satisfied. Toroidal symmetry of the magnetic field configuration warrants the analytic representation of the magnetic surfaces as

$$\psi = rA_\theta(r,z) = const. \tag{1.38}$$

and poloidal field is calculated by

$$B_\mathrm{r} = -\frac{1}{r}\frac{\partial\psi}{\partial z} \text{ and } B_\mathrm{z} = \frac{1}{r}\frac{\partial\psi}{\partial r}, \tag{1.39}$$

which satisfies Eq. (1.37).

The Lagrangian equation of the motion of a charged particle in a magnetic field **B** and an electric field **E** is given by

$$\frac{d}{dt}\left(\frac{\partial\mathcal{L}}{\partial\dot{q}_\mathrm{i}}\right) - \frac{\partial\mathcal{L}}{\partial q_\mathrm{i}} = 0\,, \tag{1.40}$$

where

$$\mathcal{L} = \frac{mv^2}{2} + q\mathbf{v}\cdot\mathbf{A} - q\phi. \tag{1.41}$$

Here **A** is vector potential of **B**: $\mathbf{B} = \nabla\times\mathbf{A}$ and ϕ is scalar potential of **E**: $\mathbf{E} = \nabla\phi$, and **q** is the coordinate of the charged particle. In a toroidaly symmetric configuration ($\partial\mathcal{L}/\partial\theta = 0$), the canonical angular momentum of the charged particle satisfies

$$p_\theta \equiv \frac{\partial\mathcal{L}}{\partial\dot{\theta}} = mr^2\dot{\theta} + qrA_\theta = const. \tag{1.42}$$

The variation of ψ at a distance d from ψ at the initial point is given by

$$|\delta\psi| = d|\nabla\psi|, \tag{1.43}$$

and by using Eq. (1.42), d is calculated as

$$d = \left|\frac{m\delta(rv_\theta)}{q|\nabla\psi|}\right|. \tag{1.44}$$

From Eqs. (1.38) and (1.39), $|\nabla\psi| = r(B_\mathrm{r}^2 + B_\mathrm{z})^{1/2} = rB_\mathrm{p}$ and also assuming that $\delta(rv_\theta) <\sim rv_\theta$, the maximum value of d is given by

$$d \le \left|\frac{mr\dot{\theta}}{qB_\mathrm{p}}\right| \equiv r_{Lp}, \tag{1.45}$$

indicating that the deviation of the charged particle from one magnetic surface is less than the poloidal Larmor radius r_{Lp}. When the Hamiltonian of the charged particle

$$\mathcal{H} = -\mathcal{L} + \sum_i p_\mathrm{i}\dot{q}_\mathrm{i} = -\frac{1}{2m}(\mathbf{p} - q\mathbf{A})^2 + q\phi \tag{1.46}$$

is not explicitly time dependent, the total energy of the charged particles is conserved:

$$W = \frac{mv^2}{2} + q\phi = const. \tag{1.47}$$

and v has an upper limit of $v \leq (2(W - q\phi)/m)^{1/2}$, and thus, as long as the poloidal field lines form closed magnetic surfaces in a finite region, the orbits of charged particles are also limited to a finite region.

Due to the toroidal effects, some of charged particles in a toroidal geometry undergo magnetic mirror reflection, and trapped in the mirror. The orbit of these particles take "banana"-like trajectories, and when collisional processes are considered, it leads to the enhancement of the transport (neoclassical transport) [1].

1.1.4 Toroidal confinement of non-neutralized plasmas

In contrast to the linear devices, toroidal configurations use no electric fields along the magnetic field lines, and it has a potential ability to confine charged particles at any degree of non-neutrality. It thus becomes possible to trap high-energy beam particles, or to confine multiple species of different charges. Studies on non-neutral plasmas regarding pure toroidal magnetic fields [31–51] have revealed an interesting equilibrium state, one is in marked contrast to the confinement of a neutral plasma, which requires twists (rotational transforms) of magnetic field lines in order to avoid the drift loss of particles.

In the drift orbit approximation, the total energy of a charged particle in a toroidal magnetic field is

$$E = q\phi + \frac{\mu_0 B_0 R_0}{R} + \frac{{L_z}^2}{2mR} + \frac{m(\nabla\phi)^2}{2B^2}, \tag{1.48}$$

where q is charge, ϕ is the electrostatic potential, R_0 is the major radius, B_0 is the magnetic field strength at $R = R_0$, μ_0 is the space permeability, L_z is the angular momentum of the particle around z axis, and m is the particle mass. Because the total energy of each particle is conserved, surfaces defined by $E = const.$ constrain the positions of the guiding center of the particles. When there is no electric field (neutral plasmas), Eq. (1.48) becomes

$$E = \frac{\mu_0 B_0 R_0}{R} + \frac{{L_z}^2}{2mR} \propto 1/R, \tag{1.49}$$

and the guiding center motions are on cylinders, which inevitably intersects the boundary wall of a containing chamber. In non-neutral plasmas, however, due to the strong radial electric field caused by the space and image charges, $E = const.$ surfaces can take closed circular shape in the poloidal cross section of the torus. The particles might also take closed orbits in a pure toroidal field undergoing the poloidal $\mathbf{E}\times\mathbf{B}$ rotation [32]. Non-neutral plasmas in pure toroidal magnetic fields were analyzed by the early work of Dougherty and Levy [32]. They showed that in a conducting toroidal vessel, the particles can take closed orbits due to the $\mathbf{E}\times\mathbf{B}$ rotation, which is inward-shifted from the equipotential contours because of the other first order drifts. By substituting $\mathbf{E}\times\mathbf{B}$ drift speed $\mathbf{v} = -\nabla\phi\times\mathbf{B}/B^2$ into the steady state continuity equation $\nabla\cdot(n\mathbf{v}) = 0$, we have

$$\left[\nabla\phi\times\nabla\left(\frac{n}{B^2}\right)\right]\cdot\mathbf{B} = 0. \tag{1.50}$$

When electric and magnetic fields and plasmas are axisymmetric, Eq. (1.50) implies that

$$\frac{n}{B^2} = f(\phi). \tag{1.51}$$

By using Eq. (1.51), one can solve Poisson's equation

$$\nabla^2\phi = -\frac{nq}{\varepsilon_0} \tag{1.52}$$

in order to obtain equilibrium potential and density profiles of toroidal non-neutral plasmas.

An electrostatic force balance equilibrium model, including the effects of the space and image charges, was also studied [40]. Toroidal electron plasmas feel repulsive "hoop force" caused by the self electric field and also by the diamagnetic effects, and the confinement can be achieved by the external radial electric fields due to the image charges on the vessel wall or electrodes. They also showed the applied electric fields can control the stability and frequency of the $l = 1$ diocotron mode. Concerning the fluid equilibrium of toroidally confined non-neutral plasmas, an inviscid model was studied by Turner [48, 49], and the existence of the equilibrium and the interesting properties of the equilibrium, like the possibility of the confinement of dense plasmas over the Brillouin limit were demonstrated. Stability [50], and transport [51] properties of toroidal non-neutral plasmas were also theoretically studied.

The early experimental investigations on toroidal non-neutral plasmas aimed at storage or acceleration of heavy ions [33] or creation of high-current relativistic electron beams [11, 37] in a pure toroidal magnetic field configuration. Toroidal effects, electron injection methods, and other collective behaviors of electron plasma were studied in a series of experiments in low-aspect-ratio torus devices [41–43]. Existence of the equilibrium of electron plasma in pure toroidal field was demonstrated in these experiments, and recently, stabilization of $m = 1$ diocotron mode and realization of long time confinement of toroidal electron plasma were demonstrated in a "partial" torus device using an electrostatic feedback system [47].

1.1.5 Magnetic surfaces for non-neutral plasmas

In recent years, it has been recognized that the toroidal geometries might be suitable for the various kinds of non-neutral plasmas [52, 53], such as the mixtures of antimatters [54] or streaming non-neutralized plasmas for the investigation of new relaxation states of plasmas with strong flow [52]. In these experiments, magnetic surface configurations [52–64] are employed for the confinement of non-neutral plasmas, because it is expected to show excellent confinement properties, as well-known in the devices for fusion plasmas (motions of charged particle in magnetic surfaces are described in the previous section).

The force balance equation of single component non-neutral plasma is

$$mn\left(\frac{\partial \mathbf{v}}{\partial t} + \mathbf{v}\cdot\nabla\mathbf{v}\right) = qn(\mathbf{v}\times\mathbf{B} - \nabla\phi) - \nabla p. \tag{1.53}$$

When the density of non-neutral plasmas is far below the Brillouin limit

$$n_{\mathrm{B}} = \frac{\varepsilon_0 B^2}{2m}, \tag{1.54}$$

and the pressure term is negligibly smaller than the electromagnetic forces, the equation of motion reduces to

$$qn(\mathbf{v}\times\mathbf{B} - \nabla\phi) = 0. \tag{1.55}$$

By taking the scalar product of Eq. (1.55) and **B**,

$$\mathbf{B}\cdot\nabla\phi = 0, \tag{1.56}$$

indicating that the electrostatic potential is constant on a magnetic field line. From Eq. (1.55), the perpendicular velocity of the fluid is given by the $\mathbf{E}\times\mathbf{B}$ drift speed

$$\mathbf{v} = -\frac{\nabla\phi\times\mathbf{B}}{B^2}, \tag{1.57}$$

and the strong self electric field of non-neutral plasmas induces fast cross-field transport of charged particles on a magnetic surface. Thus in cold non-neutral plasmas, electrostatic potential ϕ is a function of magnetic flux ψ

$$\phi = \phi(\psi). \tag{1.58}$$

When the temperature of the plasma is also a function of magnetic flux ψ, the density in the equilibrium state is given by

$$n = N(\psi)\exp\frac{e\phi}{k_{\mathrm{B}}T_{\mathrm{e}}(\psi)}, \tag{1.59}$$

and one may solve Poisson's equation

$$\nabla^2\phi = \frac{1}{\varepsilon_0}N(\psi)\exp\frac{e\phi}{k_{\mathrm{B}}T_{\mathrm{e}}(\psi)} \tag{1.60}$$

to obtain equilibrium potential and density profiles [54].

Although several theoretical works including the equilibrium [54] and the stability [60] have been carried out, little is known about the experimental issues on the confinement properties of the non-neutral plasmas in the magnetic surface configuration. Closed magnetic surfaces can be produced by a ring conductor hung in a vacuum vessel [52]. One may use a super-conducting levitated ring to eliminate mechanical structures and current feeds that degrade particle confinement [53]. A helical device is another solution to produce closed magnetic surfaces with only "external" windings [54]. At present, experiments of toroidal non-neutral plasmas on internal conductor devices [52, 53], a stellarator [54], and a helical system [61–64] are in progress or under construction. Ignoring the mechanical momentum of a particle, the particle orbit may be restricted on a corresponding magnetic surface, as far as the canonical momentum is conserved. This is the common mechanism of particle confinement in magnetic surface configurations, which also applies to usual neutral plasmas, and is also a natural extension of the above-mentioned "thermal equilibrium" under the constraint on the canonical momentum [53].

1.1.6 Hall MHD and high β plasma with strong flow

Including the finite pressure terms, equations of motion for electrons and ions are

$$\frac{\partial}{\partial t}\mathbf{v}_\mathrm{e} + (\mathbf{v}_\mathrm{e}\cdot\nabla)\mathbf{v}_\mathrm{e} = -\frac{e}{m_\mathrm{e}}(\mathbf{E}+\mathbf{v}_\mathrm{e}\times\mathbf{B}) - \frac{1}{m_e n}\nabla p_\mathrm{e}, \tag{1.61}$$

$$\frac{\partial}{\partial t}\mathbf{v}_\mathrm{i} + (\mathbf{v}_\mathrm{i}\cdot\nabla)\mathbf{v}_\mathrm{i} = \frac{e}{m_\mathrm{i}}(\mathbf{E}+\mathbf{v}_\mathrm{i}\times\mathbf{B}) - \frac{1}{m_i n}\nabla p_\mathrm{i}. \tag{1.62}$$

When the small inertia term of electrons can be neglected, Eq. (1.61) reduces to

$$\mathbf{E}+\mathbf{v}_\mathrm{e}\times\mathbf{B} + \frac{1}{m_e n}\nabla p_\mathrm{e} = 0. \tag{1.63}$$

Using the relation on the electric field $\mathbf{E} = -\partial\mathbf{A}/\partial t - \nabla\phi$ and current density $\mathbf{j} = e(\mathbf{v}-\mathbf{v}_\mathrm{e}) = 1/\mu_0\nabla\times\mathbf{B}$, where $\mathbf{v} = (m_\mathrm{e}\mathbf{v}_\mathrm{e} + m_\mathrm{i}\mathbf{v}_\mathrm{i})(m_\mathrm{e}+m_\mathrm{i}) \simeq \mathbf{v}_\mathrm{i}$, Eqs. (1.63) and (1.62) become

$$\partial_\mathrm{t}\mathbf{A} = (\mathbf{v}-\nabla\times\mathbf{B})\times\mathbf{B} - \nabla(-\phi+\varepsilon p_\mathrm{e}) \ \text{ and} \tag{1.64}$$

$$\partial_\mathrm{t}(\varepsilon\mathbf{v}+\mathbf{A}) = \mathbf{v}\times(\mathbf{B}+\varepsilon\nabla\times\mathbf{v}) - \nabla(\varepsilon v^2/2 + \phi + \varepsilon p_\mathrm{i}). \tag{1.65}$$

Here length is normalized by ion skin depth $l_\mathrm{i} = c/\omega_\mathrm{ci}$, time t by ion cyclotron time $1/\omega_\mathrm{ci}$, velocity v by Alfvén velocity $v_A = B_0/(\mu_0 Mn)^{1/2}$, pressure p by magnetic pressure B_0^2/μ_0, and $\varepsilon = l_\mathrm{i}/L_0$ is a measure of the ion skin depth, where L_0 and B_0 are typical length and magnetic field scales. From Eqs. (1.64) and (1.65), Hall MHD equations are derived:

$$\partial_\mathrm{t}\mathbf{v} + (\mathbf{v}\cdot\nabla)\mathbf{v} = (\nabla\times\mathbf{B})\times\mathbf{B} - \nabla p, \tag{1.66}$$

$$\partial_\mathrm{t}\mathbf{B} = \nabla\times[(\mathbf{v}-\varepsilon\nabla\times\mathbf{B})\times\mathbf{B}]. \tag{1.67}$$

When $\varepsilon = 0$ and Hall term is neglected, Eqs. (1.66) and (1.67) become standard MHD equations.

Hall MHD Equations (1.66) and (1.67) are represented as

$$\frac{\partial}{\partial t}\mathbf{\Omega}_\mathrm{i} - \nabla\times(\mathbf{U}_\mathrm{i}\times\mathbf{\Omega}_\mathrm{i}) = 0 \ \ (j=1,2) \ , \tag{1.68}$$

where $\mathbf{\Omega}_1 = \mathbf{B}$, $\mathbf{U}_1 = \mathbf{v}-\nabla\times\mathbf{B}$ and $\mathbf{\Omega}_2 = \mathbf{B}+\nabla\times\mathbf{v}$, $\mathbf{U}_2 = \mathbf{v}$. One of the time-independent solution of Eq. (1.68) is given by

$$\mathbf{U}_\mathrm{i} = \mu_\mathrm{j}\mathbf{\Omega}_\mathrm{i} \ \ (j=1,2) \ \text{ or} \tag{1.69}$$

$$\mathbf{B} = a(\mathbf{v}-\nabla\times\mathbf{B}) \ \text{ and } \ \mathbf{B}+\nabla\times\mathbf{v} = b\mathbf{v}. \tag{1.70}$$

When compared with Eqs. (1.64) and (1.65), the time independent solution satisfies

$$v^2/2 + p_\mathrm{i} + \phi = const., \tag{1.71}$$

$$p_\mathrm{i} - \phi = const., \tag{1.72}$$

Taking the sum of Eqs. (1.71) and (1.72), the β value and ion flow velocity v is related as

$$\beta + v^2 = const.. \tag{1.73}$$

Assuming that $\beta = 0$ at the plasma surface and v is given by $\mathbf{E} \times \mathbf{B}$ speed, the relation between β value and radial electric field E_r is

$$E_\mathrm{r}/B = v_\mathrm{A}\beta^{1/2}. \tag{1.74}$$

Thus ultra-high β (possibly $\beta > 1$) equilibrium state of flowing plasma is predicted owing to the two fluid effects [65–68]. In order to obtain the beta value of $\beta = 1$ in hydrogen plasma of electron density $n_\mathrm{e} = 10^{17}$ m^{-3} with magnetic field $B = 0.01$ T, required electric field strength is $E_\mathrm{r} = 7$ kVm^{-1}.

As **v** and **B** are written using Clebsch potentials

$$\mathbf{v} = \nabla\phi \times \nabla z + v_\mathrm{z} \times \nabla z, \tag{1.75}$$

$$\mathbf{B} = \nabla\psi \times \nabla z + B_\mathrm{z} \times \nabla z, \tag{1.76}$$

Eqs. (1.66) and (1.67) can be rewritten as

$$-\partial_\mathrm{t}(\Delta\phi) + \{\phi, -\Delta\phi\} - \{\psi, -\Delta\psi\} = 0, \tag{1.77}$$

$$\partial_\mathrm{t} v_\mathrm{z} + \{\phi, v_\mathrm{z}\} - \{\psi, \varepsilon B_\mathrm{z}\} = 0, \tag{1.78}$$

$$\partial_\mathrm{t}\psi + \{\phi - \varepsilon B_\mathrm{z}, \psi\} = 0, \tag{1.79}$$

$$\partial_\mathrm{t} B_\mathrm{z} + \{\phi, \varepsilon B_\mathrm{z}\} - \{v_\mathrm{z} + \Delta\psi, \psi\} = 0, \tag{1.80}$$

where { } is the Poisson bracket defined as

$$\{a, b\} = (\partial_y a)(\partial_x b) - (\partial_x a)(\partial_y b). \tag{1.81}$$

In the steady state, Eq. (1.79) becomes

$$\{\phi - \varepsilon B_\mathrm{z}, \psi\} = 0, \tag{1.82}$$

indicating that

$$\phi - \varepsilon B_\mathrm{z} = f(\psi). \tag{1.83}$$

In the standard MHD, $\phi = f(\psi)$ is always satisfied as $\varepsilon = 0$, but toroidal magnetic field induces the disagreement of the contours of ϕ and ψ when the two fluid effects are not negligible [69, 70].

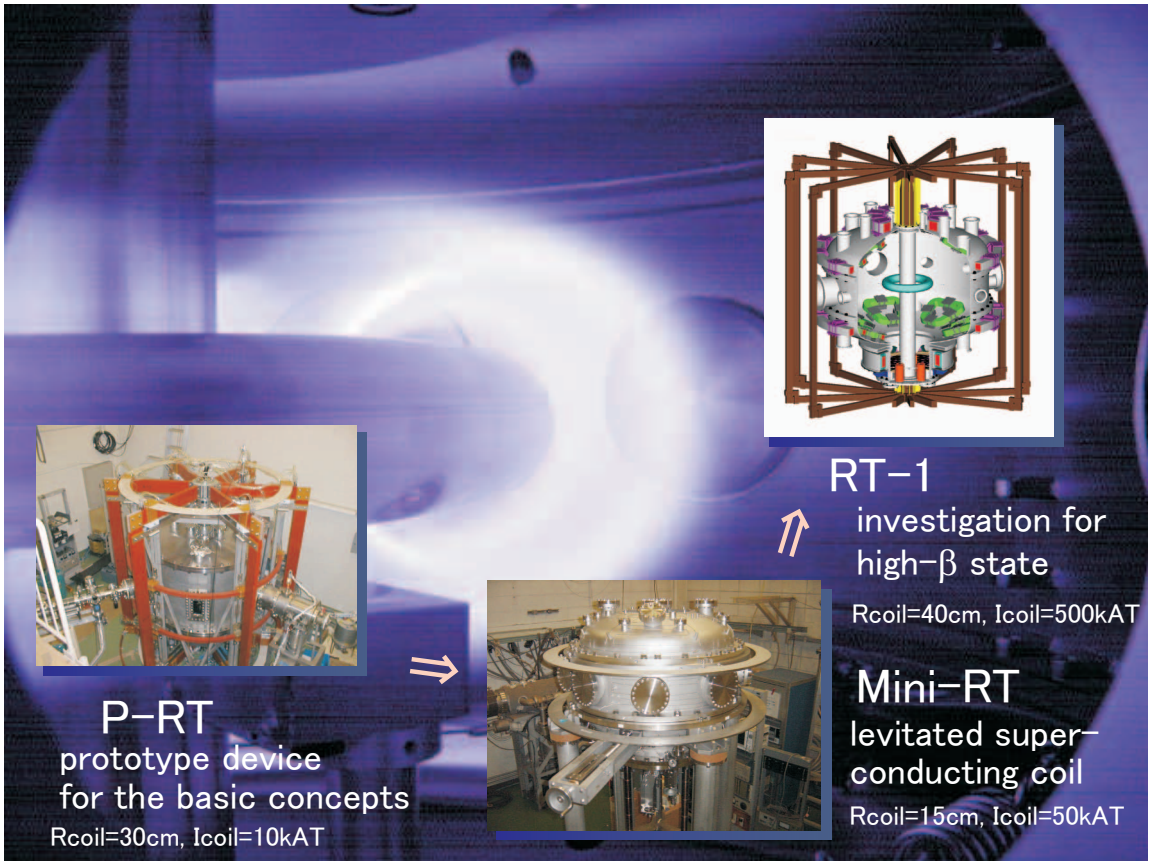

Figure 1.5: Experiments of flowing high β plasma in internal conductor devices [52, 53].

1.2 Proto-RT project and objective of the present study

As described in the previous section, the effects of electric field and flow play important role in the fundamental properties of plasmas, and it is one of the main subjects in the study of fusion, space, and planetary magnetospheric plasmas. The formation of transport barrier at the edge region of the plasma and improvement of the confinement properties have been intensively studied in tokamaks [71, 72], stellarators [73, 74], mirror machines [21], or heliac [75].

Recently, the study of plasmas with flow in the entire region is developing, such as centrifugal confinement of rotating plasmas [24] or new relaxation states of plasmas [66, 67] (represented by Double Beltrami fields [65]) that includes the effects of plasma flow. In the new relaxation theory of two-fluid plasma developed by Mahajan and Yoshida, ultra-high β (possibly $\beta > 1$) equilibrium state of flowing plasma is predicted.

In experimental search for the relaxation states of flowing plasmas, toroidal trap devices equipping a normal-conducting or superconducting internal coil [52, 53] are constructed and fundamental research is currently being carried out. When a radial electric field is generated in the internal conductor device, toroidal plasma flow is induced due to the drift motion of charged particles.

Thus mechanism of the formation of internal potential gradient and confinement properties of non-neutralized plasmas are essential issues for the study of flowing plasmas.

Non-neutral plasmas on magnetic surfaces have various kinds of scientific applications, especially in the study of flowing plasmas. The purpose of this thesis is to examine the basic properties of plasmas with internal electric field in an internal conductor device Proto-RT (Prototype-Ring Trap). In terms of the confinement properties, pure electron plasma was trapped in Proto-RT and control of the potential structures was carried out. Two-dimensional potential profiles were measured, and effects of the relation between equi-potential contours and magnetic surfaces on the confinement properties were tested. As for the control of the potential profiles in two-fluid plasmas, hydrogen plasma was used for the examination on the formation of radial electric field. As noted in the previous section, one of the most important experimental parameters of both non-neutral and neutral plasmas is the electrostatic potential structures. In this study, two-dimensional potential profiles of plasmas are measured using a Langmuir probe array in the internal conductor device. Experimental setup and obtained results are explained in the following sections.

Chapter 2

Apparatus and experimental setup

The experiments in this study were conducted at Proto-RT (Prototype-Ring Trap) device [52, 53, 79–84]. Descriptions concerning the apparatus, including the device setup, formation of plasmas, electron injection, and diagnostics are explained in this chapter.

2.1 The Proto-RT device

The Prototype-Ring Trap is an internal conductor device constructed in 1998 for the study of physics related to non-neutral plasmas [52, 85], chaos-induced resistivity of collisionless plasma and its application to low-gas-pressure plasma sources [86–88], and experimental investigation of ultra-high β plasma with fast flow [65, 66]. Overall descriptions on the device setup and plasma formation methods are described in this subsection. More comprehensive objective of the Proto-RT project and details of the machine can be found in references [52, 53, 79–84].

2.1.1 Vacuum chamber and field coils

The bird-eye view and photograph of Proto-RT are given in Fig. 2.1 and Fig. 2.2. Proto-RT consists of a cylindrical chamber, three kinds of magnetic field coils, vacuum pumps, and other diagnostic apparatus connected to the main chamber.

Vacuum chamber

The top view and toroidal cross section of the Proto-RT device are shown in Fig. 2.3. The chamber has a rectangular poloidal cross section of 90 cm $\times$ 53.3 cm and it is evacuated by a 500 ℓ/min turbomolecular pump (ULVAC YTP-500SA rev.). The base vacuum pressure measured by an ionization gauge is 4×10^{-7} Torr. Two mechanical rotary pumps are also equipped, one (ANEST

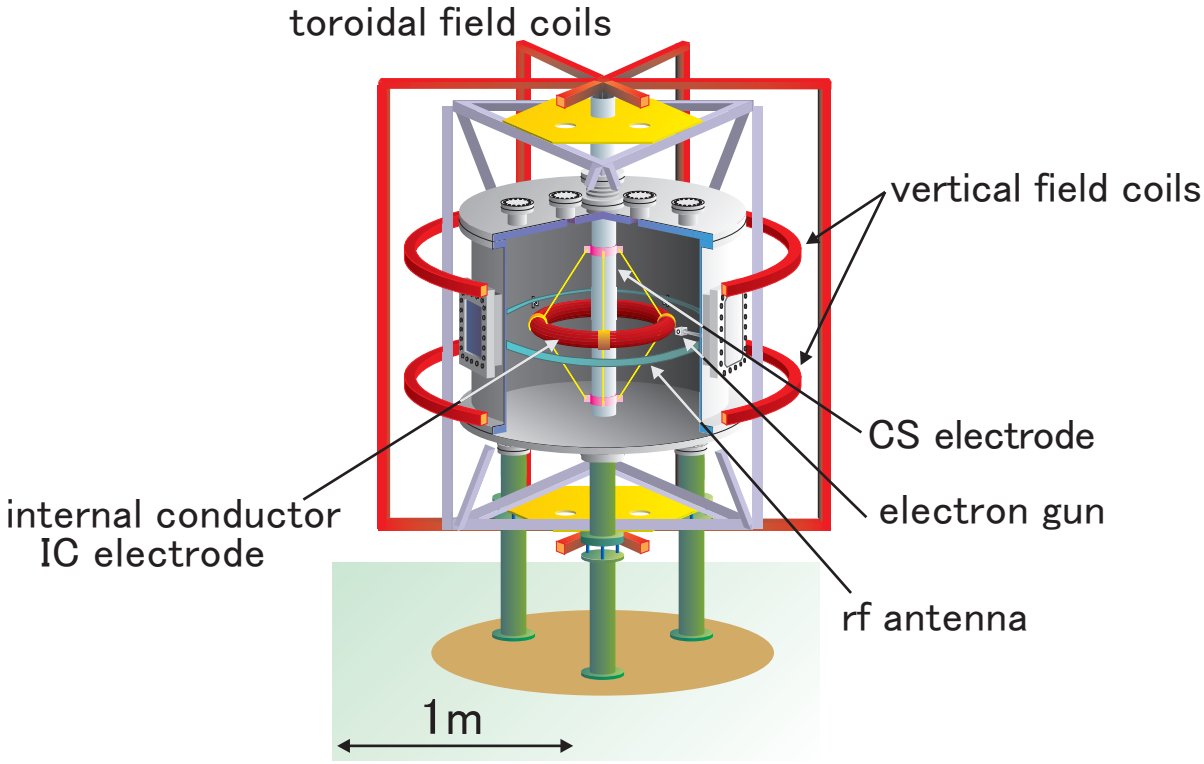

Figure 2.1: Diagram of Proto-RT (Kondoh 1997 [80]).

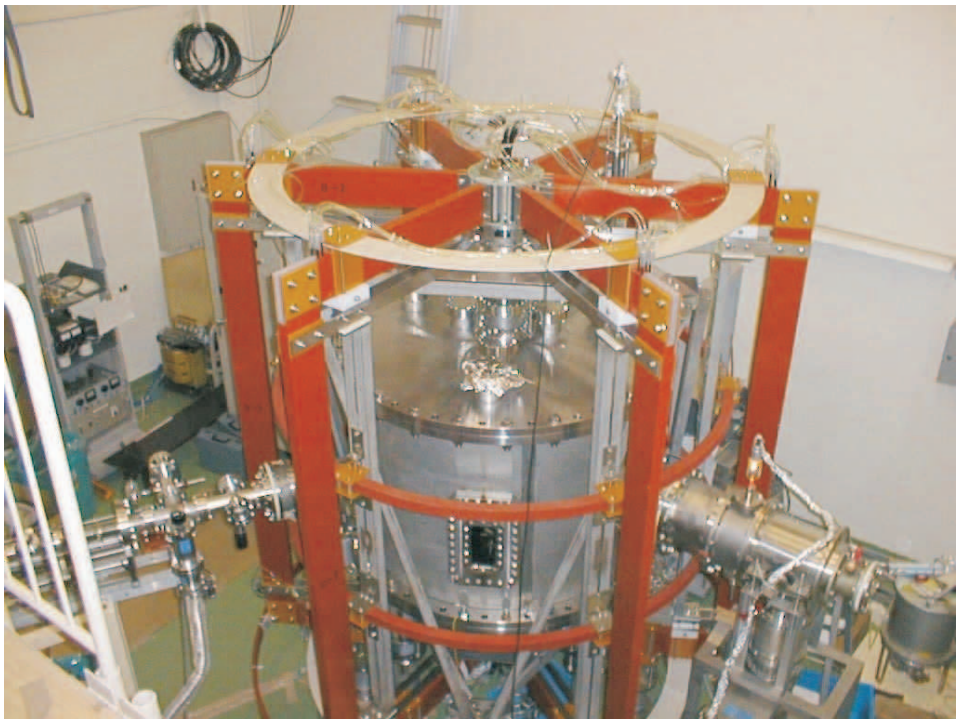

Figure 2.2: Photograph of Proto-RT.

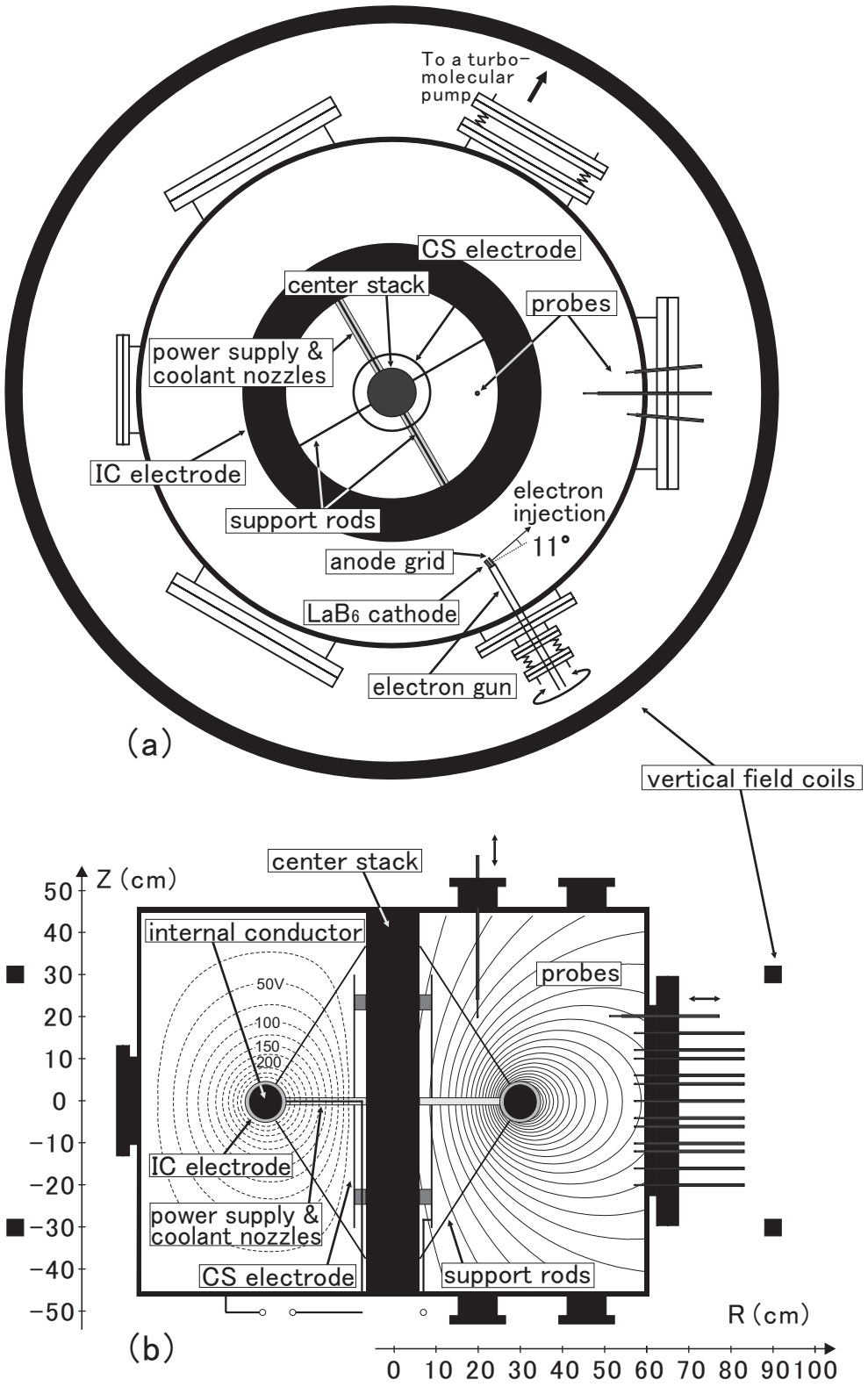

Figure 2.3: (a) Top view and (b) poloidal cross section of the Proto-RT chamber. Magnetic surfaces of dipole field (solid lines) and vacuum electrostatic equi-potential contours when the IC electrode is biased to V_{IC} = +300 V (dotted lines) are also described in (b).

IWATA ISP-500) is for roughing of the chamber from atmospheric pressure, and the other (ULVAC GVD-050A) is for differential evacuation near a rotating flange of the electron gun.

Proto-RT has three rectangular maintenance ports of 41 cm × 26 cm on the side face, and fifteen ICF152 ports on the top, bottom and side faces of the vessel. Among three ICF ports on the side face of the chamber, the north-east port is used for the electron gun and the south port is used for the install of 13.56 MHz RF. A diagnostic flange, attached to the east maintenance port, has twenty-two gauge ports and it is used for the installation of the diagnostic probes. Diameter of the gauge ports is $\phi 7$ mm and it is located between $Z = -20$ cm and 20 cm with a vertical intervals of 2 cm. North-west and east ICF 152 ports at $R = 20$ cm on the top side of the device are also used for the insulation of diagnostic probes. Electric cables for potential control electrodes are arranged through the east ICF 152 port at $R = 46$ cm on the bottom side of the device.

Magnetic field coils

As described in Fig. 2.1, Proto-RT has three kinds of magnetic field coils: internal conductor, vertical field coils, and toroidal field coils, and a variety of field configurations can be produced by the combination of these coils. Inside the chamber, a ring-shaped internal conductor (IC) for the production of dipole magnetic field [77,78] is hung by support rods that are connected to the center stack (CS) of 11.4 cm diameter. The major radius and minor radius of the IC case is 30 cm and 4.3 cm, respectively. Electric current and coolant for the IC are fed through a pair of tube structures via the CS. All these structures, including the support rods and coolant or feeder tubes, are covered by ceramic tubes for the electric insulation from plasmas. Outside the chamber, a pair of vertical field (VF) coils are installed at $R = 90$ cm with an interval of $Z = 60$ cm. It provides almost parallel magnetic field lines inside the chamber, and used for deforming the shape of magnetic surfaces. For the production of magnetic shear, toroidal field (TF) coils are installed in the CS. The IC and the VF coils consist of 175 turns of copper coil as shown in Fig. 2.4 and the TF is assembled from 60 copper coils. The IC coils are installed in a stainless (SUS 304) case. All the coils are power fed by DC power sources and the maximum coil currents are 10.5 kAT (IC), 5.25 kAT (VF), and 30 kAT (TR), respectively. The

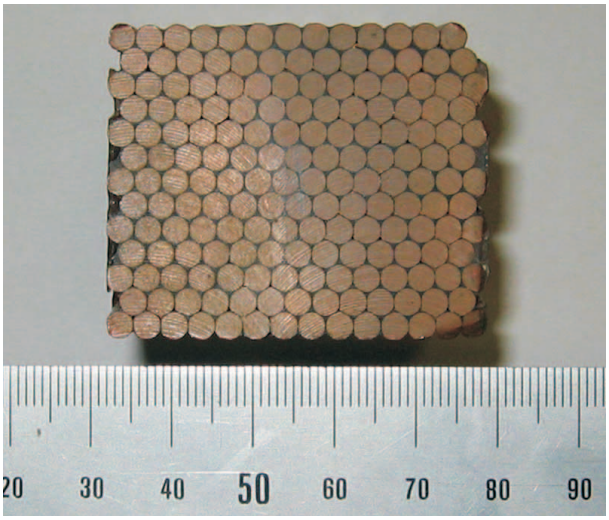

Figure 2.4: Cross section of a coil used for the internal conductor and vertical field coils.

Vacuum vessel	inner radius	59 cm
	center stack diameter	11.4 cm
	height	90 cm
	base pressure	4×10^{-7} Torr
Internal conductor (IC) Coil	major radius	30 cm
175 turns	minor radius	4.3 cm
	coil current	10.5 kAT
	cooling	freon
Vertical field (VF) Coils	major radius	90 cm
175turns	coil current	5.25 kAT $\times$2
	cooling	air
Toroidal field (TR) coils	coil current	30 kAT
60 turns	cooling	water
Electron gun	cathode	LaB_6
	acceleration voltage	up to 2 kV
	emission current (B = 0)	750 mA
RF oscillator	frequency	13.56 MHz
	input power	up to $\sim$ 1 kW

Table 2.1: Machine parameters of Proto-RT

typical strength of the magnetic field in the confinement region of the chamber is of the order of 10^{-2} T. For the cooling of the magnetic field coils, refrigerant fluid (IC) and water (TF) are circulated and air-cooling is used for VF. These device parameters are summarized in table 2.1.

2.1.2 Magnetic surface configuration

As well as the conventional toroidal field coils, Proto-RT has an internal conducting ring and vertical field coils for the production of poloidal magnetic fields. Thus plasmas are trapped on a closed magnetic surface configuration, which had not been used in previous experiments for non-neutral plasmas [52]. Typical magnetic surfaces and magnetic field strength in the poloidal cross section of the Proto-RT chamber are shown in Fig. 2.5. Thick lines show the magnetic surfaces that intersect the vessel wall.

2.1.3 Electrodes for potential control

A toroidal non-neutral plasma relaxes to an equilibrium state by the help of external electric fields from outside of the space charges [40]. As far as an equilibrium is found, this external fields are automatically generated by the induced image charges on the chamber. The equilibrium can

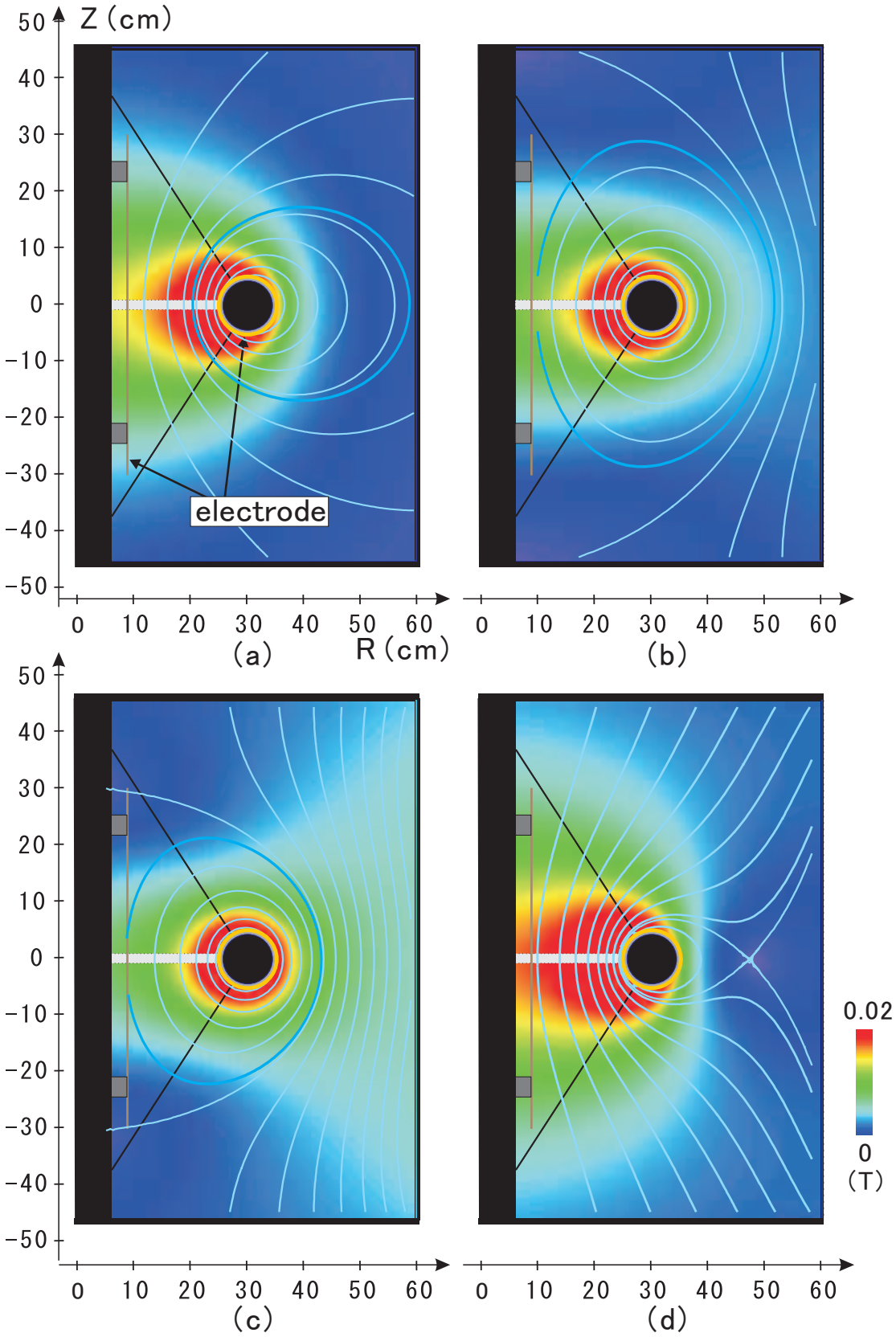

Figure 2.5: Magnetic surfaces and field strength of Proto-RT, generated by the combination of dipole and vertical field coil currents I_{IC} and I_{VF} of (a) 7 kAT and 0 (pure dipole field), (b) 7 kAT and −2.33 kAT (3:-1), (c) 7 kAT and −4.67 kAT (3:-2), and (d) 7 kAT and 2.33 kAT (3:+1).

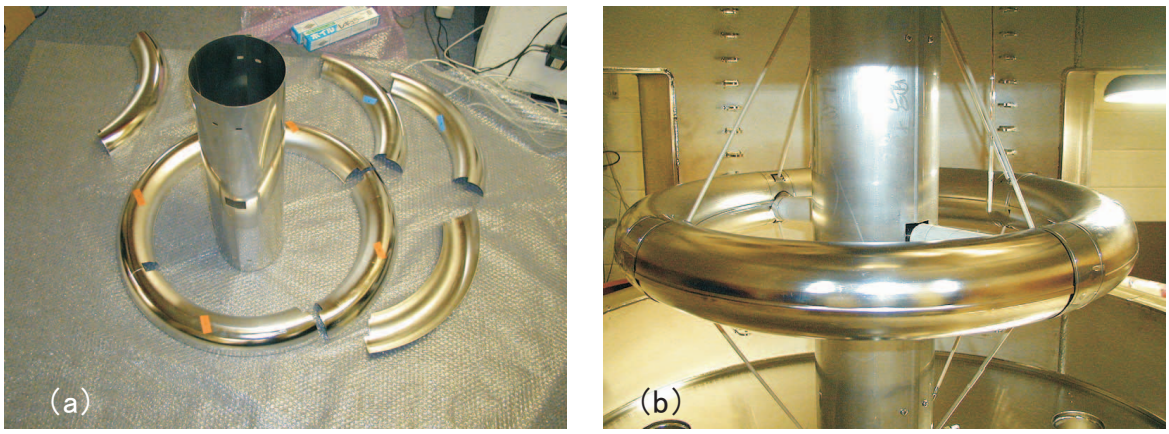

Figure 2.6: Electrodes for potential control (a) before the installation and (b) when installed in Proto-RT.

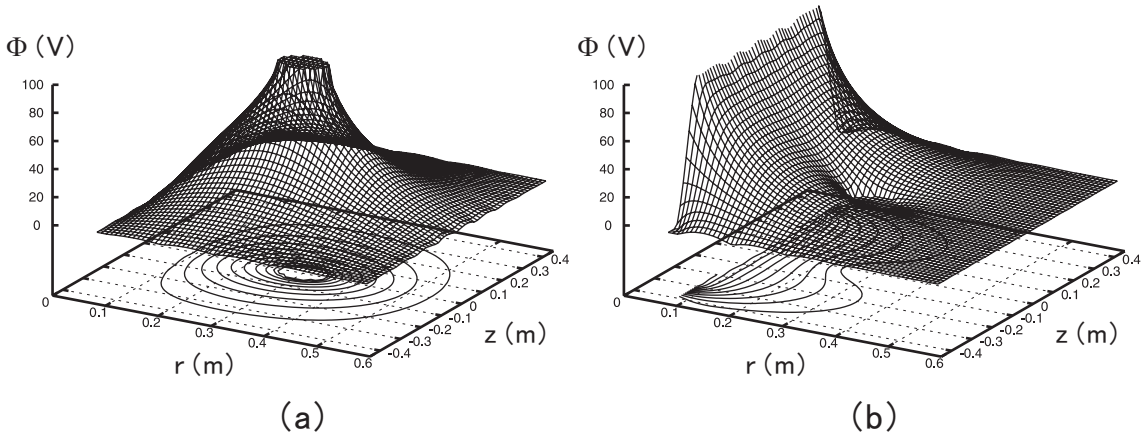

Figure 2.7: Vacuum (no plasma) potential profiles generated by plasma control electrodes on a poloidal cross section (cf. Fig. 2.3 (b)) of Proto-RT. A potential of 100 V is applied to (a) the IC and (b) the CS electrode and another electrode is shorted to the ground. The contours are plotted at intervals of 10 V.

also be externally controlled by applied electric fields generated by the electrodes. The electrodes are also effective for the potential optimization and formation of radial electric field inside neutral plasmas. In this study, the effects of electrode biasing were examined.

For the potential optimization and formation of radial electric field inside the plasma, a pair of electrode are installed in Proto-RT. Because the center stack and stainless cover of the IC are both shorted to the ground (the chamber of Proto-RT), it is difficult to separate them each other electrically. Thus insulating materials are placed on the IC and the CS, and electrodes are installed on the insulations. In order to avoid the sputtering or to minimize the distortion of magnetic fields, the electrodes is made of 1 mm-thick SUS 304 stainless steel. Vacuum equi-potential contours inside the chamber when V_{IC} = +100 V and V_{CS} = +100 V are shown in Fig. 2.7.

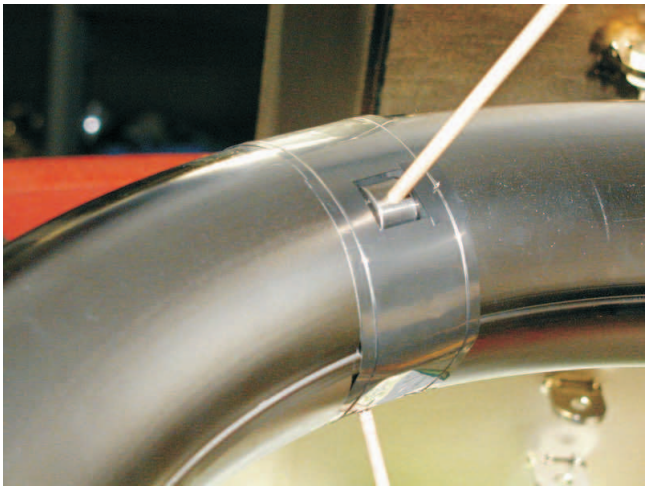

Figure 2.8: Enlarged view of the IC electrode.

The IC electrode was assembled from eight crescentic parts of 90° cut. Minor radius and surface area of the IC electrode are 5 cm (7 mm larger than the IC coil cover) and 0.59 m^2, respectively. The IC electrode is insulated from the IC cover by four pieces of teflon molding and kapton sheets. On these insulating material, the electrode is fixed by ϕ0.2 stainless (SUS316) wire. The gap of each part of the IC electrode is covered with 50 μm thick stainless sheets. This is in order to repress the distortion of electric fields due to the exposure of grounded IC case, and to hide the teflon molding from plasmas. Also electrical connection of each part was done by these stainless sheets. A bias voltage, V_{IC}, of up to ±600 V are applied by a DC power source against the vessel wall for the creation of radial electric field. Potential profiles generated by the electrodes in a vacuum (no plasma) chamber of Proto-RT are described in Fig. 2.7. The electrical insulation of the electrodes was tested by a 1 kV and 2000 MΩ high voltage tester and 2 kV power source for two minutes. The test was done between the chamber and each electrode, and, between each electrode in the atmospheric pressure. Electric cables are connected to the terminals of a ICF152 flange at north-east R = 20 cm port. In order to minimize the distortion of electric fields, the feeder cables are covered by a grounded stainless tubes and located along the CS.

Another electrode is also installed on the CS, and power fed by a DC power source of 350 V. To avoid interference of the CS electrode with the coolant nozzle and feeder cables, there is a space of 3 cm between the electrode and the center stack, as shown in the top view of the device in Fig. 2.3 (a). The electrode is fixed to a pair of photoveel (ceramic) insulator, which is attached to the center

Internal conductor (IC) electrode	major radius	30 cm
	minor radius	5 cm
Center stack (CS) electrode	major radius	9 cm
	height	60 cm
Common properties	material	SUS304
	thickness	1.0 mm
	electrical insulation	$>$ 2 kV (at 1 atm)

Table 2.2: Parameters of potential control electrodes

stack. The diameter of the CS electrode is 18 cm. The longitudinal length of the CS electrode is 60 cm, which is 30 cm shorter than the height of the vessel, and it is limited by interference with the support rods of the IC coil. However, the electric field in the confinement region (around $z = -20 \sim +20$ cm) is almost smooth (Fig. 2.7 (b)) and the effects of the irregular field are supposed to be small.

As electric feeder cables, teflon coated Junfron® wire is spot welded to the electrode near the coolant nozzle, and laid inside the nozzle insulator, then placed along the center stack, inside the CS electrode. The wire is covered by grounded stainless tubes for electric shield, and exposed part of the wire is also covered by an alumina (SSA) insulating tube. The other end of the wire was connected to a power source via a ICF152 flange with electric terminals, at $R = 20$ cm diagnostic ports on the bottom face of Proto-RT.

2.1.4 Electron injection

For the formation of electron plasmas and application of voltage bias to neutral plasmas, an electron gun is installed in Proto-RT [83]. Photographic views of the electron gun are shown in Fig. 2.9. The electron gun is located near $Z = 0$ plane, and it is movable in the radial direction. Injection angle of the gun is also variable using a rotating flange.

Lanthanum hexaboride (LaB_6) sintered compact (DENKA BETA PLUS W2) is employed as a cathode of the electron gun. Among other thermoelectron sources, LaB_6 has a low work function of $\phi_W = 2.6$ eV. Total radiation energy Q emitted from a body with surface area of S and temperature of T is given by

$$Q = \varepsilon_r S \sigma T^4,$$

where $\sigma = 5.67 \times 10^{-8}$ W/m^{2}K^4 is Stefan-Boltzmann constant and ε_r is the radiation ratio [105]. Thus the use of high ϕ_W materials requires much more electric power, which might lead to difficulty in the operation or contamination of the vacuum. When compared with conventional tungsten ($\phi_W = 4.5$ eV) cathodes, LaB_6 can be operated at lower cathode temperatures with higher emitting

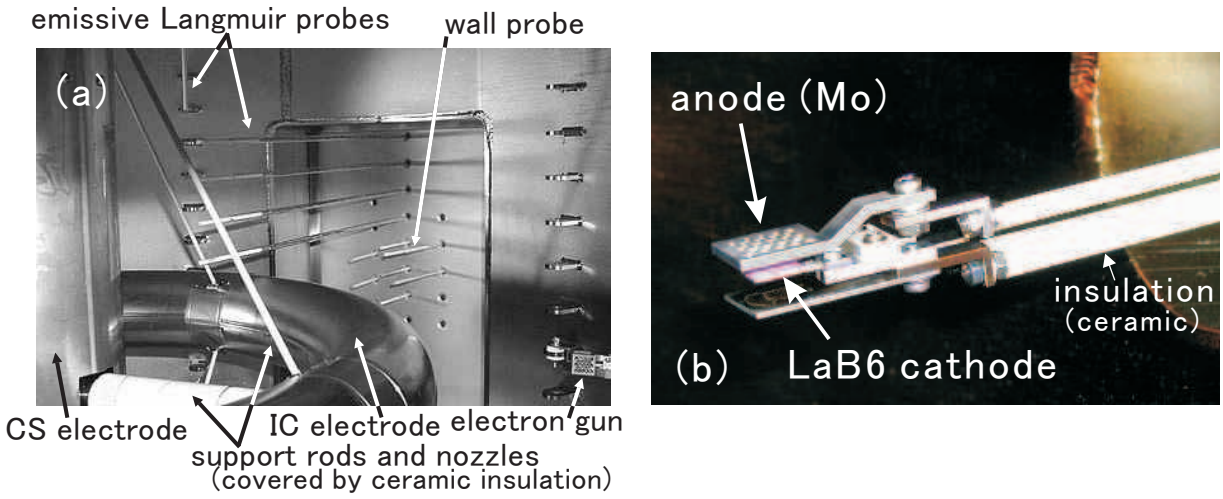

Figure 2.9: (a) Photographic view inside the Proto-RT chamber including the probe and electrodes configuration, and (b) the structure of electron gun.

currents [105]. Most boride materials, including LaB_6, has negative TCR (temperature coefficient of resistance) and heating current from a power source is usually fed by constant current mode, in order to avoid the thermorunaway.

Figure 2.10 shows the construction of the electron gun. Acceleration voltage of up to $V_{\rm acc}$ = 1.3 kV is applied between the LaB_6 cathode and a molybdenum anode grid of 65 % transparency, located 2 mm in front of the cathode. The cathode is heated with a current of up to 28 A by a regulated DC power source (TAKASAGO NL035-30) and operated at temperature of $\sim$ 1800 K. Acceleration voltage $V_{\rm acc}$ is controlled by a MOS-FET open-drain semiconductor switch as described in an electric circuit for the control of the electron gun in Fig. 2.11. Acceleration duration signal is generated by a timer circuit and the signal is transmitted to the control circuit via a optical coupler, because the cathode is electrically floating with high voltage. Acceleration voltage is supplied by a DC power source (NISTAC PS2000-1) and switched by a MOS-FET (HITACHI 2SK2393). Drain current from the cathode ($I_{\rm drain}$), return current to the anode ($I_{\rm anode}$), and net beam current that emitted from the gun and returns to the chamber wall ($I_{\rm chamber}$) are measured by 1 Ω shunt resistances as shown in the diagram. An example of the drain current from the cathode in pure-electron-plasma experiment is shown in Fig. 2.12. The obtained drain current is $I_{\rm drain} \sim 0.8$ A when $V_{\rm acc}$ = 1.2 kV and no magnetic field. With $V_{\rm acc}$ = 300 V, the electron injection beam current $I_{\rm beam}$ is 26 mA when V_{IC} (IC electrode bias voltage) is 0, and 5.9 mA when $V_{IC} = -300$ V. The gun is usually operated at a base pressure of below 1×10^{-5} Torr, in order to avoid rapid evaporation and evaporation coating due to the oxidation of the cathode.

The injection angle of the electron gun is decided according to a numerical calculation [81] so that the electrons take sufficiently long orbit lengths. Because of the large gyration radius, electrons

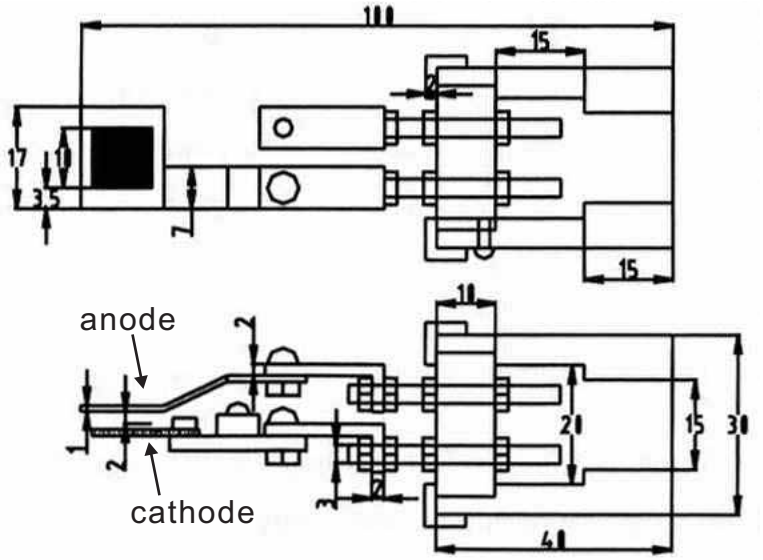

Figure 2.10: Schematics of an electron gun (Nakashima 2002 [83]).

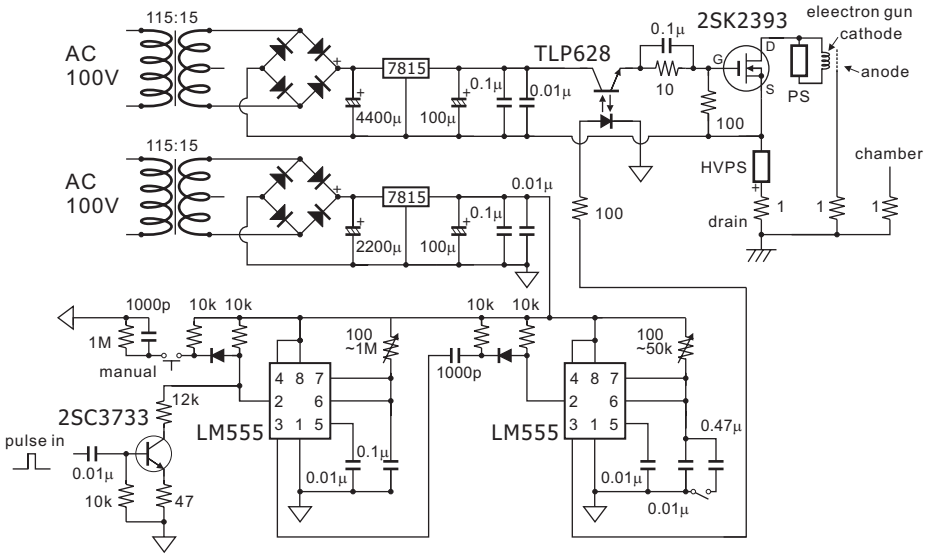

Figure 2.11: Electric circuit for the electron gun operation, including a MOS-FET semiconductor switch, pulse control, power sources, opt-insulation, and shunt resistances for electron currents.

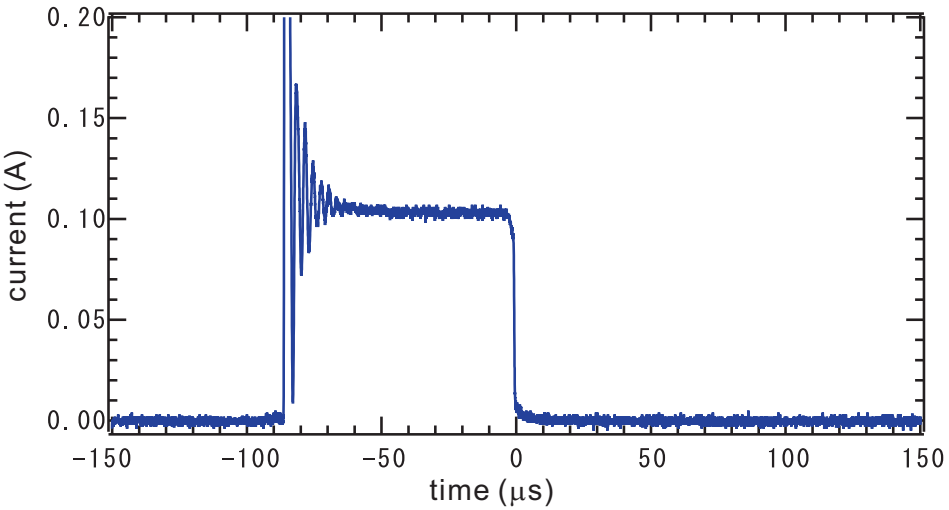

Figure 2.12: Temporal evolution of drain current from the electron gun.

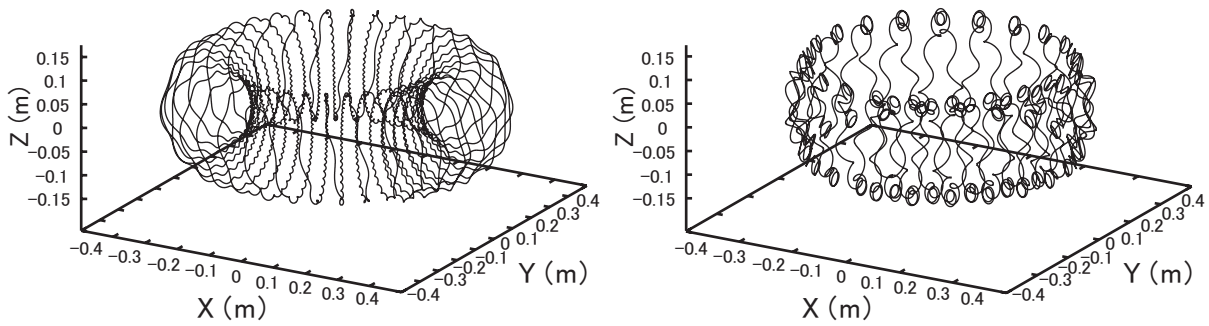

Figure 2.13: The typical orbits of an electron in a dipole magnetic field of I_{IC} = 5.25 kAT. Electrons are injected from R = 46 cm and Z = 0 cm with an acceleration voltage of 300 V, (a) in the parallel direction (pitch angle $\theta_p = 0°$) and the electron takes transit orbit, and (b) when $\theta_p = 45°$ and the electron is mirror trapped. The center axis of the device is located as X=Y=0.

obey a strongly nonlinear equation of motion in the inhomogeneous magnetic field, resulting in chaotic (non-periodic) motion with long orbit lengths [79]. A numerical calculation shows that electrons are effectively injected from the edge of the confinement region [82]. The typical orbit of a single electron injected into a dipole magnetic field is shown in Fig. 2.13 (bird-eye view where $X = Y = 0$ is the center axis of the device). When the pitch angle between the dipole magnetic field lines and initial injection velocity is large, electrons take transit orbit around the IC as shown in Fig. 2.13 (a). Electrons with small parallel velocities are mirror trapped in the bad curvature region (Fig. 2.13 (b)). Electrons also undergo the Larmor rotation around the magnetic field lines and drift motion in the toroidal direction due to the $\mathbf{E}\times\mathbf{B}$ and ∇B/curvature drifts. As shown in Fig. 2.14, part of the injected electrons hit the electrodes and observed as electrode currents.

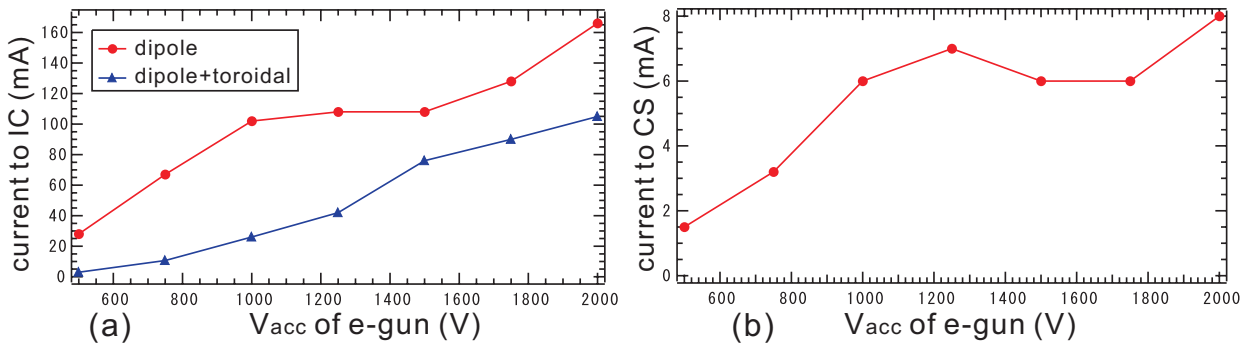

Figure 2.14: Current of electron plasma flowing to (a) IC and (b) CS electrodes. Potentials of the electrode $V_{IC} = V_{IC} = 0$ (terminated by 1 Ω resistors),

2.1.5 13.56 MHz RF

For the production of neutral plasmas, 13.56 MHz radio frequency (RF) oscillator is installed in Proto-RT. The RF power is transmitted to plasmas using capacitively (C-type) and inductively (L-type) coupled antenna via a LC matching circuit. RF terminals are connected to a 13.56 MHz power source via DC cut capacitors.

2.2 Diagnostics

2.2.1 Emissive Langmuir probes

Electrostatic probes, or Langmuir probes [96–98] are one of the most fundamental and first developed diagnostics for plasmas. Basically, the probe is a simple metallic tip inserted into a plasma, and biased to some potential. Analysis of the relation between the bias voltage and the obtained current provides the information of electron number density n_e, electron temperature T_e, space potential ϕ_s, and distribution function f_i of charged particles. Although Langmuir probes might perturb the surrounding plasmas, and also measurable parameter region is rather limited, it can provide the quantities of laboratory or natural plasmas with fine spatial resolution.

In this study, among other parameters, space potential ϕ_s is one of the essential parameters for the measurements of both structures of pure electron plasma and radial electric fields in neutral plasma. As described in the following, when plasma has radial electric field, the resultant fast flow might cause the error of the measurements of ϕ_s. In this study, emissive probes [99–102, 104] are employed for the precise measurements of space potentials. The characteristics of emissive probes, its construction, and the usage for the measurements of potential structures are explained in this section.

Probe theory

When a plasma has only single species of particles (say, electrons), the current density j flows into the probe is

$$j = e\int_0^\infty f(\mathbf{v})\mathbf{v}\cdot\mathbf{n}d^3v, \tag{2.1}$$

where $f(\mathbf{v})$ is electron distribution function, $\mathbf{n}$ is the normal to the probe surface. For simplicity, we assume planar probe surface in Cartesian coordinate,

$$j = e\int_{v_{\rm min}}^\infty f(v_{\rm x}, v_{\rm y}, v_{\rm z})v_{\rm z}dv_{\rm z}. \tag{2.2}$$

Here $v_{min} \equiv [2e(\phi_{\rm s}-\phi_{\rm b})/m_{\rm e}]^{1/2}$, $\phi_{\rm b}$ is the probe bias voltage, $\phi_{\rm s}$ is the plasma space potential, and $m_{\rm e}$ is the electron mass. When the electron distribution is given by a drifting Maxwellian with temperature $T_{\rm e}$ and drift velocity $v_{\rm d}$ (in z direction, perpendicular to the probe surface):

$$f(\mathbf{r},\mathbf{v}) = n_e\left(\frac{m_{\rm e}}{2\pi k_{\rm B}T_{\rm e}}\right)^{3/2}\exp\left(-\frac{m_{\rm e}(v_{\rm z}-v_{\rm d})^2}{2k_{\rm B}T_{\parallel}}\right)\exp\left(-\frac{m_{\rm e}({v_{\rm x}}^2+{v_{\rm y}}^2)}{2k_{\rm B}T_{\perp}}\right), \tag{2.3}$$

then the electron current collected by a planar probe is

$$I = eSn_{\rm e}\left(\frac{k_{\rm B}m_{\rm e}}{2\pi T_{\parallel}}\right)^{1/2}\int_{v_{\rm min}}^\infty \exp\left(-\frac{m_{\rm e}(v_{\rm z}-v_{\rm d})^2}{2k_{\rm B}T_{\parallel}}\right)v_{\rm z}dv_{\rm z}, \tag{2.4}$$

where S is the surface area of the probe. The current-voltage (I-V) curve given by (2.4) has a slope around $V = V_s - E_d/e$ ($E_d \equiv m_e{v_d}^2/2e$ is the energy of flow) with a temperature width of T_e, and takes constant values

$$I = \begin{cases} 0 & V \ll \psi_{\rm s} - E_{\rm d}/e \\ eSn_{\rm e}\sqrt{k_{\rm B}T/2\pi m_{\rm e}} & \psi_{\rm s} - E_{\rm d}/e \ll V. \end{cases}$$

Here $I_{\rm s} = eSn_{\rm e}\sqrt{k_{\rm B}T/2\pi m_{\rm e}}$ is called the electron saturation current.

When the Debye length is greater than probe scale size, simplified sheath approximation does not work due to the orbital motion of the charged particles. In the above derivation, the assumption that the motion of electrons is single dimensional is used, and all particles of higher velocity than $v_{\rm min}$ are certainly absorbed by the probe. In real plasmas, when the sheath is thick compared to the size of probes, the orbital motion of the charged particles must be taken into the consideration. According to the orbital theory [96], the saturation current is an increasing function of V, in response to the probe shapes, and the I-V curve is an increasing function even when $\phi_{\rm s} - E_{\rm d}/e \ll V$. The typical characteristics of cold probe is shown in Fig. 2.15.

When the probe tip is biased more negative than the local plasma space potential $\phi_{\rm s}$, the emitted electrons can escape from the probe tip. In the probe characteristics, this electron flow contributes as an effective ion current. When the probe tip is biased positive with respect to $\phi_{\rm s}$, however, the emitted electrons are repelled by the plasma and return to the probe. This behavior of electrons is

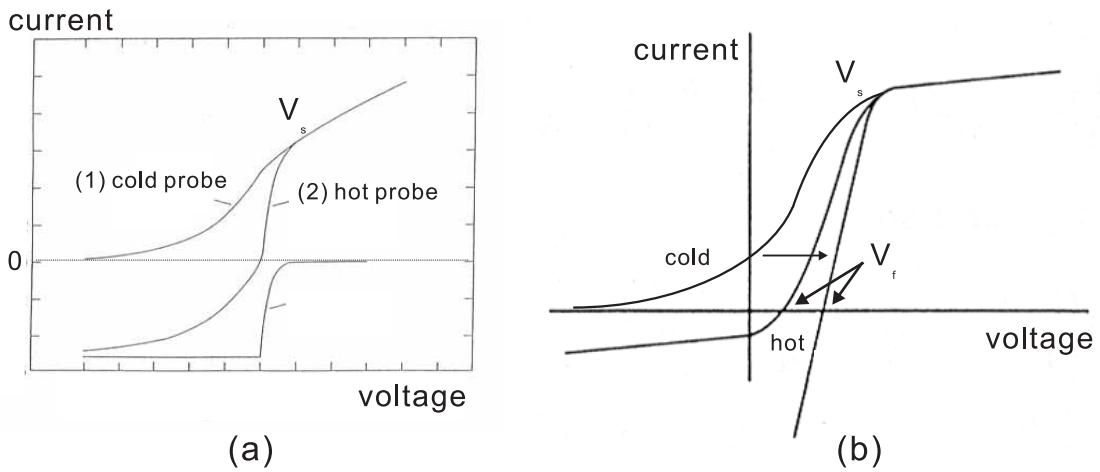

Figure 2.15: Schematic view of the characteristics of hot and cold probes. (a) The emission begins at the space potential of the plasma, but does not increase in an instant, because of the space charge limit. The horizontal part at $\phi < \phi_s$ is due to the limit of the filament current. (b) The relation between the space potential ϕ_s and the floating potential ϕ_f. As the emission current is increased, V_f approaches to ϕ_s, but they do not agree due to the space charge limit.

not affected by the plasma flow (kinetic energy of particles), because it is decided solely by plasma potential. The typical characteristics of cold (non emissive) and hot (emissive) probes are shown in Fig. 2.15. The two characteristics separate from each other near the plasma potential ϕ_s, and one can take it as an indication of the plasma potential. This is quite advantageous to the measurement of space potential compared to the cases of cold probes, where the knee of I-V curve corresponds to the sum of the space potential and the flow energy.

When the probe filament is heated enough, the emission current is space charge limited, and its value is decided by the Child-Lngmuir low. In Fig. (2.16), we assume that electrons are emitted at plane A with an initial (at $x = 0$) velocity of zero toward the plane B: the particle velocity is $v(x) = \sqrt{2ev/m_e}$. Because the current density j is constant in this geometry, the number density $n(x)$ of electrons between two planes is

$$n(x) = -je^{-1}(2ev/m_e)^{-1/2}, \tag{2.5}$$

and Poisson's equation becomes

$$\frac{d^2V}{dx^2} = \frac{j(2eV/m_e)^{-1/2}}{\varepsilon_0} \tag{2.6}$$

Multiplying by dV/dx and integrating from $x = 0$, we have

$$\frac{1}{2}\frac{dV^2}{dx} = \frac{j(2eV/m_e)^{-1/2}}{\varepsilon_0} + \frac{1}{2}\left(\frac{dV}{dx}\right)^2\Big|_{x=0} \tag{2.7}$$

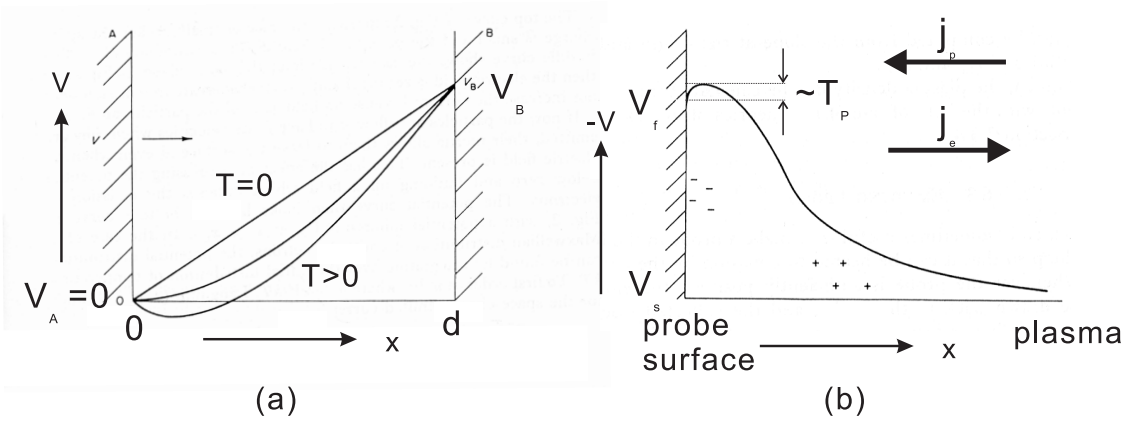

Figure 2.16: (a) Schematic graph of the Child-Langmuir's low. Electrons are emitted from the plane A (left) and escape to the plane B. Three curves are the potential profiles between two planes, according to the electron temperature T. (b) Double sheath formation between the emissive probe and the plasma. Because the emitted electron is space charge limited, there is a potential dip near the probe surface.

Because the charged particles' flow is space charge limited at the filament, at $x = 0$, the gradient of the potential vanishes: $dV/dx|_{x=0} = 0$, and (2.7) becomes

$$V^{-1/4}dV = \left(\frac{2j}{\varepsilon_0}\right)^{1/2}\left(\frac{m_\mathrm{e}}{2e}\right)^{1/4}dx \tag{2.8}$$

Integrating from $x = 0$ to d, the current density is given by

$$j = \left(\frac{2e}{m_\mathrm{e}}\right)^{1/2}\frac{8}{9d^2}\varepsilon_0 {V_\mathrm{B}}^{3/2}. \tag{2.9}$$

This is valid for the "cold" emitted particles (the $T = 0$ curve in Fig. 2.16 (a)). The derivation when the temperature T of the plate A is not negligible compared to the plasma, and the emitted particles have finite speeds at $x = 0$, was done by Langmuir [98]:

$$j = \left(\frac{2e}{m_\mathrm{e}}\right)^{1/2}\frac{8}{9(d-x_\mathrm{m})^2}\varepsilon_0(V_\mathrm{B}-V_\mathrm{m})^{3/2}(1+\alpha), \tag{2.10}$$

where $x_\mathrm{m}, V_\mathrm{m}$, and α are the correction terms.

The floating potential phi_f of the emissive probe is decided by the balance between the collected current from plasma (j_p in Fig. 2.16 (b)) and emission current (j_e). Here j_p is decided by (2.4) and j_e by (2.10). From (2.10), the current emitted from the hot probe is

$$j = \left(\frac{2e}{m_\mathrm{e}}\right)^{1/2}\frac{8}{9d^2}\varepsilon_0(\phi_\mathrm{f}-\phi_\mathrm{s})^{3/2}, \tag{2.11}$$

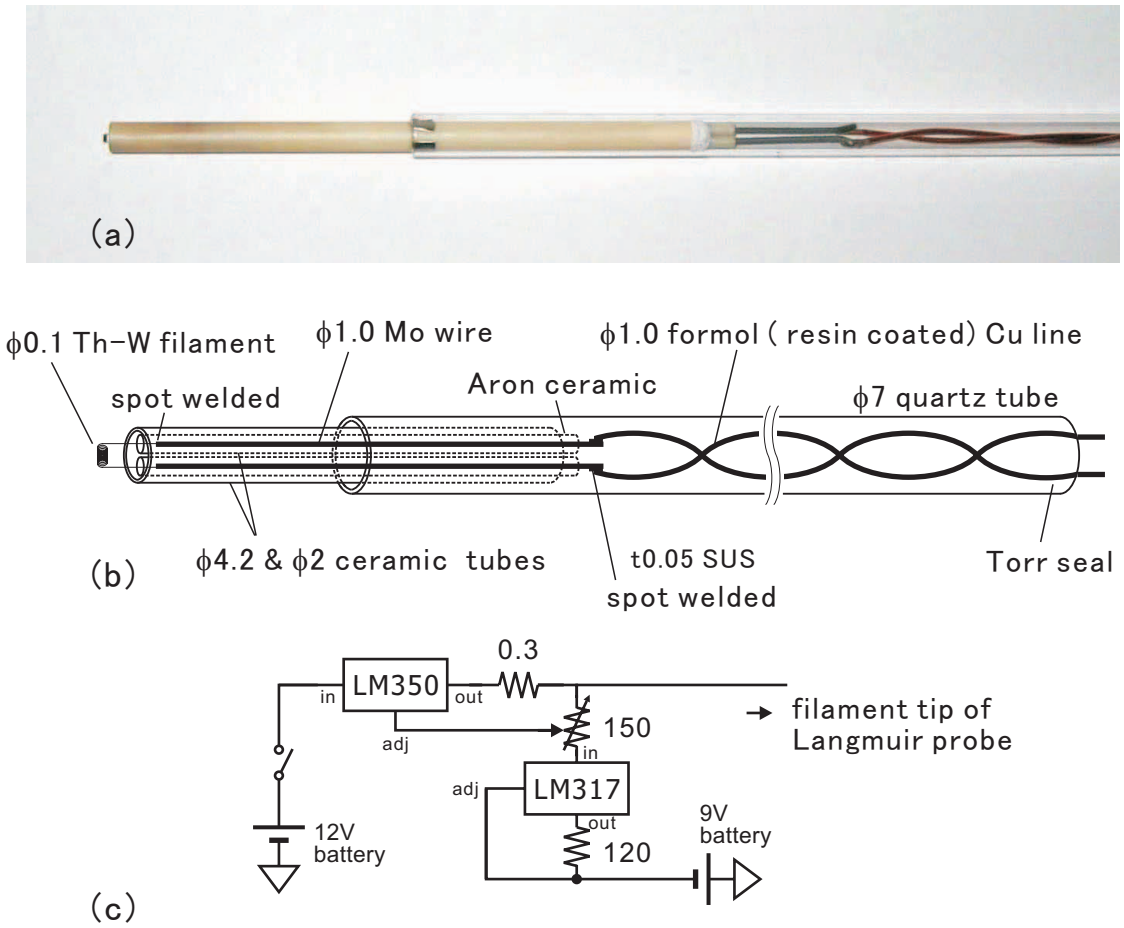

Figure 2.17: (a) Photographic view, (b) construction, and (c) constant current heating circuit of an emissive Langmuir probe.

and we see the current is not canceled when $\phi_f = \phi_s$. This fact must be taken attention when high impedance potential probes are used for the potential measurements: due to the space charge limit, the measured potentials do not agree with the space potential even when the probe filament is sufficiently heated. The validity of the measurements by high impedance potential probes was experimentally tested and will be discussed in the following.

Probe construction and usage

The electrostatic potential of the plasma (both pure electron plasma and neutral plasma in a bias experiment) is measured by emissive Lagnmuir probes and it provides the information of potential profiles with fine spatial resolution. As a tip of an emissive probe, a hot filament (heated by a passage of current) is employed instead of an usual cold metal piece. The principle of emissive probes is, that emitted electrons will escape from the probe only when the tip is more negative than $\sim \phi_s$. For pure electron plasmas, structures like Langmuir probes inside the plasma are serious

obstacles for the realization of stable confinement, but it can be used for the measurements of space potential during the electron injection phase.

The probe tip is a thoria-tungsten spiral filament of 0.1 mm diameter and heated by a DC current of ~ 1.5 A. To increase the surface area and gain more emission current, spiral filaments were employed. The surface of the exposure of the filament is $S \simeq 3\times10^{-6}$ m^2 and it is spot welded to molybdenum support wires. Heating current was fed through copper wires, which were spot welded to molybdenum support wires. The structure of the emissive Langmuir probe is shown in Fig. 2.17. The tip filament is spot-welded to a molybdenum rod of 1 mm diameter, and the molybdenum rod is connected to a copper power line located in a quartz tube. The molybdenum rod is covered by ceramic (SSA-S) tubes, and top 5 mm of the filament tip is exposed to the plasma. In order to avoid electric contact with plasmas, which is caused by the formation of conductive coating on the surface of insulator, or collision of high energy electron beam to the insulator, and cause the breakdown of electric isolation, the support wires are covered with double ceramic tubes and loosely fitted in the inner tubes, The tip is terminated to the chamber across a 100 MΩ high impedance voltage probe (TEKTRONIX P6015A) and used as "floating" probes. Required heating current for the operation in space charge limited region is checked for each Langmuir probe.

The density of the emission current J of heat electrons from materials are given by Richardson-Dushmann's equation; [105]

$$J = \eta A_R T^2 \exp\left(-\frac{\phi_{\rm w}}{k_{\rm B}T}\right), \tag{2.12}$$

where $k_{\rm B}$ is Boltzmann's constant, $A_{\rm R} \sim 120$ Acm^{-2}K^{-2} is Richardman's constant, T is temperature, $\phi_{\rm w}$ is a work function of the material, and $\eta = 0 \sim 1$ is decided by the surface state of the material. The required current for the heating of the filament was about 2 A. When this current is passed in an infinitely long Th-W filament, its temperature is 2800 K. The burn off temperature of a tungsten filament of 0.1 mm diameter is about 3200 K, and enough emission current was obtained before this limit.

High impedance measurements

For the interpretation of emissive Langmuir probes, several techniques are used for the measurements of space potentials $\phi_{\rm s}$. Most simply, when the probe characteristics (current-voltage curves) are obtained, the branching point of the cold (non-emitting) probe and emissive probe curve indicates $\phi_{\rm s}$, provided that the thermal energy of the emitted electrons is neglected. In "floating" potential method [101], the probe tip filament is terminated across a high impedance resistance and "floating" potential is measured. Although the effects of finite filament temperature and space charge effects must be considered [104], it provides a good approximation of the space potential when sufficient emission current is obtained. Inflection-point method [102] is also used for the space potential measurements. In this method, the characteristics of $I_{\rm em}$ (emission current)-

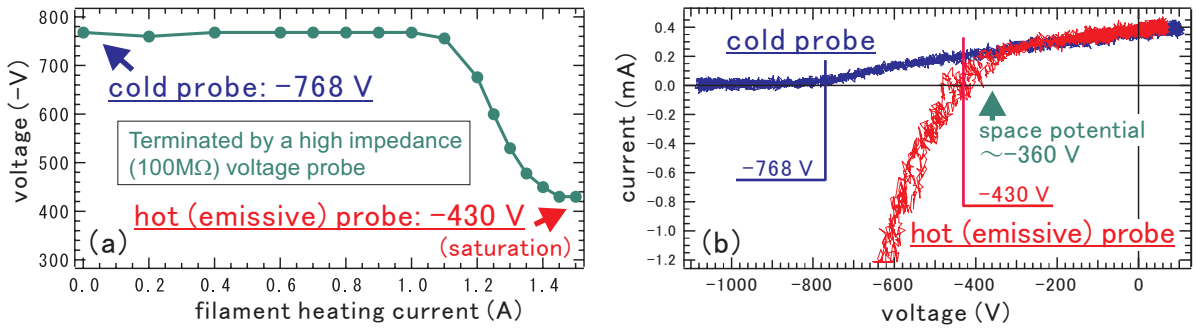

Figure 2.18: (a) Floating potentials measured by an emissive Langmuir probe in the variation of filament heating current I_f. (b) $I - V$ characteristics of hot (emissive I_f = 1.5 A) and cold (non-emitting, I_f = 0 A) probes.

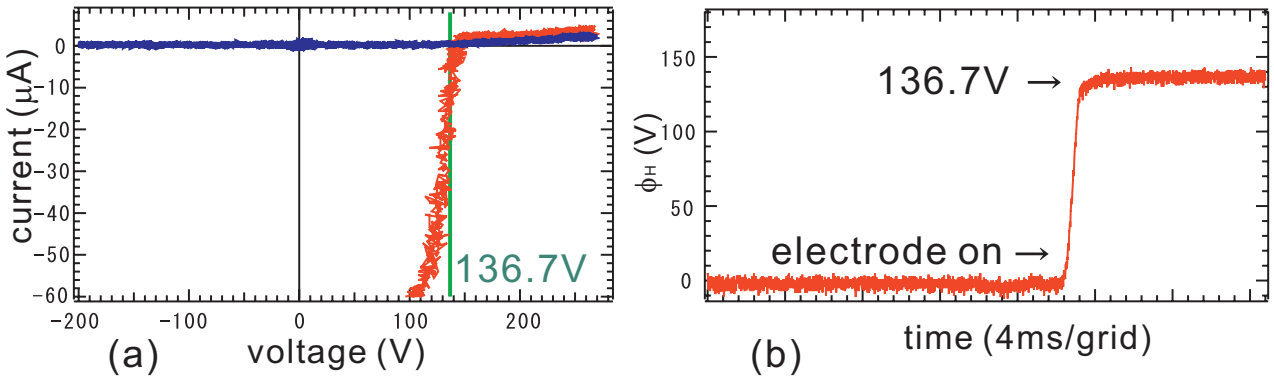

Figure 2.19: (a) Current-voltage characteristics of an emissive Langmuir probe in neutral (hydrogen) plasma, where the branch point of the tow curves is 143.5 V. (b) High impedance potential measurement.

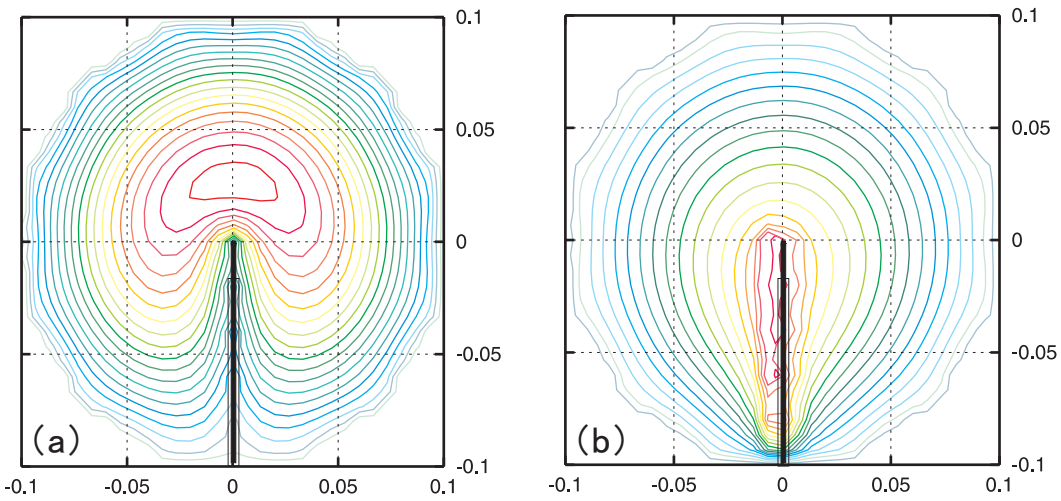

Figure 2.20: Potential profiles of electron plasma with grounded and floating Langmuir probes.

V (bias voltage to the probe tip) is measured and ϕ_s is decided by using its differentiated trace dI_{em}/dV. Without using the collecting current, ϕ_s is identified as where $dI_{em}/dV = 0$.

Among these methods, high impedance ("floating") method was used in this study. In the present experiments, space potential of the plasma is generated by the large negative space charges or electrode biasing up to some 100 V, and typical measured potential is quite large. When sufficient emission current is obtained, error of the high impedance method is in the order of the temperature of the filament ($\sim$ 0.2 eV), and it is often negligibly smaller than ϕ_s. High impedance method also has an advantage in disturbance to the plasma. Figure 2.20 shows the example of calculated potential profiles of cylindrical charged cloud with inserted insulated conductor. When the conductor rod is grounded in Fig. 2.20 (a) the electrostatic potential contours are strongly distorted, but these effects are relatively reduced when the conductor is in the floating potential (Fig. 2.20 (b)).

In the following, we designate the potential measured by the high impedance probe as Φ_H. Assuming a Maxwellian electron plasma, the floating potential Φ_F of the emissive Langmuir probe is given by

$$\Phi_F = \Phi_S - (k_B T_e/e)\ln(I_{es}/I_{em}),$$

suggesting that Φ_F gives a good approximation of Φ_S when a sufficient emission current is obtained ($I_{em} >> I_{es}$). Here Φ_S is space potential, T_e is electron temperature, I_{es} is electron saturation current, and I_{em} is electron emission current from the filament. The emission current from the probe filament is decided according to the magnetic field strength, space charge effect and device geometry, and surface of the filament, and thus it is not straightforward to decide the exact emission current. *I-V* (current-voltage) characteristics of the Langmuir probes.

Figures 2.18 and 2.19 shows the typical *I-V* characteristics and Φ_H of cold (non-emitting)

and emissive probes in both pure electron plasma and neutral (hydrogen) plasma. Although the "floating" potential of a cold Langmuir probe is not defined in pure electron plasmas, Φ_H gives a certain value according to the *I-V* curve and the probe high impedance. Especially due to the fast flow of electron plasma caused by the self electric field of non-neutral plasma, the *I-V* curve of cold probe has a long "tail" below Φ_S [99]. Here Φ_S is indicated as the branching point of two *I-V* curves provided that filament temperature (~ 0.3 eV) is neglected. Thus the measured Φ_H of cold probe, -768 V, gives much smaller value than the space potential of $\Phi_S = -360$ V. On the other hand, Φ_H of the emissive probe is approximately equal to $\Phi_F = -430$ V and it is rather close to Φ_S. Because the emission current is limited due to the space charge effect and magnetic field strength, further increase of filament heating current does not contribute to approach of Φ_H to Φ_S. We have checked the *I-V* curves at several points and found that Φ_H of emissive probe gives a good approximation of the space potential within an error of ~ 20 % in electron plasmas. For neutral plasmas, Φ_H of emissive probe gives typically underestimate of some volts compared with space potential.

Although emission currents from each Langmuir probe come to space charge limited region around $I_{fil} = 1.5$ A (as indicated in saturation in Fig. 2.21), required heating current shows some dispersion due to the small structure difference. Figure 2.21 shows the potentials measured by high-impedance emissive Langmuir probes in the variation of filament heating current. When used as floating (high impedance) probes, required currents are checked beforehand in the actual experimental condition, and used in the saturated region. Figure 2.22 shows the example of measured potential (radial profiles in different magnetic field strength) by high-impedance cold and hot Langmuir probes. Passage of filament current is effective for the removal of surface contamination of probe tips as shown in Fig. 2.23.

Probe configuration

The probes are arranged as an array located between $Z = -20$ cm and $+20$ cm (the configuration of the probes is shown in Fig. 2.3) and two dimensional potential structures are measured in the confinement region. Schematic and photographic views of emissive Langmuir probe configuration are shown in Figs. 2.17. The probes were inserted from gauge ports (*r-probes*) on the diagnostic flange and one gauge port (*z-probe*) on a diagnostic port. The probes are manually movable along **r** (*r-probe*) or **z** (*z-probe*) direction, and we can obtain two-dimensional potential profiles. Measuring points and reconstructed 2-d profiles are shown in Fig. 2.24.

After the stop of the electron supply, Langmuir probes placed inside the confinement region are serious obstacles for the realization of stable equilibrium. For the measurement of electrostatic fluctuations and determination of the confinement time of the plasma without such perturbations, 5×15 mm and 5×250 mm copper foils are covered by insulating quartz tubes and installed in

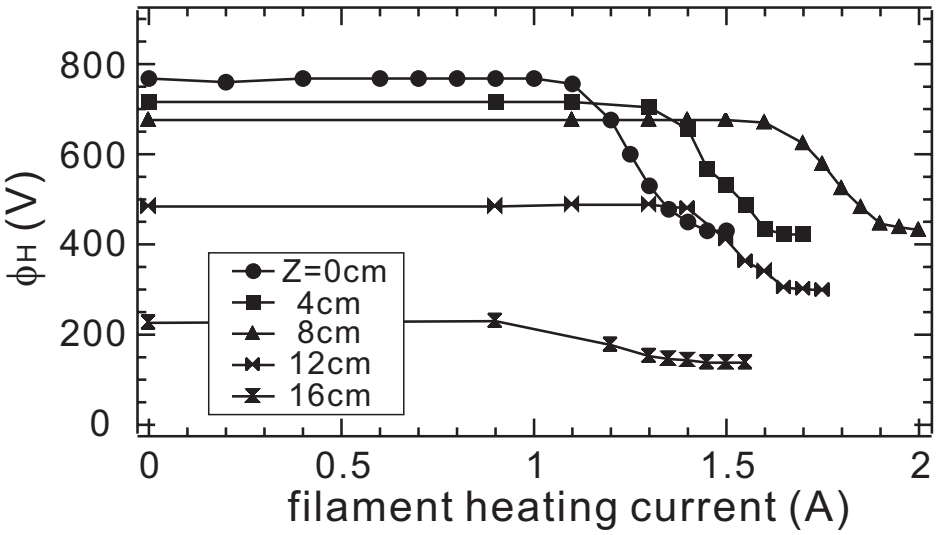

Figure 2.21: High-impedance potentials measured by emissive Langmuir probes at Z = 0 - 16 cm.

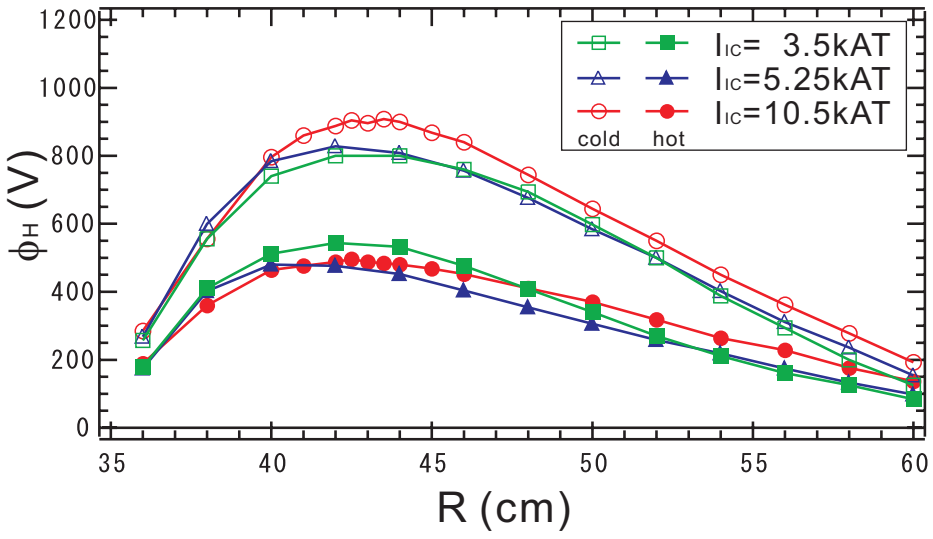

Figure 2.22: Radial high-impedance potential profiles measured by hot and cold Langmuir probes in dipole field configurations.

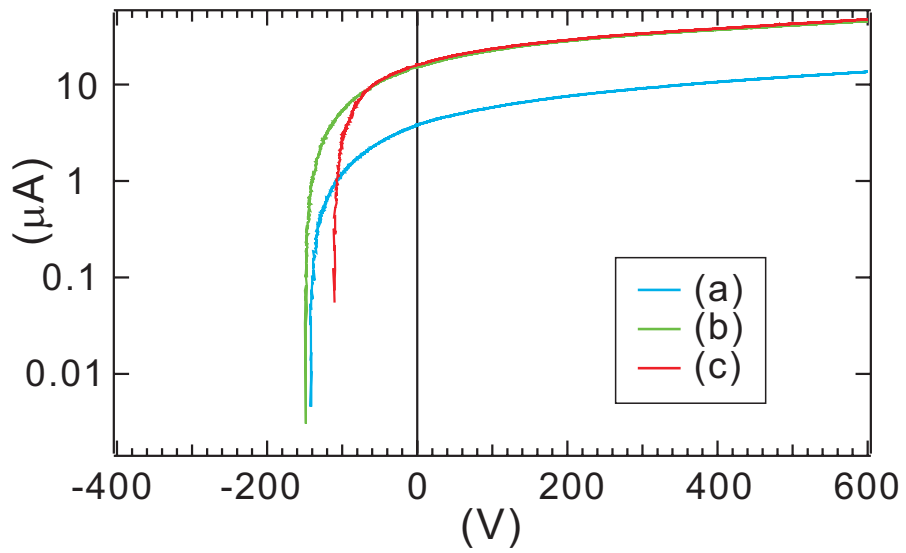

Figure 2.23: Current-voltage characteristics of an emissive Langmuir probe in the variation of filament heating current $I_{\rm fil}$, (a) $I_{\rm fil} = 0$, (b) $I_{\rm fil} = 2.0$ A, and (c) $I_{\rm fil} = 2.7$ A.

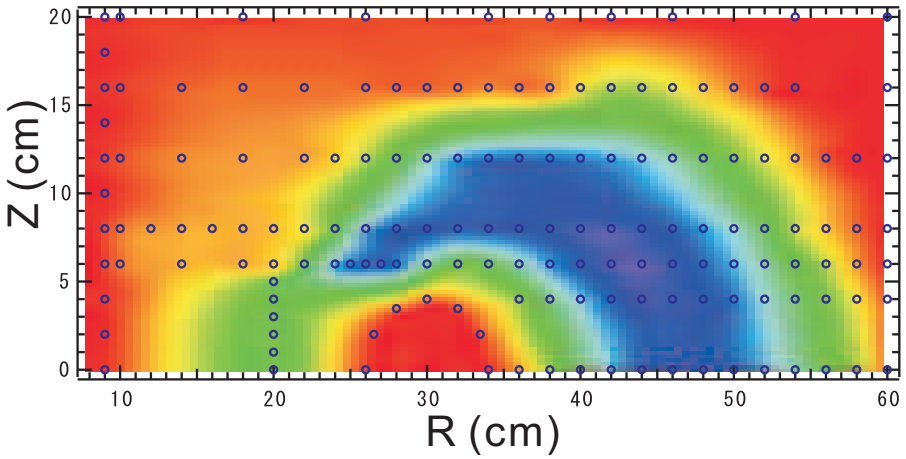

Figure 2.24: Measuring points (circles) and reconstructed 2-d profiles of space potential in the $R-Z$ plane ($Z > 0$).

the chamber, and used as wall probes [35, 93, 94]. The sensor foil is connected to the vessel wall through a current amplifier for the observation of image current, which indicates the motion of the plasma. The longer wall is placed over the entire confinement region and used for the estimation of the remaining charge of the plasma by integrating the passing image current.

2.2.2 Wall probes

Electrostatic fluctuations of the plasmas are measured by wall probes. During the electron injection, a current collected by the high-impedance emissive Lagmuir probe is less than 10 μA. It is much smaller than the injected beam current of the electron gun of $2 \sim 30$ mA, and the resultant disturbance is supposed to be small. In fact, additional insertion of another Langmuir probe does not significantly change the measured Φ_{H}, and we therefore conclude that during the electron injection, the Langmuir probes do not seriously perturb the plasma.

2.2.3 Data acquisition

Experimental data is observed by 16 ch 12 bit digital oscilloscope (YOKOGAWA DL750) and directly stored to the hard disk drive of a PC, and analyzed by a software (WAVEMATRIX IGOR Pro®).

Chapter 3

Confinement of toroidal electron plasma

In order to test the fundamental properties of plasmas with internal electric field in an internal conductor device, pure electron plasma is trapped on Proto-RT and its confinement properties are investigated. The toroidal magnetic-surface configuration shows excellent confinement properties for non-neutral plasmas when the potential profiles of the plasma are adjusted to the contours of the magnetic surfaces. As well as the first step toward the realization of non-neutralized and flowing high β plasmas, it also provides a trap configuration for various kinds of charged particles. Experiments of toroidal electron plasma in Proto-RT, including the potential structures and its modification, confinement properties, and characteristics of the electrostatic fluctuations are described in this chapter.

3.1 Electron injection and potential structures

3.1.1 Potential structures

As described in the previous section, electron plasma is generated by gun injection from LaB_6 cathode into static electric and magnetic fields in Proto-RT. During the electron injection phase, potential profiles are measured by high-impedance emissive Langmuir probes. Figure 3.1 shows the structures of the internal electric potential in the poloidal cross section of the device during the electron injection (the injection period was 100 μs). Potential profiles when the IC electrode is grounded is shown in Fig. 3.1 (a). Poisson equation was solved in the geometry of Proto-RT [89], and we may reproduce the measured potential profile, assuming an electron cloud with a peak number density of 1×10^{13} m^{-3} and a total space charge of 3×10^{-7} C. When $V_{IC} = -300$ V, the peak density and total charge are estimated to be 1×10^{13} m^{-3} and 4×10^{-7} C, respectively. The high density region of the electron plasma is relatively remote from the support rods of the internal conductor throughout the experiments, and these structure does not seriously perturb the electron plasmas so long as the electrons rotates in the toroidal direction.

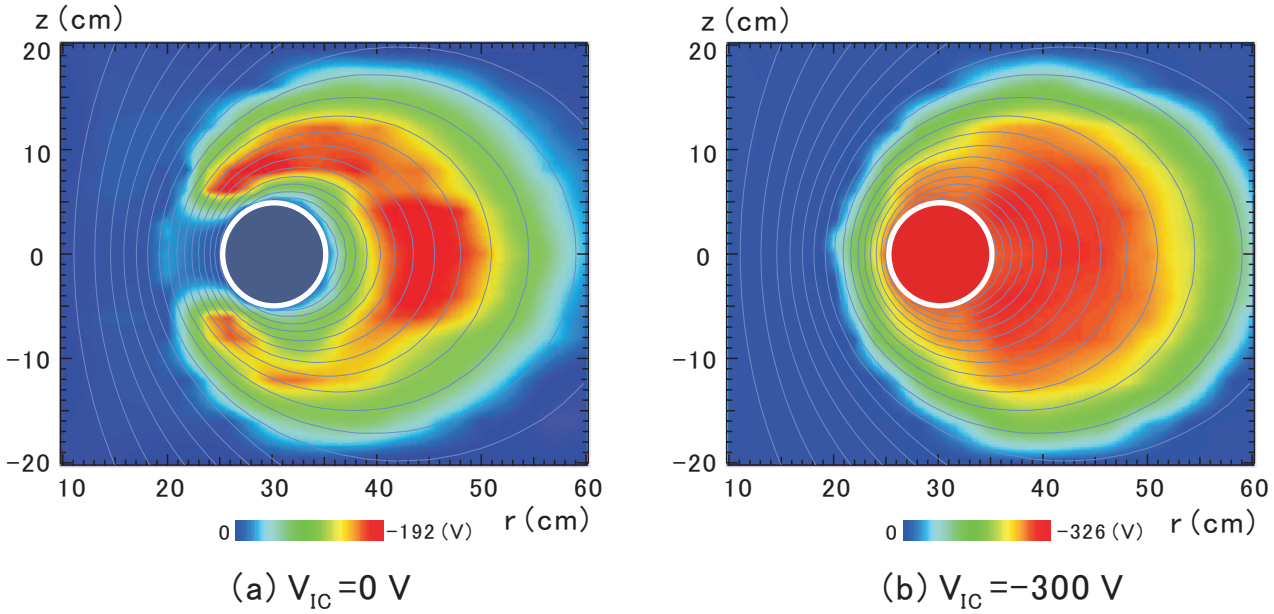

Figure 3.1: Potential profiles of an electron plasma in a poloidal cross section of the Proto-RT (a) when the potential is not controlled: IC electrode is grounded: $V_{\mathrm{IC}} = 0$ and (b) when the IC electrode is negatively biased: $V_{\mathrm{IC}} = -300$ V. The profile images are reconstructed from 284 data points measured shot by shot. The thin lines show the magnetic surfaces. Base pressure $P_{\mathrm{base}} = 8 \times 10^{-5}$ Pa and typical magnetic field strength $B_{\mathrm{typ}} = 1.3 \times 10^{-2}$ T.

When the potential is not externally controlled (the IC electrode is grounded) in Fig 3.1 (a), the distribution has a reversed “C” shape and the potential contours show strong disagreement with the magnetic surfaces of the dipole field configuration. Thus the potential contours without electrode bias do not coincide with the magnetic surfaces, implying a rapid particle loss across the field lines. When temperature and neutral collisional effects are neglected in the force balance equation of the equilibrium state of the electron plasma,

$$\nabla p = -en_{\mathrm{e}}(\mathbf{E} + \mathbf{v} \times \mathbf{B}) - m_{\mathrm{e}} n_{\mathrm{n}} \nu_{\mathrm{en}} \mathbf{v},$$

the perpendicular velocity of the electron is given by the $\mathbf{E} \times \mathbf{B}$ drift motion, and the electrostatic potential ϕ must be constant on a magnetic surface in the equilibrium states [54]: $\mathbf{B} \cdot \nabla \phi = 0$. Here p is electron pressure, m_{e} is electron mass, n_{n} is the number density of residual neutral gas, and ν_{en} is electron-neutral collision frequency.

If this is the case during the electron injection in the present experiment, where the electron number density is far below the Brillouin density limit of $n_{\mathrm{B}} \sim 10^{14}$ m^{-3} and electron temperature is relatively low (less than $T_{\mathrm{e}} \sim 50$ eV [82]), the disagreement of the contours of ϕ and ψ (magnetic flux) when $V_{\mathrm{IC}} \geq 0$ implies that thermalized (low energy) electrons are not confined when the potential is not externally controlled. The injected electron beam current when $V_{\mathrm{IC}} = 0$ V is $I_{\mathrm{beam}} =$

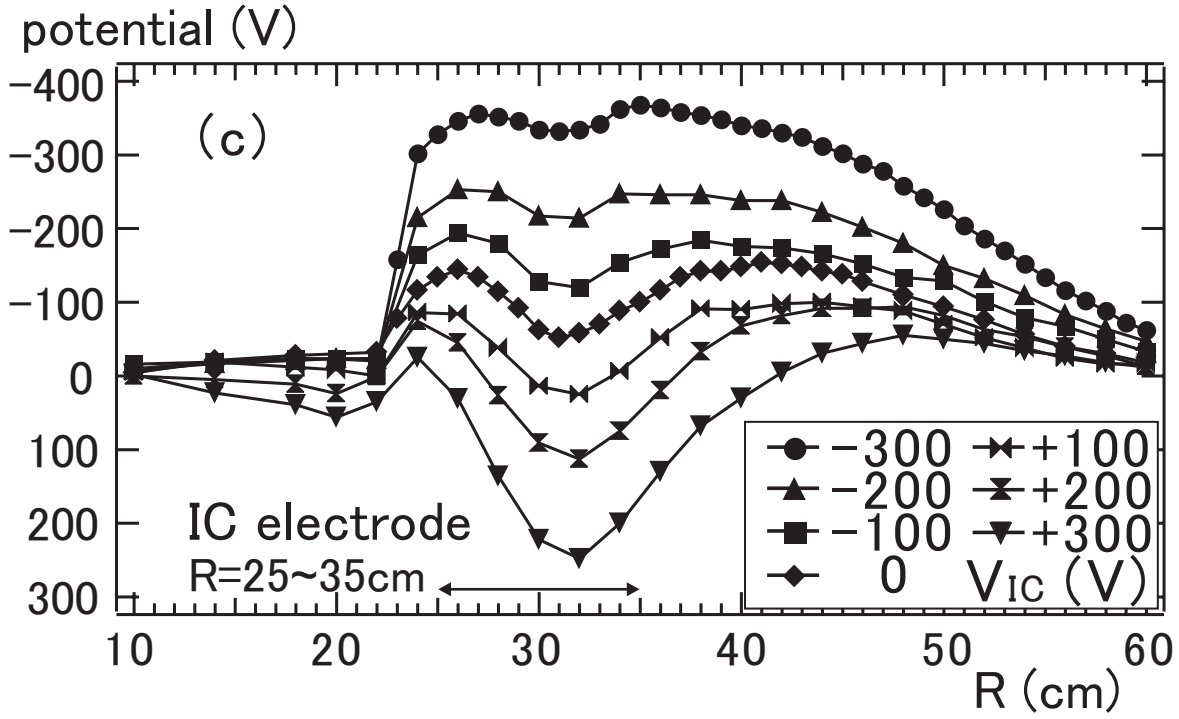

Figure 3.2: Radial potential profiles at Z = +6 cm in the variation of the potential of the IC electrode, $V_{\rm IC}$. Electrons are injected by an acceleration voltage of $V_{\rm acc}$ = 300 V.

26 mA, and it is an order of magnitude larger than when $V_{\rm IC} = -300$ V, also may suggesting that stable confinement is not realized unless the IC electrode is negatively biased.

3.1.2 Potential control by electrode bias

In contrast, when the IC electrode is negatively biased, the potential profile was successfully modified. Figure 3.1 (b) shows the potential profile when $V_{IC} = -300$ V, the same potential as the acceleration voltage of the electron gun. The potential hall near the IC electrode is eliminated, and the potential contours surround the IC, which is topologically close to the shape of the magnetic surfaces. Figure 3.2 shows the radial potential profiles at Z = +6 cm, just above the surface of IC electrode). The grounded or positively biased IC yields a hollow potential, resulting in a strong $\mathbf{E}\times\mathbf{B}$ flow shear that may destabilize the Kelvin-Helmholtz (diocotron) modes. By negatively biasing the IC electrode, the hollow structures are cancelled as illustrated in the figure, and it might lead to stabilize the diocotron instability of non-neutral plasmas. As described in the next subsection, the measurements of electrostatic fluctuation show that the confinement time is enhanced for more than an order of magnitude by the negative bias of the IC.

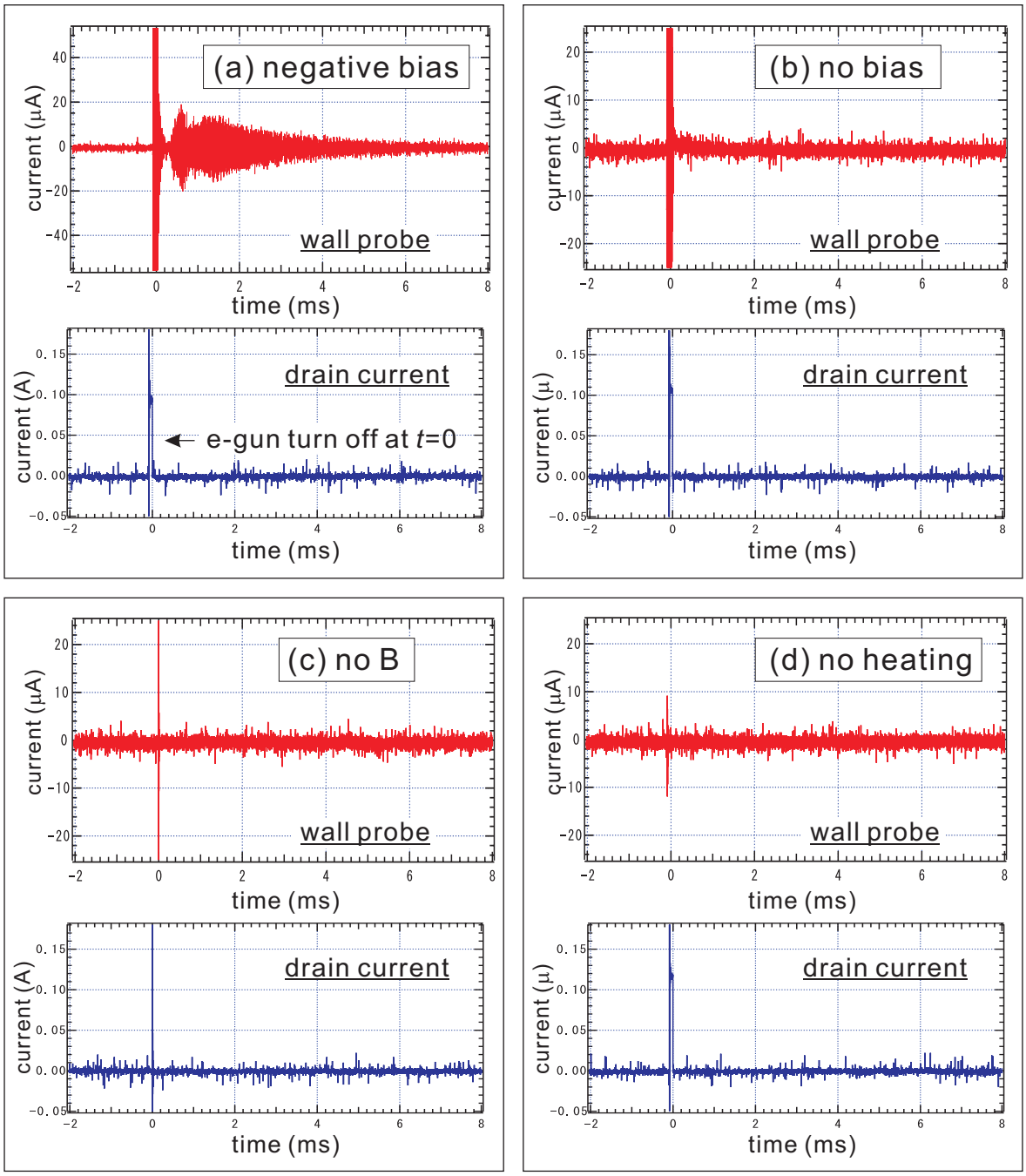

Figure 3.3: Conditions for the stable confinement of electron plasmas. After the electron gun is turn off at $t = 0$ s, (a) initial large fluctuation is damped and stable oscillation mode appears when the IC electrode is negatively biased. When (b) the IC electrode is grounded, (c) $V_{IC} < 0$ but no magnetic field, or (d) cathode is not heated, long lasting oscillation mode is not observed in the wall probe signal.

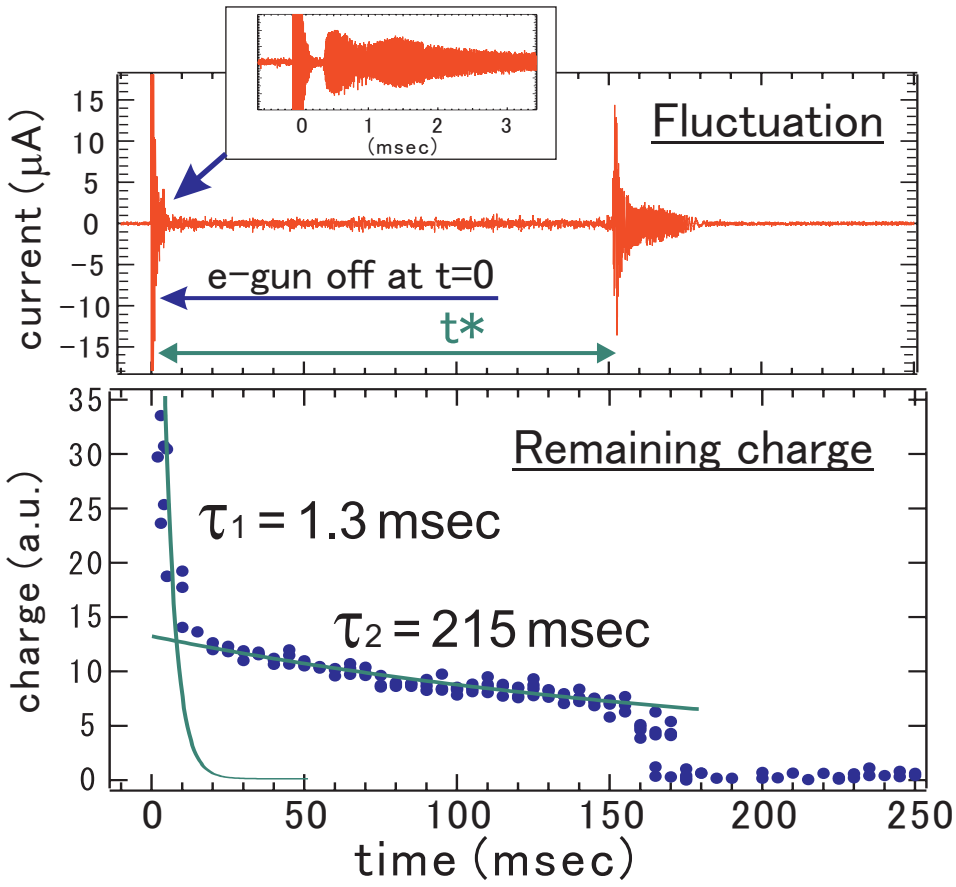

Figure 3.4: (a) Waveform of the wall probe signal. (b) Decay of the charge on the wall probe. The IC electrode was biased to −300 V. The gun was terminated at $t = 0$. $P_{\text{base}} = 8 \times 10^{-5}$ Pa and $B_{\text{typ}} = 1.3 \times 10^{-2}$ T.

3.2 Life time of electron plasma

Long term confinement of toroidal electron plasma was experimentally demonstrated in the magnetic surface configuration in the Proto-RT device with a negatively biased electrode [91]. Experimental observations on the confinement properties are described in this section.

3.2.1 Potential optimization and confinement properties

Figure 3.3 shows the examples of electrostatic fluctuations and drain currents from the electron gun, during and after the electron injection. Electrons are injected into a DC dipole magnetic field generated by the internal conductor current of $I_{\text{IC}} = 5.25$ kAT, from $t = -100$ μs to 0 μs. Wall probe is located at $R = 46$ cm. As described in Fig. 2.12, the gun is turn off in the time constant of ~ 1 μs. When the IC electrode is grounded in Fig. 3.3 (b), the initial fluctuation decays typically in a time constant of ~ 10 μs, and no electrostatic signals are observed after this period. By negatively

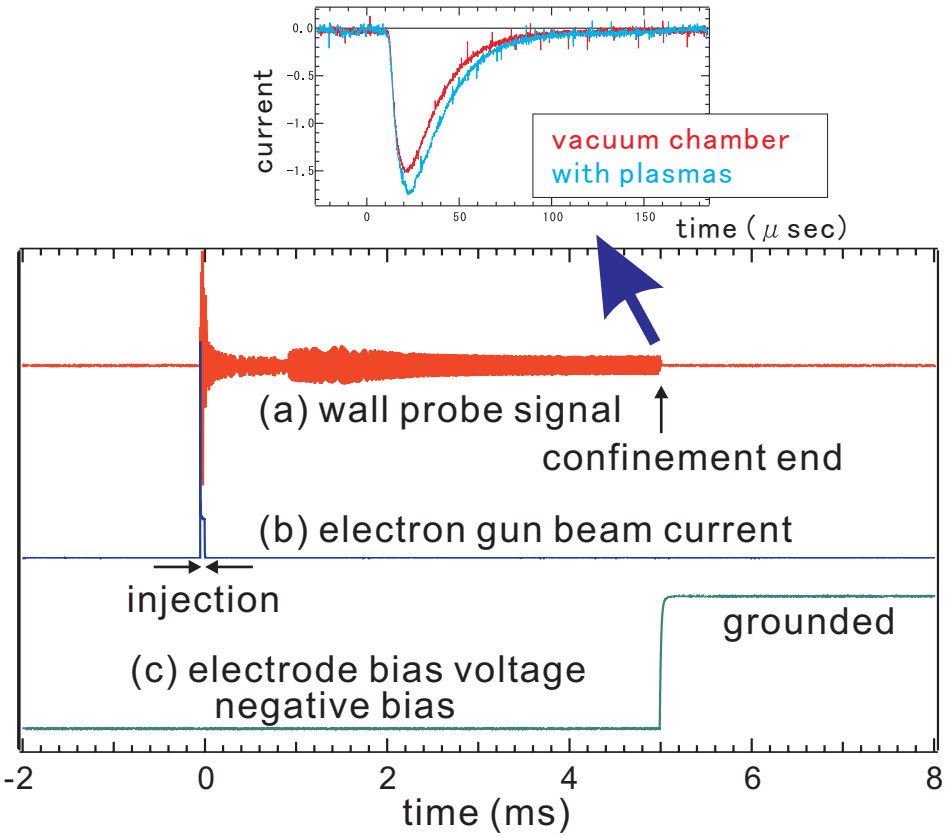

Figure 3.5: Temporal scheme of "destructive" measurement of electron plasma. (a) Electrostatic fluctuation measured by a wall probe, (b) injected electron beam current, and (c) bias voltage of the IC electrode V_{IC}.

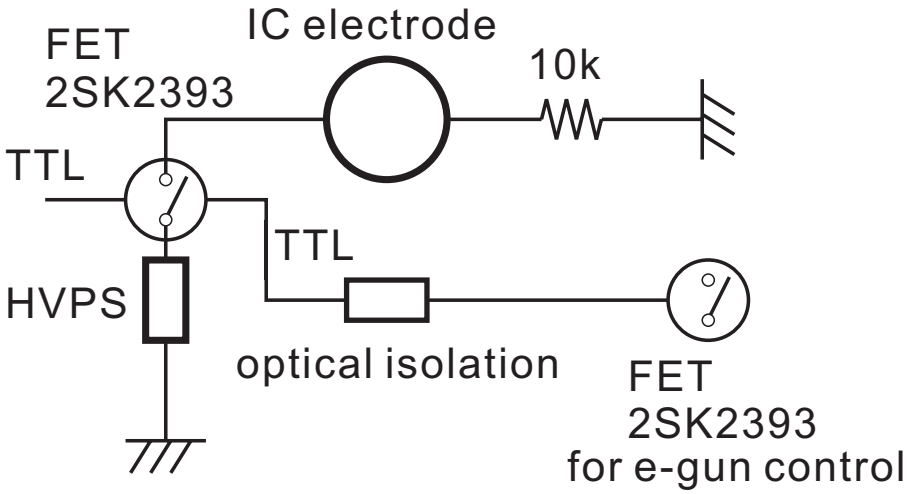

Figure 3.6: Diagram of the control of electron gun and electrode bias used in Fig. 3.5. Internal drive circuit of the FET switch is shown in Fig. 2.11.

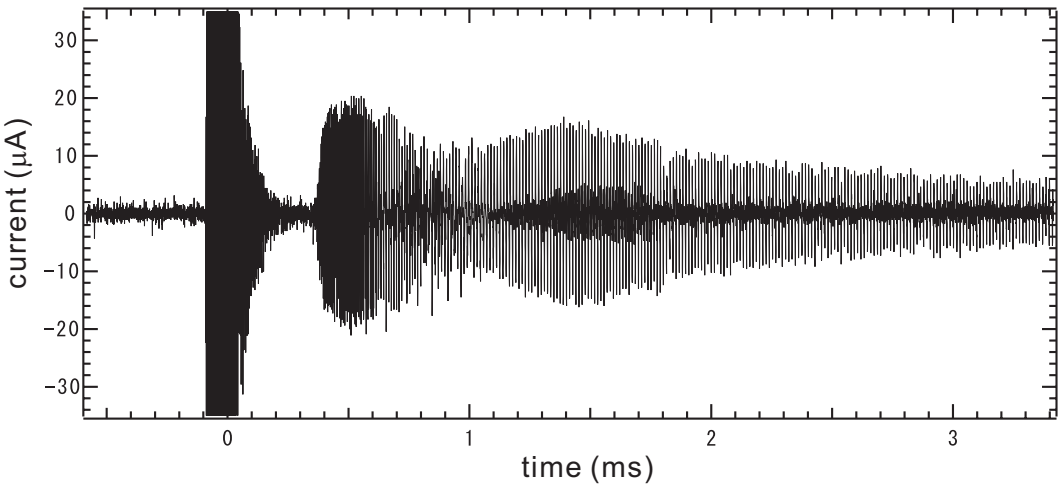

Figure 3.7: Temporal evolution of the electrostatic fluctuation of toroidal electron plasma.

biasing the IC electrode, some of the trapped electron charge remains after $t = 0$ in Fig. 3.3 (b), and temporal evolutions of the signal are explained in the following subsections.

3.2.2 Fluctuation and trapped charge decay

An example of the detected fluctuations is shown in Fig. 3.4 (a) for the case of negatively biased IC. During the electron injection ($t = -100$ μs to 0), we observe large, almost coherent amplitude oscillations. The dominant frequency is 510 kHz which corresponds to the diocotron frequency (discussed below). After the electron injection was stopped, the amplitude of the oscillations decreases exponentially with a time constant of 20 μs, and then, some quiescent periods follow. The stable phases appear when the magnetic field is stronger than $\sim 10^{-2}$ T (measured at the edge of the confinement region) and $V_{IC} \leq -10^2$ V. The life time of the first stable phase is at most 0.4 ms. Near the end of the quiescence, fluctuations grow rapidly. The fluctuations quench again when the frequency drops down to 43 kHz ($t = 0.7$ ms). The second quiescent phase lasts relatively long at more than 10^{-1} s. The typical time constant of the growth rate of observed fluctuations at the termination phase was 100 μs. One of the possible reasons for the onset of fluctuations is ion resonance instability caused by the ionization of neutral background gas [34, 93, 94]. When the IC electrode is grounded, and thus the initial potential profile does not coincide with the magnetic surfaces, such kinds of long-lasting signals are not observed, and trapped charge decays away in a time constant of about 10 μs after the stop of the electron supply.

Figure 3.4 (b) plots the charge on the wall probe as a function of time. The data were accumulated for many shots; each shot was artificially terminated by turning off the control electric potential V_{IC}, and the remaining charge on the wall probe was measured. Scheme for such operation and control circuit for the bias drive are shown in Figs. 3.5 and 3.6. In the initial phase

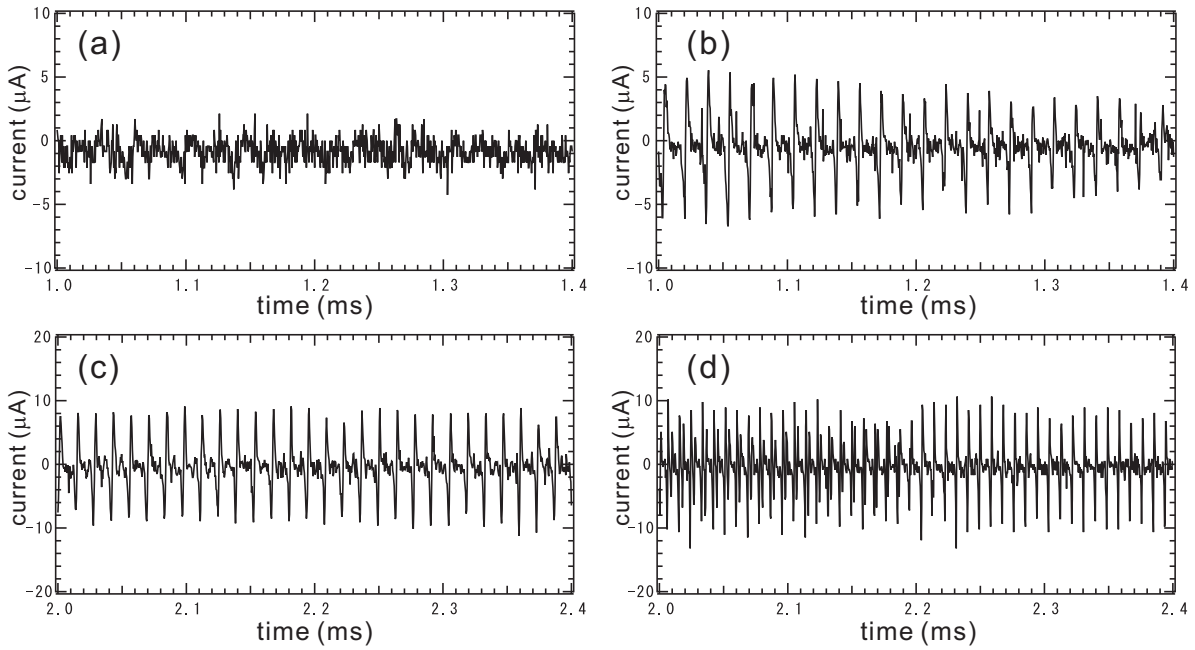

Figure 3.8: Wall probe signals in the variation of applied external electric field. The bias voltages of the IC electrode are (a) $V_{\mathrm{IC}} = -50$ V, (b) $V_{\mathrm{IC}} = -150$ V, (c) $V_{\mathrm{IC}} = -250$ V, and (d) $V_{\mathrm{IC}} = -300$ V.

($t \leq 1$ ms), the charge decreases from 4.5×10^{-10} C to 1.4×10^{-11} C with a time constant of 1.3 ms. During the quiescent phase ($t \sim 2$ ms), we observe a much slower decay of the charge; The time constant of the decay is 0.2 s. Usually, the plasma confinement terminates with disruptive instability around $t \sim 0.1$ s (the time of disruption will be referred to as "the life time").

3.2.3 Frequencies of electrostatic fluctuations

As shown in Fig. 3.7, growth of the fluctuation amplitude tends to saturate when the frequency of the first fluctuation decreased to a certain value. The dominant frequency of the fluctuations at this period is shown in Fig. 3.8 as a function of applied external electric field. By taking the dependence on both external electric and magnetic fields, the frequency is inversely proportional to the magnetic field strength B and also to V_{IC} as shown in Fig. 3.9. After the first oscillation decays, second signals appears with some temporal interval as shown in Fig. 3.10. Although the decrease rate is small compared with during the large fluctuation, the fluctuation frequency is decreasing during the stable confinement phase.

The properties of electrostatic frequencies suggest that the observed electrostatic fluctuations are due to the diocotron oscillations. However, a direct correlation between frequency and density cannot easily be drawn, because our system has an inhomogeneous magnetic field and complicated conducting boundaries. Here we borrow the empirical formula for the $l = 1$ diocotron oscillation

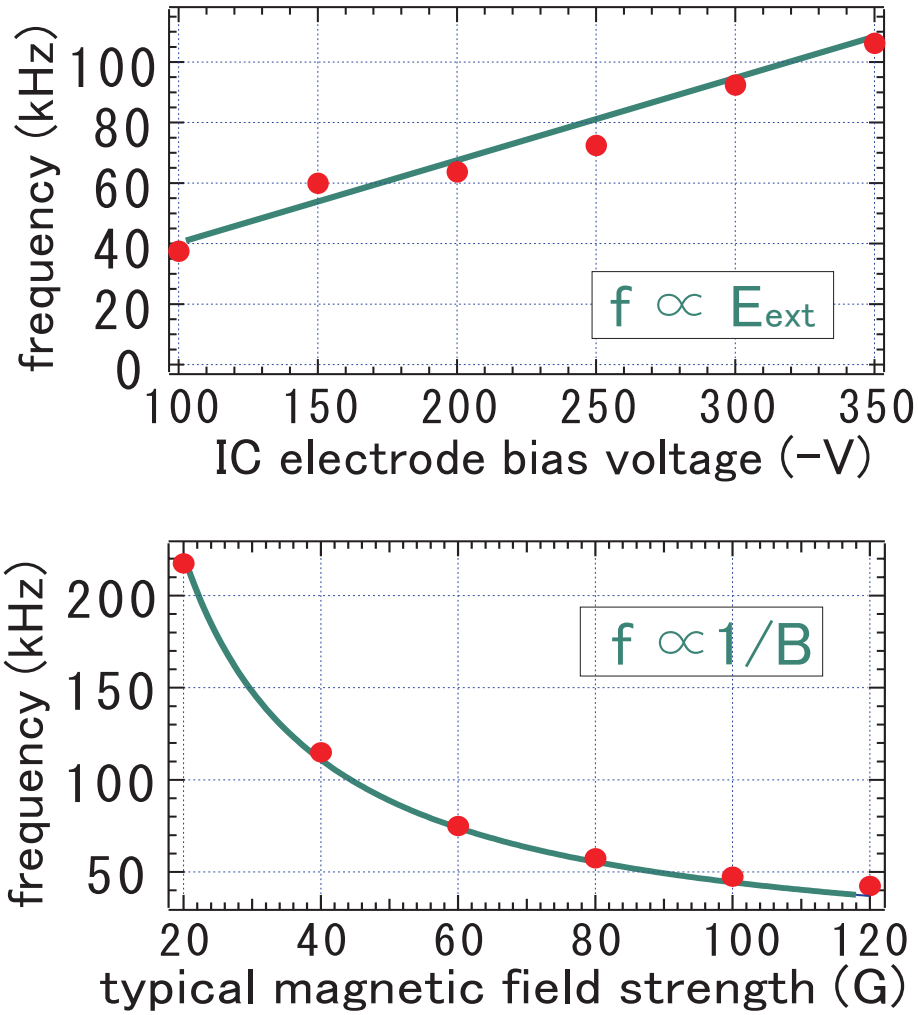

Figure 3.9: The dominant frequency of electrostatic fluctuations (just before the quiescent phase) as functions of (a) the typical strength of dipole magnetic field B (at $r = 40$ cm) and (b) potential of the IC electrode $V_{\rm IC}$. $P_{\rm base} = 8\times10^{-5}$ Pa, (a) $V_{\rm IC} = -250$ V, and (b) $B_{\rm typ} = 6.0\times10^{-3}$ T.

in a toroidal electron plasma due to Daugherty *et al.* [33], i.e., $f \approx Q/(8\pi^3 R a^2 \varepsilon_0 B)$, where Q is the total charge, R (a) is the major (minor) radius of the toroid, ε_0 is the vacuum dielectric constant, and B is the magnetic field strength at $r = R$. Then, the total charge is estimated to be $\sim 1\times10^{-7}$ C for the electron injection phase.

In the geometry of Proto-RT, the large amount (up to $\sim 90\%$) of electric field by trapped electrons are cancelled due to the image charges on the internal conductor. Although the exact profiles of plasmas after the stop of electron injection are not known at present, but the image charge effect might lead to underestimate the trapped charge calculated from the frequency. The estimated charge is fairly consistent with the above mentioned result from the Langmuir probe measurements. In the quiescent phase ($t = 0.7$ ms), we obtain $Q \sim 1\times10^{-8}$ C.

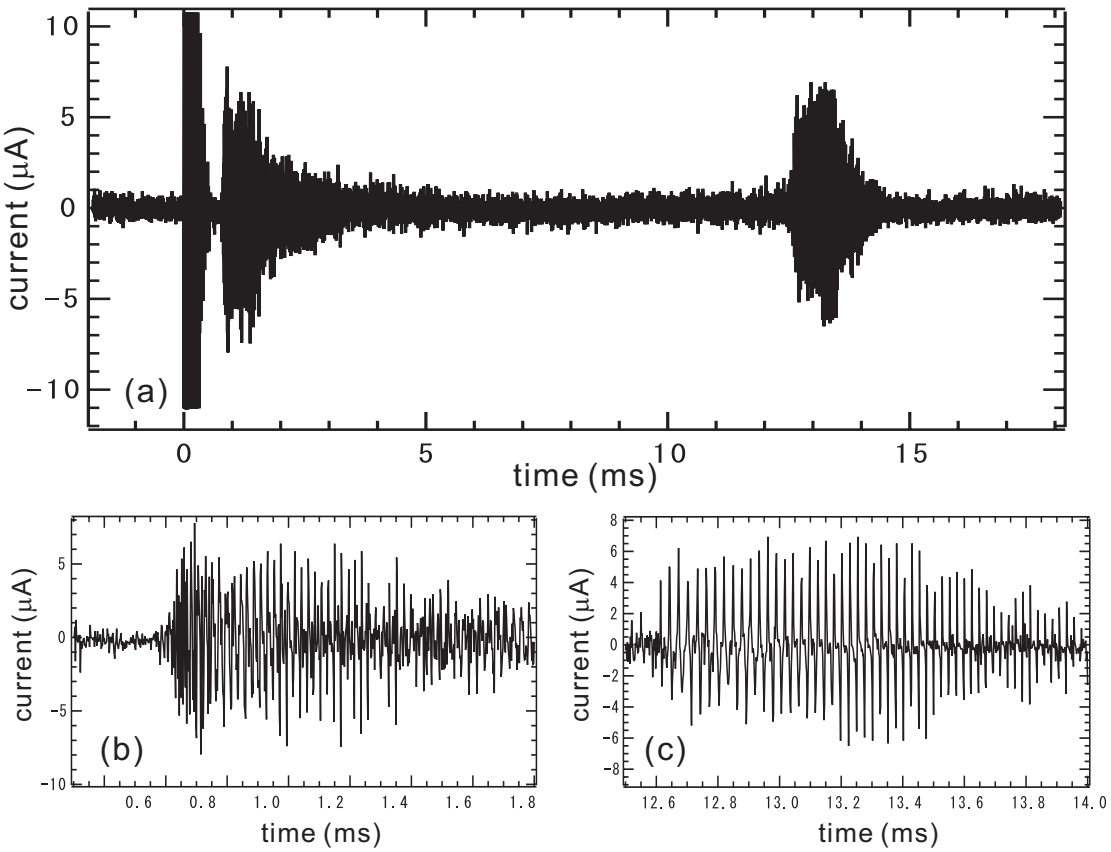

Figure 3.10: Initial damp and re-growth of the electrostatic fluctuation.

3.2.4 Life time of electron plasma

Using the formula of the diffusion time due to neutral collisions [95] $\tau_D \approx \nu_{en}^{-1}\lambda_D^2 r_L^{-2}$ (ν_{en}: mean collision frequency, λ_D: Debye length, r_L: Larmor radius) and the experimental parameters $B \sim$ 0.01 T, electron temperature $\sim$ 1 eV, and a density of $n_e \sim 10^{12}$ m^{-3}, we estimate $\tau_D \approx 0.1$ s. The classical diffusion time τ_D is comparable to the experimental results of both "life time" and decay time of the charge. The life time t^* varies as a function of the background pressure (P, Fig. 3.11) and the magnetic field (B), suggesting the limit of the present confinement time is set by the effects of neutral collisions. We observe $t^* \propto P^{-1}B^{2.5}$, as shown in Fig. 3.12, and the use of higher vacuum and increase of the magnetic field strength would make possible the further longer confinement of electron plasmas. While the confinement time is close to the classical diffusion time, the scaling of the life time t^* shows a difference from the simple classical diffusion relation ($\propto P^{-1}B^2$), suggesting onset of some instability (like the ionization instability). Detailed analysis of fluctuations and scaling laws will be reported elsewhere.

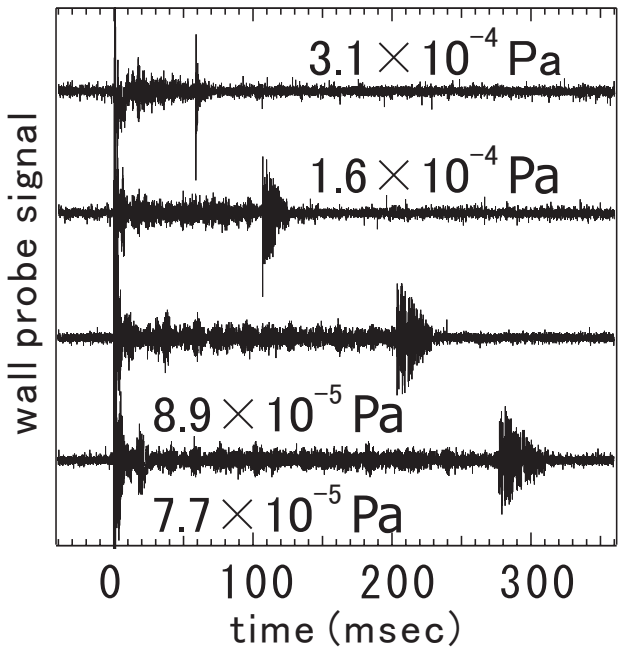

Figure 3.11: Wall probe signal as a function of neutral gas pressure. Electrons are injected from $t = -100$ to 0 μs.

3.2.5 Disturbance due to Langmuir probes

During the electron injection phase, the loss of electrons through the Langmuir probe was of the order 1 μA, and it is negligibly smaller than the injected electron beam current. However, in a quiet trap phase, Langmuir probes located in the confinement region are serious obstacle for the realization of stable confinement. As shown in Fig. 3.13, the life time of the electron plasma is strongly affected by the insertion of the probes, and the probe insertion induces the growth of instability at the early stage of the confinement. As shown in the figure, when the probe tip is located at $R \leq\sim 45$ cm (inside the confinement region), no stable equilibrium was obtained. Thus the perturbation due to the probing is a serious problem for estimating the confinement time after cutting off the gun injection. For this purpose, we have used wall probes [35] that measure the image charges induced by electron plasmas. A sensor foil (copper sheet of 5 mm $\times$15 mm) was installed in an insulating quartz tube, and was placed just outside the confinement region. The foil was electrically connected to the chamber through a current amplifier, and the image current was measured. Oscillations in the image currents indicate electrostatic fluctuations, giving an evidence for the plasma. In order to evaluate the charge confinement time more explicitly, we destroy the equilibrium by dropping the electrode potential and detecting the escaping image charges.

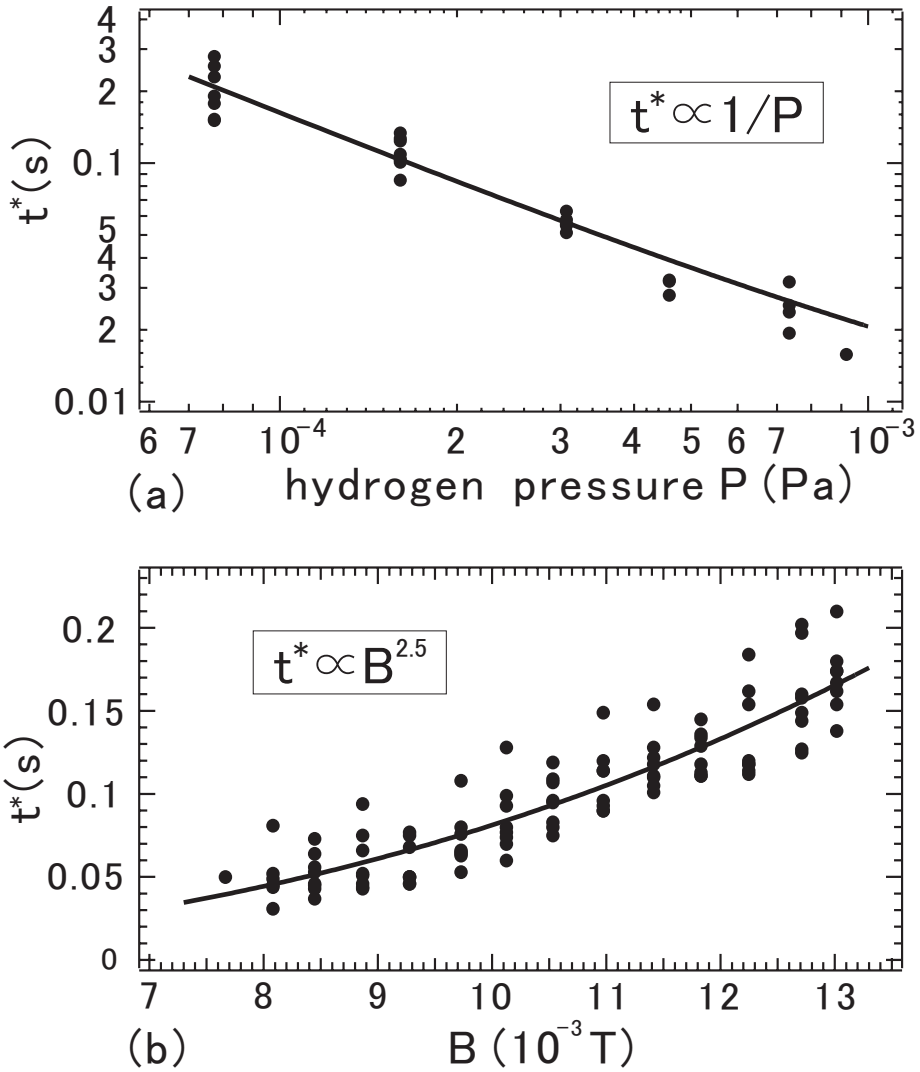

Figure 3.12: The life time t^* as functions of (a) the back pressure of hydrogen gas and (b) typical magnetic field strength B. $P_{base} = 8 \times 10^{-5}$ Pa, (a) $B_{typ} = 1.3 \times 10^{-2}$ T, and (b) $V_{IC} = -300$ V.

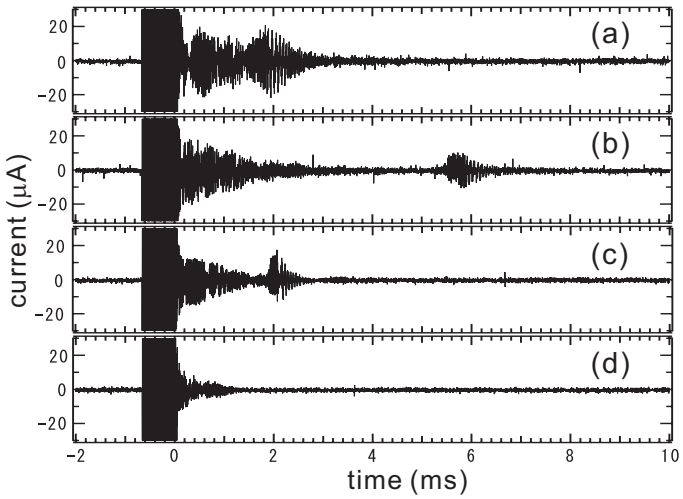

Figure 3.13: Langmuir probe insertion and stable confinement time. The probe tip is located at (a) R = 60 cm, (b) R = 50 cm, (c) R = 45 cm, and (d) R = 40 cm.

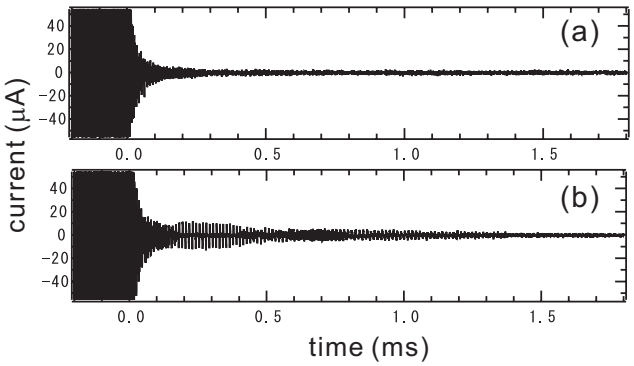

Figure 3.14: Wall probe signals when the inserted Langmuir probe is (a) grounded and (b) floating. The Langmuir probe is located at R = 45 cm.

3.3 Stable trap and confinement time

In the previous section, basic experimental results of toroidal electron plasma (conducted from 2002 to February 2003) were summarized. In this period, the confinement ended with sudden growth of instability and stable decay of the trapped charge was not observed. Some reconfiguration of the measuring instruments, carried out after this period, has realized the stable confinement of electron plasma in the experiments in second period (from May 2004 to October 2004) [92]. The obtained results on the confinement properties of plasmas are described in this section.

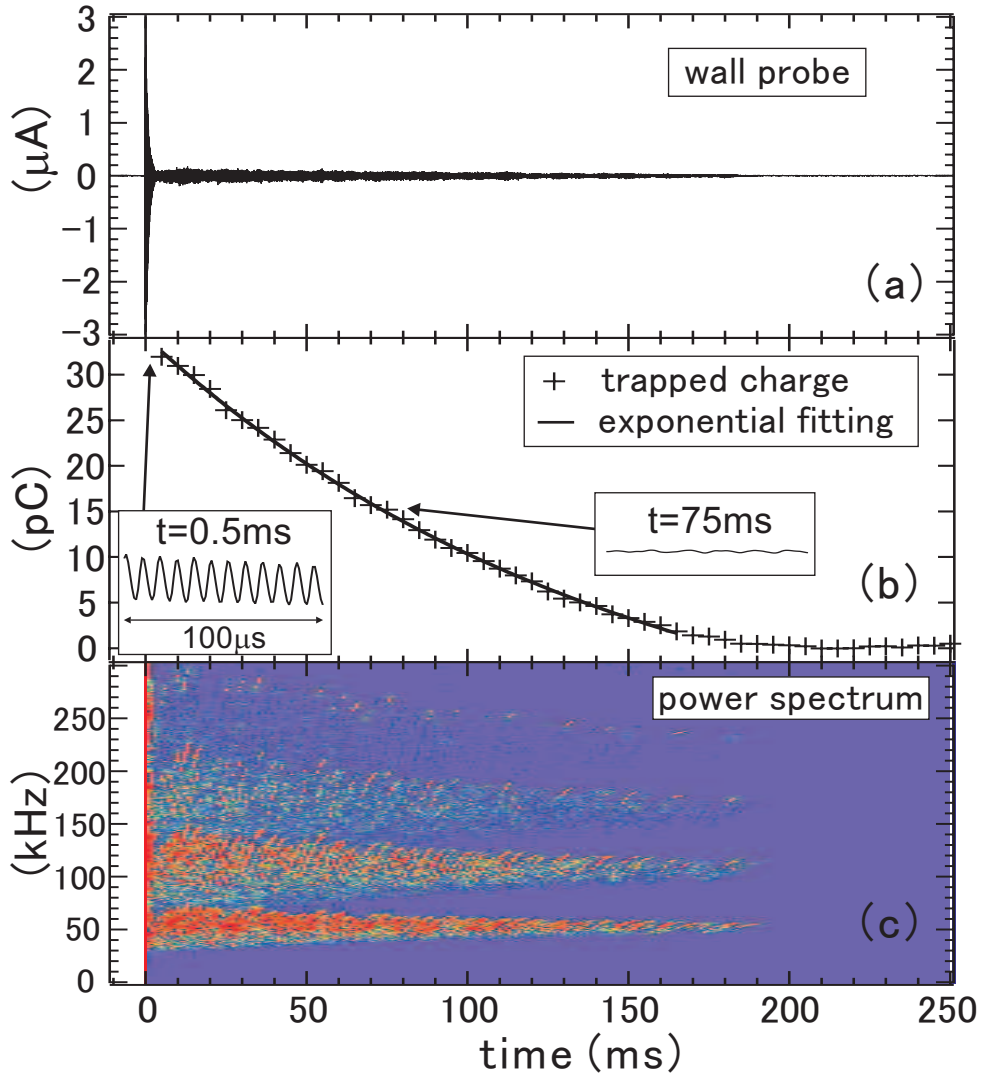

Figure 3.15: (a) The typical waveform of a wall probe signal, (b) remaining charge on a wall and horizontal enlargement (for 100 μs) of the fluctuations of remaining charge (small boxes, same vertical scale), and (c) power spectrum of the wall signal, when the IC electrode is biased to −300 V. The electron gun was operated from $t = -100$ to 0 μs.

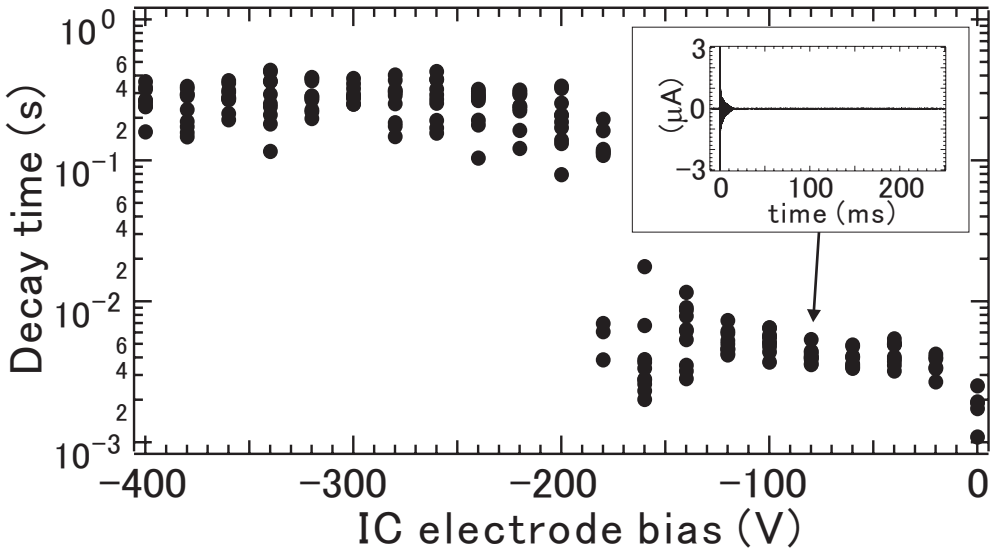

Figure 3.16: Confinement time as a function of the bias voltage of the IC electrode, V_{IC}, and waveform of the wall when $V_{IC} = -80$ V.

3.3.1 Confinement time

The temporal evolution of the electron plasma is investigated by measuring the electrostatic fluctuations. Figure 3.15 shows the typical waveform of the wall probe when $V_{IC} < 0$ V, together with the trapped charge on the wall and power spectrum of the fluctuation. Electrons are injected with an acceleration voltage of 300 V from $t = -100$ to 0 μs, into DC magnetic and electric fields generated by a dipole filed coil current of $I_{IC} = 7$ kAT (magnetic field strength at $R = 40$ cm is 70 G) and electrode bias voltages of $V_{IC} = -300$ V and $V_{CS} = 0$ V. After the electron gun is turn off at $t = 0$ s, a large oscillation during the electron injection phase decays typically in a time constant of ~ 1 ms. Subsequently, a quiet oscillation mode is realized only when the IC electrode is negatively biased. The wall signals before and after the stabilization of the initial large fluctuation are shown in the small boxes in Fig. 3.15 (b). The magnitude of the electrostatic fluctuation before and during the quiet mode normalized by the DC electrostatic potential in the plasma is $\tilde{\phi}/\phi = 12$ % and 0.6 %, respectively. In the quiet confinement phase, the remaining charge drops approximately exponentially as indicated in Fig. 3.15 (b). As the plasma enters the quiet confinement mode, the frequency of oscillation, illustrated in Fig. 3.15, decreased from 240 kHz to 62 kHz. In the quiet confinement phase, the decrease of the frequency is relatively small, and the peak of the fundamental frequencies in the power spectrum are 62 kHz at $t = 5$ ms and 57 kHz at $t = 180$ ms, indicating that both self and external electric fields decide the frequencies of the electrostatic oscillation.

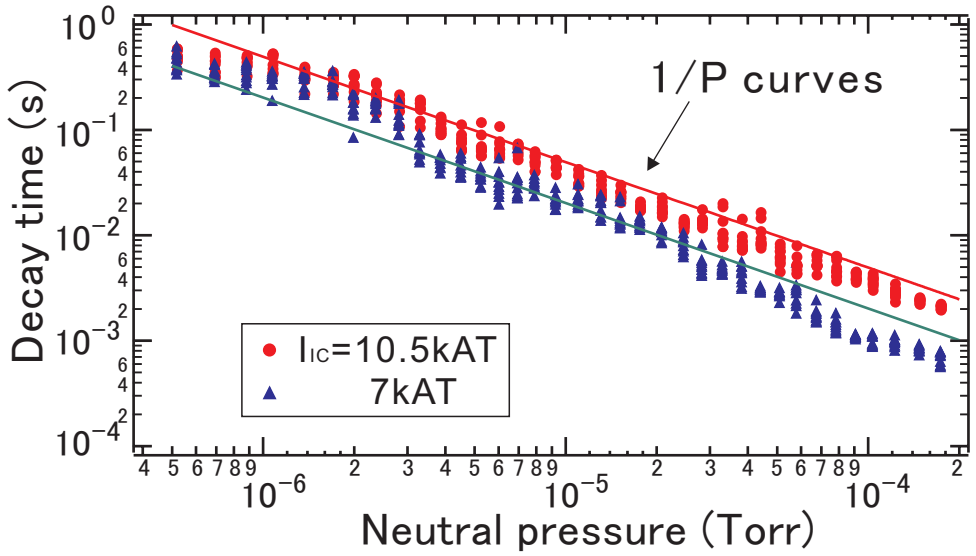

Figure 3.17: Confinement time as a function of added neutral gas (hydrogen) pressure. I_{TR} = 10.5 kAT, V_{IC} = −300 V.

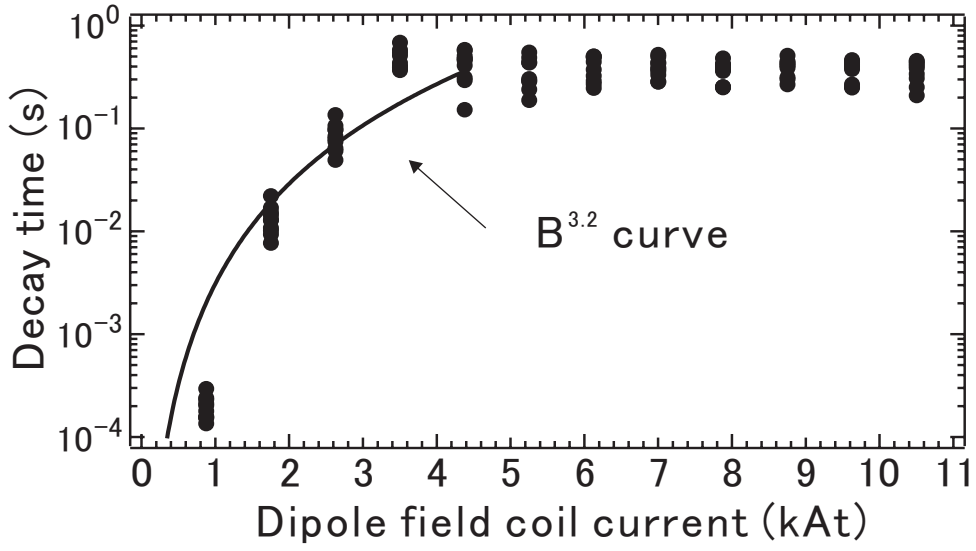

Figure 3.18: Confinement time as a function of dipole magnetic field strength.

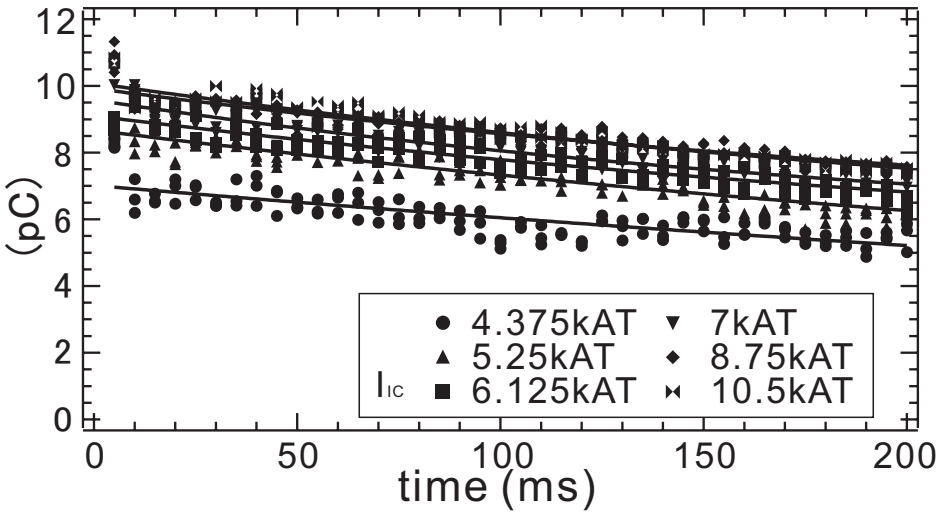

Figure 3.19: Decay of trapped charge on the wall in the variation of the dipole field coil current.

3.3.2 Confinement time scalings

The confinement time of the particles (time constants of the exponential fitting curves) as a function of $V_{\rm IC}$ is shown in Fig. 3.16. When $V_{\rm IC}$ is above -180 V, the initial fluctuation of the plasma does not enter a quiet state and the charge decays within some milliseconds. As shown in the small box in Fig. 3.16, the amplitude of the initial fluctuation when $V_{\rm IC} = -80$ V is $\tilde{\phi}/\phi = 32$ % and it decays without entering the quiet confinement mode. As indicated in Fig. 3.2, the drastic improvement of the confinement is observed when the hollow potential structure is eliminated by the sufficient bias voltage of the IC electrode.

Figure 3.17 shows the confinement time τ of electrons as a function of background neutral gas (hydrogen) pressure P. At the base pressure of 4×10^{-7} Torr and the maximum dipole field coil current of 10.5 kAT, the obtained confinement time is $\tau = 0.5$ s.

Assuming that the loss of electrons is caused by the collisions with neutral atoms, the force balance equation of electrons in the confinement phase is given by

$$qn(\mathbf{E}+\mathbf{v}_{\rm e}\times\mathbf{B}) - m_{\rm e}n_{\rm e}\nu_{\rm en}\mathbf{v}_{\rm e} = 0.$$

Here the small inertia term is neglected. When the confinement time of electrons is determined by the loss of the momentum of toroidal $\mathbf{E}\times\mathbf{B}$ motion due to the collisions with neutral gas molecules, the toroidal viscous force is balanced by the Lorentz force caused by the outgoing radial velocity of electrons:

$$0 = -en_{\rm e}v_{\rm r}B - m_{\rm e}n_{\rm e}\nu_{\rm en}(v_{\rm t}-v_{\rm n}),$$

where e is charge, $v_{\rm r}$ and $v_{\rm t}$ are radial and toroidal speed of electrons, $m_{\rm e}$ is electron mass, $n_{\rm e}$ is electron density, v_n is the velocity of neutral atom, $\nu_{\rm en} = n_{\rm n}\sigma v_{\rm t}$ is the electron-neutral atom mean

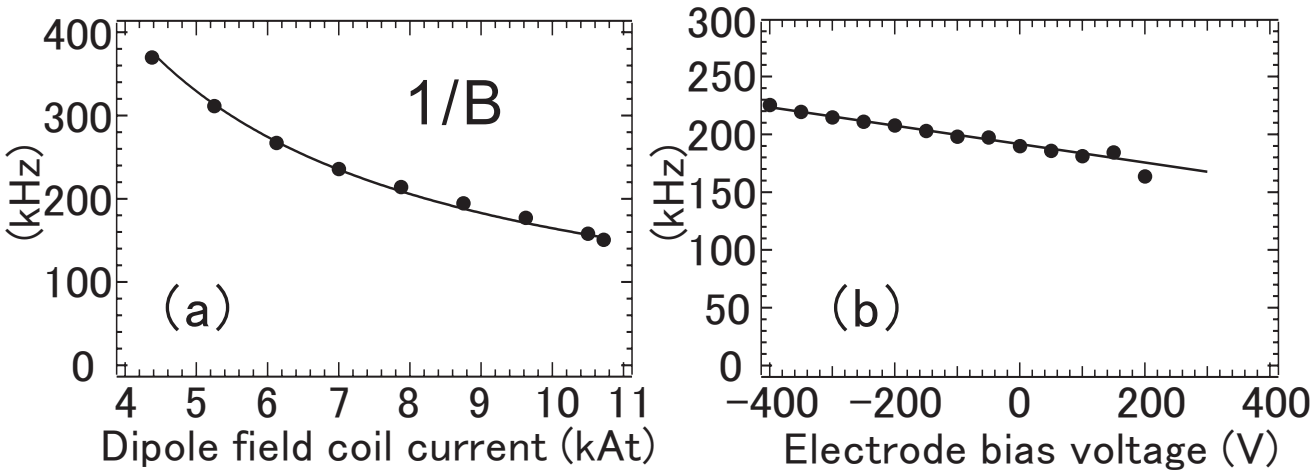

Figure 3.20: Fundamental frequencies of wall probe signal during the electron injection, in the variation of (a) dipole magnetic field strength and (b) bias voltage of the IC electrode, V_{IC}.

collision frequency, n_{n} is neutral gas density, and σ is the collision cross section. Assuming that $v_{\mathrm{n}} = 0$, the radial outgoing velocity of the electrons is given by

$$v_{\mathrm{r}} = \frac{m_{\mathrm{e}} n_{\mathrm{n}} \sigma E^2}{eB^3}.$$

Taking the minor radius of the electron plasma a as the typical length, the typical diffusion time of the electrons is given by

$$\tau_{\mathrm{D}} \sim a/v_{\mathrm{r}} = \frac{eaB^3}{m_{\mathrm{e}} n_{\mathrm{n}} \sigma E^2} \propto P^{-1} B^3.$$

Substituting the experimental parameters of $B \sim 0.005$ T, $P = 10^{-6}$ Torr, $E = 3 \times 10^2$ Vm^{-1}, $\sigma \sim 10^{-19}$ m^2, and $a = 0.1$ m, the typical confinement time τ_{D} is in the order of 1 s, and it is comparable to the observed confinement time. For the pressure range of 10^{-6} to 10^{-4} Torr, τ is scaled as $\propto P^{-1}$, as shown in Fig. 3.17, indicating that the effects of residual neutral gas set the confinement time. When P is below $\sim 10^{-6}$ Torr, τ deviates from the P^{-1} line and it saturates near 0.5 s. The confinement time at the base pressure of 4×10^{-7} Torr in the variation of the dipole field coil current is shown in Fig. 3.18. Before entering the saturation region (when I_{IC} is below ~ 5 kAT), the observed τ is approximately proportional to B^3 and it also agrees with the parameter dependence of the calculated τ_{D}, but τ has an upper limit in spite of the increase of the magnetic field strength above $I_{\mathrm{IC}} \sim 5$ kAT. As indicated in the change of the electron charge in Fig. 3.19, the amount of the trapped charge as well as τ saturate above $I_{\mathrm{IC}} \sim 5$ kAT, although the obtained electron density ($\sim 10^{12}$ m^{-3}) is far below the Brillouin density limit ($\sim 10^{14}$ m^{-3}), suggesting the existence of some anomalous loss of the electrons.

In the initial large fluctuation phase just after the stop of the electron injection, charge on the wall decreased from ~ 200 pC to 32 pC, and only small fraction of electrons shows good

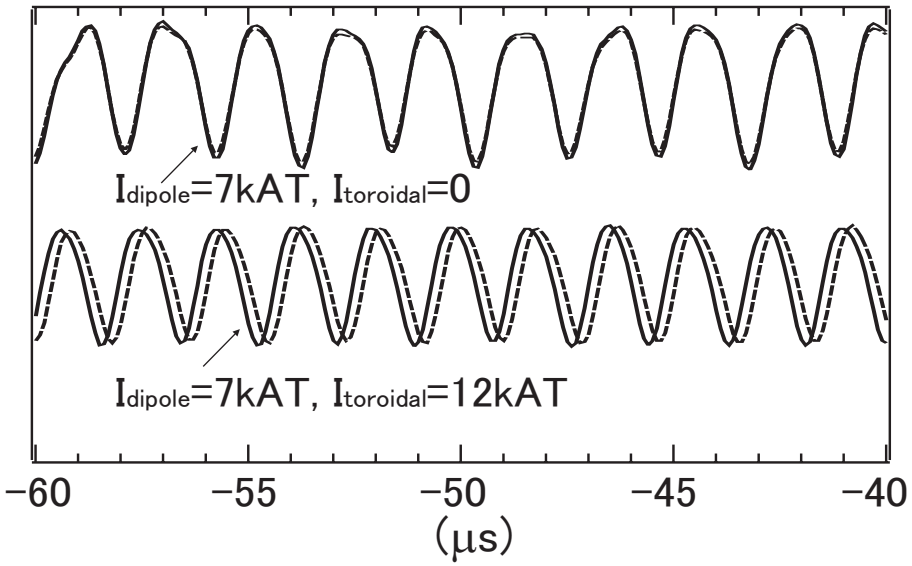

Figure 3.21: Waveforms of wall probes located at $Z = +20$ cm (solid lines) and $Z = -20$ cm (dotted lines) in the same poloidal cross section of the device. Fluctuations during the electron injection in a pure dipole field (upper lines), and dipole and toroidal fields (lower lines).

confinement properties. In comparison with the trapped charge during the electron injection calculated from the Poisson's equation, stably confined electron charge when $I_{\mathrm{IC}} = 10.5$ kAT, $P = 4\times10^{-7}$ Torr, and $V_{\mathrm{IC}} = -300$ V is estimated to be $\sim 5\times10^{-8}$ C.

3.4 Electrostatic fluctuations in toroidal electron plasma

3.4.1 Frequencies and propagation direction

The frequencies of the oscillation during the electron injection phase are shown in Fig. 3.20 as functions of magnetic field strength and V_{IC}. The frequency is inversely proportional to the magnetic field strength and it shows approximately linear dependence on the external electric fields. When the IC electrode is more positively biased than $\sim +200$ V, clear peak of frequency was not observed in the power spectrum, suggesting that the electrons are not confined as plasma.

As well as the characteristics of the fluctuation frequencies, the direction of the wave propagation also agrees with the properties of diocotron oscillation mode. The waveforms of two wall probes in pure poloidal (dipole) field and, dipole and toroidal fields configurations are shown in Fig. 3.21. The walls are located at $Z = \pm20$ cm in the same poloidal cross section of the device. In a pure poloidal magnetic field, the oscillations have no phase difference in the poloidal direction and the wave propagates in the toroidal direction. The addition of toroidal field results a phase difference between the two wall probe signals as indicated in the lower part of Fig. 3.21.

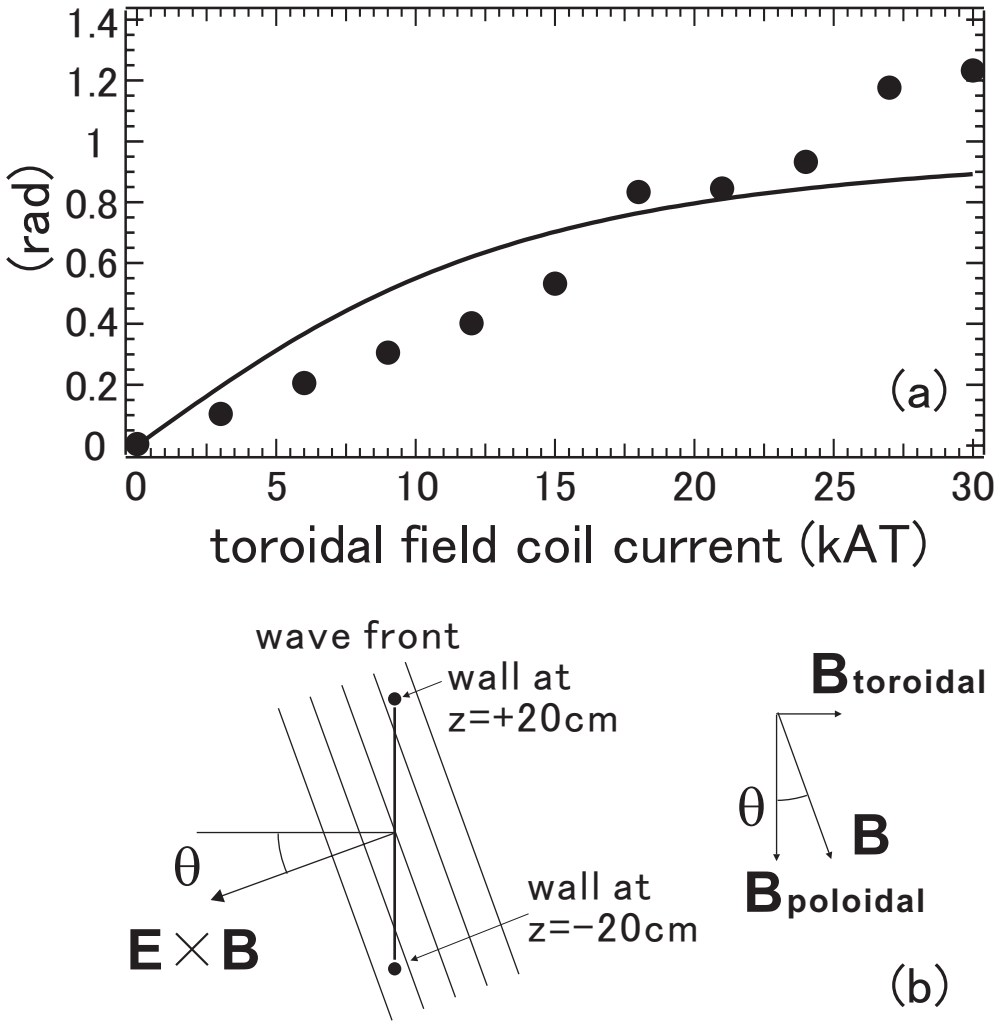

Figure 3.22: Phase difference of wall signals at $Z = \pm 20$ cm (circles) and calculated phase difference ϕ (solid line).

When observed at $Z = \pm l/2$ in the same poloidal cross section, the phase shift ϕ between two walls located in a wave propagating in the cross fields direction is given by

$$\phi = 2\pi l \sin\theta / \lambda,$$

where λ is the wave length, and θ is the pitch angle between toroidal and poloidal fields. Relation between the pitch angle and magnetic field is shown in Fig. 3.22 (b). Here the plasma shape is supposed to be azimuthally symmetric and the plasma has only radial electric field. Figure 3.22 (a) shows the observed phase difference between two walls at $Z = \pm 20$ cm in the variation of added toroidal field strength, while the strength of poloidal (dipole) field was kept constant. The solid line shows the calculated ϕ, obtained by substituting the field strength at $R = 40$ cm and taking the toroidal circumference of the device with major radius of $R = 40$ cm as typical wave length λ of

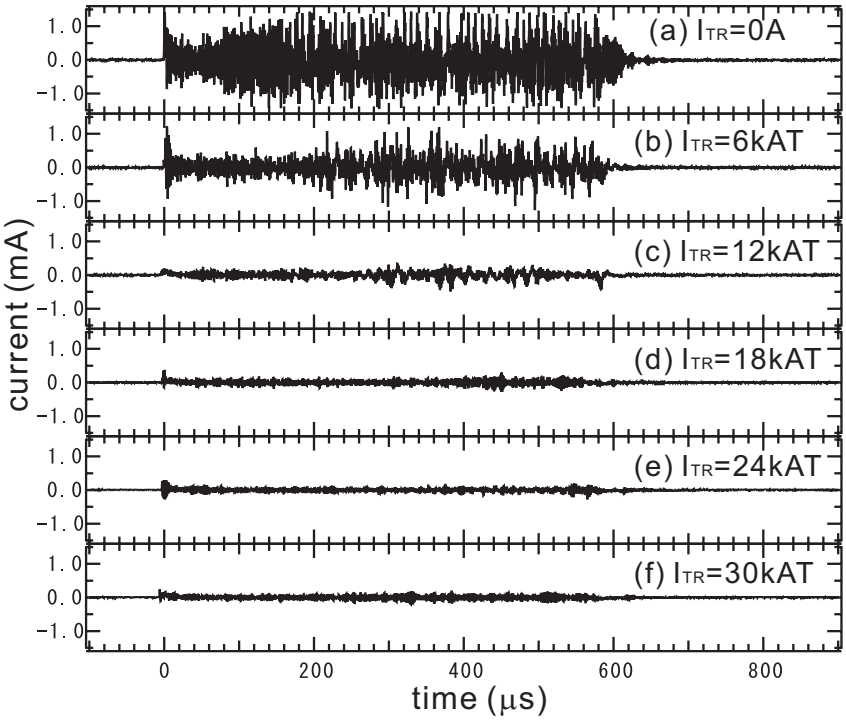

Figure 3.23: Suppression of electrostatic fluctuation by magnetic shear.

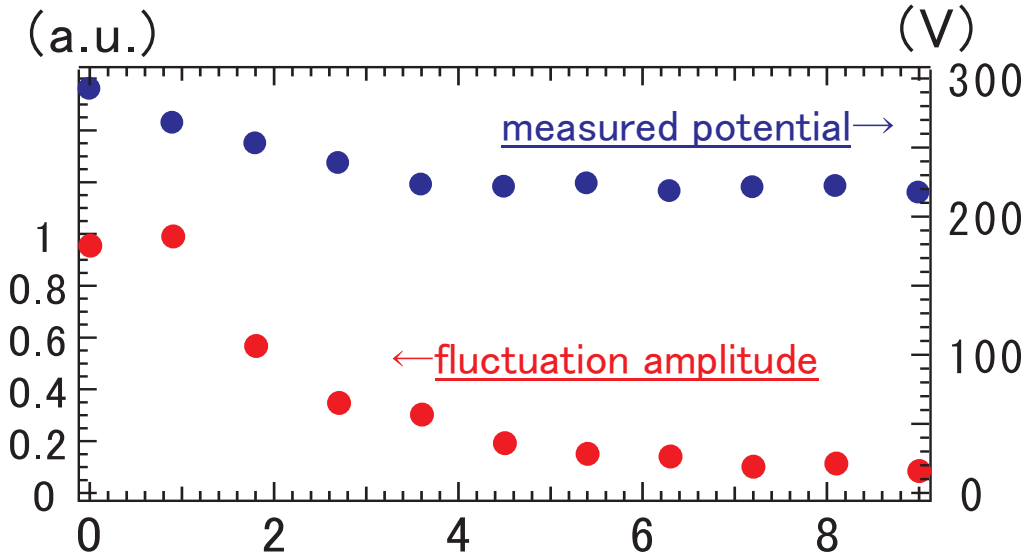

Figure 3.24: Amplitude of the fluctuation and space potential at $R = 46$ cm, as functions of added magnetic shear.

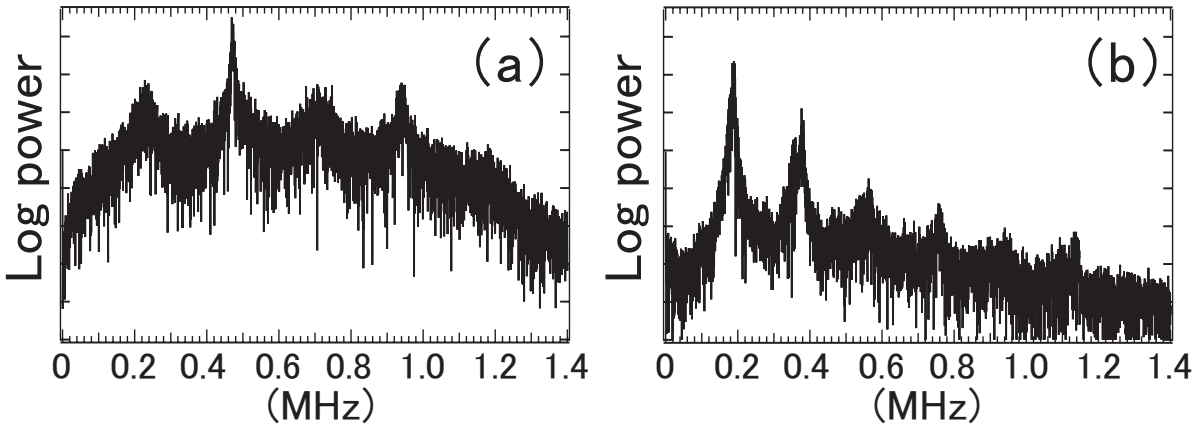

Figure 3.25: Power spectrum of wall signals when (a) I_{IC} = 7 kAT and I_{TR} = 0 and (b) I_{IC} = 7 kAT and I_{TR} = 30 kAT.

n = 1 mode. The observed phase shift of two wall probes shows similar dependence on toroidal field strength with the calculated ϕ, the phase difference of diocotron mode in the poloidal and toroidal magnetic fields. The disagreement in stronger toroidal field region is possibly because λ was simply assumed to be constant in the calculation of ϕ, and the effects of the increase of λ due to the spiral orbit is neglected.

3.4.2 Stabilizing effects of magnetic shear

Electrostatic fluctuations during the electron injection, measured by a wall probe, are shown in FIg. 3.23 in the variation of added toroidal field. Dipole field coil current I_{IC} = 7 kAT was kept constant. As described in Fig. 3.24, when I_{TR} is larger than $\sim$ 7 kAT, the amplitude of the total fluctuation decreases by a factor of 10, compared with when in pure dipole field configuration. During these experiments, the generated space potential is kept approximately constant (ϕ_H of emissive Langmuir probe at R = 46 cm is between 230 V and 290 V, for the variation of I_{IC} from 0 kAT to 9 kAT), and stabilization of diocotron instability by magnetic shear [85] is experimentally demonstrated.

The power spectrum of the fluctuation during the electron injection is shown in Fig. 3.25. As described in Fig. 3.26, when toroidal field is added to dipole magnetic field, the power of the fundamental mode decreases and second harmonic component becomes dominant. Although the measurement was done only in one poloidal cross section of the device and the mode patterns of the oscillation are not specified, the observation may suggest that n = 2 mode is dominant in pure dipole field and it is damped under the sheared magnetic field.

Although the addition of toroidal magnetic field is effective for the realization of quiet plasma during the electron injection, it induces the earlier onset of the rapid growth of instability after the

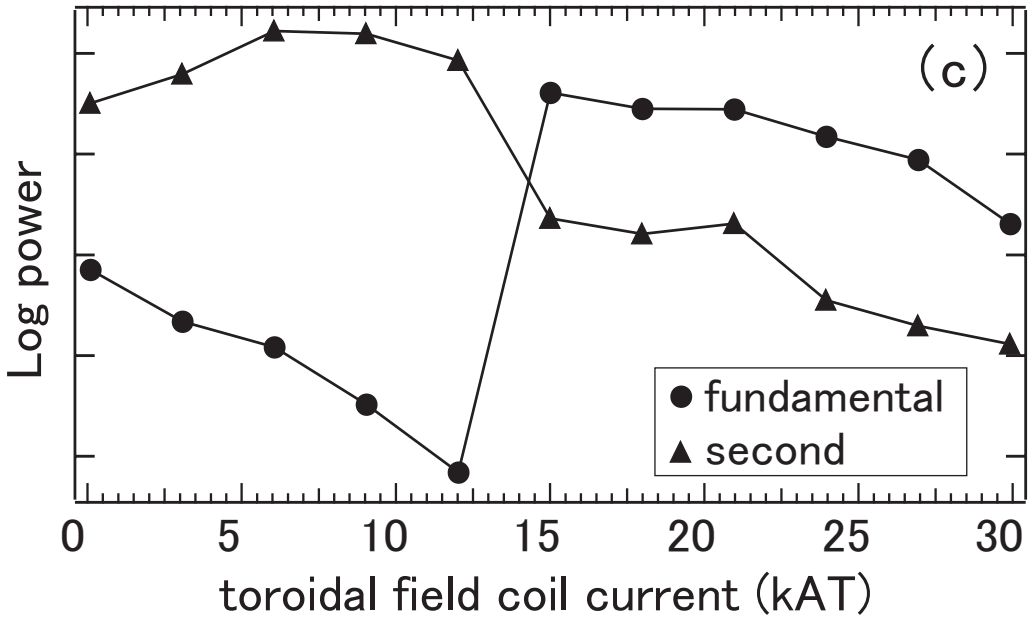

Figure 3.26: Intensity ratio of the fundamental and second harmonics mode in the variation of I_{TR}. I_{IC} = 7 kAT.

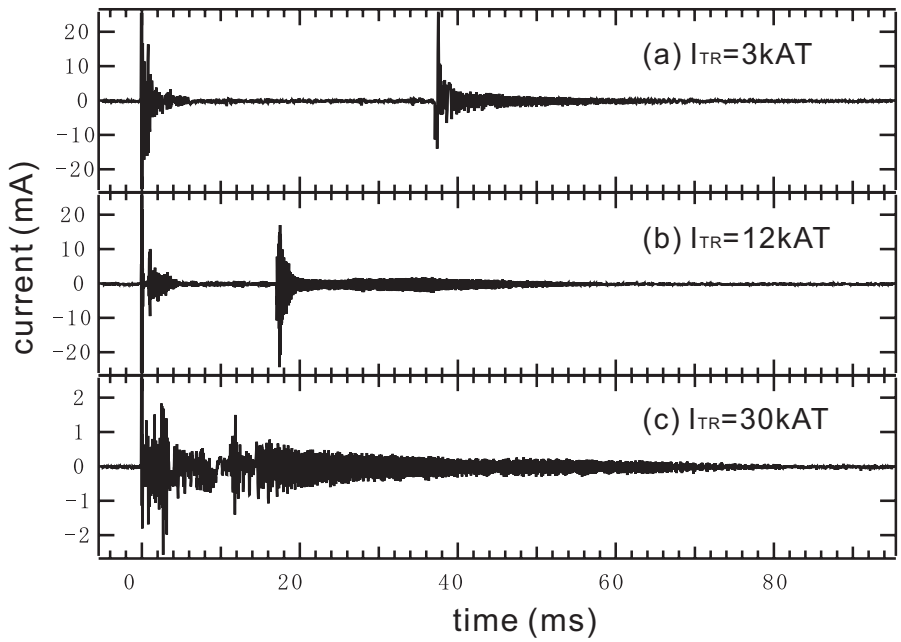

Figure 3.27: Stable confinement time *vs* added toroidal magnetic field while the dipole field coil current is constant: I_{IC} = 10.5 kAT.

stop of the electron injection. Figure 3.27 shows the wall probe signals in the variation of added toroidal field. The stable charge decay, as observed in pure dipole field configuration (Fig. 3.15), is not realized when the magnetic shear exists. As shown in the life time of the electron plasma as function of toroidal field strength in Fig. 3.28, the plasma tends to disrupt earlier in the stable confinement phase as the stronger toroidal field is added. Figure 3.29 shows the temporal decay of charge on a wall probe in the variation of added toroidal magnetic field, before the onset of the instability. In contrast to the life time t^* in Fig. 3.28, no significant difference was observed in the time constant τ of the charge decay.

Reduction of t^* is similarly observed even in the pure dipole field when structures like Langmuir probes are inserted into the confinement region, as shown in Fig. 3.13. One of the possible interpretations is that when electrons hit the surfaces of the obstacles, accumulated neutral gas molecules are released and ionized, and it causes the ion resonance instability [34, 93, 94]. When toroidal field is added to the pure dipole field configuration, the $\mathbf{E}\times\mathbf{B}$ drift motions of electrons take spiral orbits around the internal conductor, and the trajectories may intersect the coolant and feeder structures of the internal conductor. Then these effects could lead to the collisions of electrons with the obstacles. (The device configuration and electron orbits are shown in Figs. 2.3 and 2.13.) In contrast, when electrons are confined in pure poloidal field, the charged particles do not hit the coolant structures as long as they rotate in the toroidal direction due to the $\mathbf{E}\times\mathbf{B}$ drift motion. In fact, as described in Fig. 3.30, the addition of toroidal field lead to the increase of space potentials near the bar structure of the IC electrode, indicating that electrons are transported inwardly due to the spiral motion. These adverse effects of the coolant and power feeder structures could not be evaluated in the present device, and this problem might be solved in a stellarator [54] or superconducting levitated ring device [52] in future experiments.

3.5 Summary

We have confirmed long-term stable confinement under an appropriate control of the electric field. The obtained confinement time is sub-second order, and it is comparable to the classical diffusion time due to collisions with residual neutral gas in the present experiment.

In the Proto-RT device, toroidal pure electron plasma has been confined in the magnetic surface configuration for as long as classical diffusion time. When we adjust the equi-potential contours to the magnetic surfaces, the initial fluctuation damps and the trapped electron plasma enters a quiescent phase. In the present device parameters of $B \sim 10^{-2}$ T and $P = 4\times10^{-7}$ Torr, electrons with a peak density of an order of 10^{12} m^{-3} and total charge of $\sim 5\times10^{-8}$ C is confined for $\tau \sim 0.5$ s. When τ is below ~ 0.1 s, it is scaled as $\tau \propto P^{-1}B^3$ for the pressure range between 10^{-6} and 10^{-4} Torr, indicating that the collisions with remaining neutral gas limit the confinement of electrons. In the lower pressure region of below $\sim 10^{-6}$ Torr, τ saturates above ~ 0.1 s, suggesting

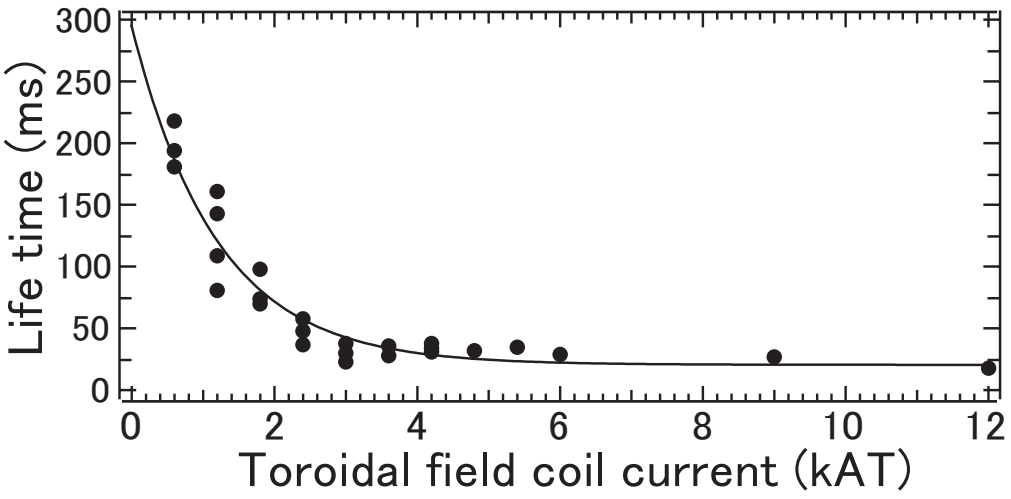

Figure 3.28: Life time of electron plasma in the variation of I_{TR}. Dipole field coil current I_{IC} = 7 kAT is kept constant.

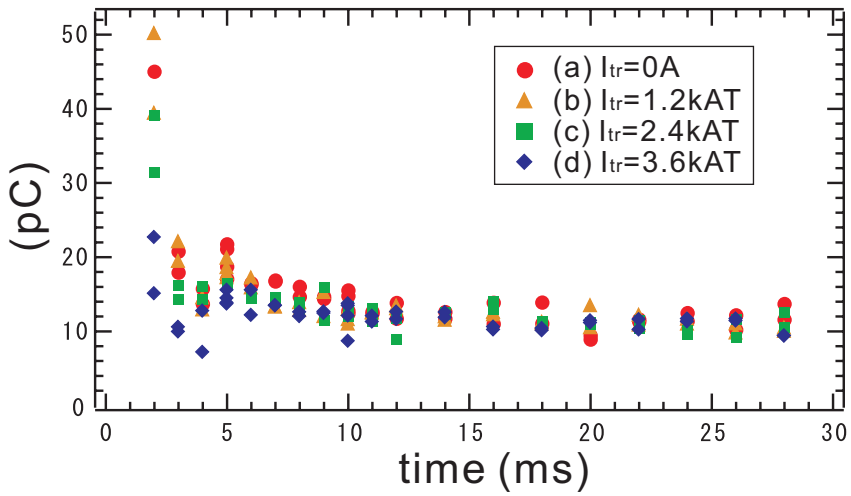

Figure 3.29: Decay of charge on a wall probe in the variation of added toroidal magnetic field. while dipole field coil current is constant: I_{IC} = 10.5 kAT.

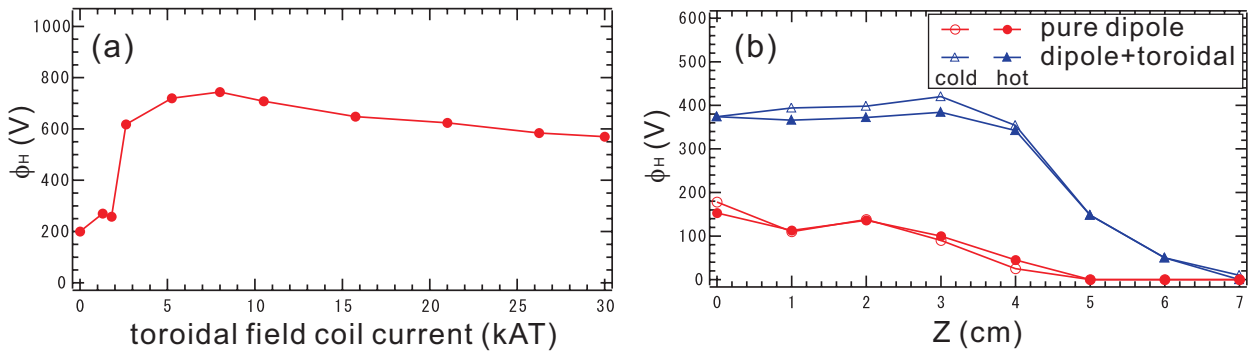

Figure 3.30: (a) Plasma potential at $R = 20$ cm and $Z = 0$ cm, in the variation of toroidal field strength as constant dipole field of $I_{IC} = 5.25$ kAT. (b) Potential profiles at $R = 20$ cm in pure dipole ($I_{IC} = 5.25$ kAT) and dipole plus toroidal field ($I_{IC} = 5.25$ kAT, $I_{IC} = 21$ kAT) configurations.

the anomalous loss of electrons. Although the stabilizing effects of magnetic shear is observed, the addition of toroidal field shortens the stable confinement time, possibly because of the obstacles of the support structure for the internal conductor.

Chapter 4

Flowing neutral plasma in a toroidal internal conductor trap

In the previous chapter, basic confinement properties of non-neutral plasma in the magnetic surface configuration were investigated using a pure electron plasma. In this chapter, neutral plasma is confined in the magnetic surface configuration and properties of radial electric field or toroidal flow were investigated. As described in the introductory paragraph, control of the internal flow is required for the various kinds of experiments in plasma physics, especially for the investigation of a new relaxation state of two-fluid plasmas (represented by double Beltrami fields). For such kind of studies, non-neutralization or formation of radial electric field of the plasma is one of the essential issues. Experimental results concerning bias experiments on hydrogen plasma will be described in the following sections.

4.1 Flow and radial electric field of plasmas in an internal conductor system

4.1.1 Parameters of 13.56 MHz RF plasma in Proto-RT

Experiments were carried out on Proto-RT with 13.56 MHz radio-frequency (RF) plasmas. As explained in chapter 2, the RF power is supplied to the plasma using capacitively or inductively coupled antennas located inside the chamber. Hydrogen pressure was 5×10^{-4} Torr. For the generation of radial electric field, the torus-shaped IC electrode and electron injection method was used for plasma bias.

The potential profiles of the plasma were measured by emissive Langmuir probes, by terminating the circuits with high impedance (100 MΩ) voltage probes. The probe characteristics (I-V curves) showed that the obtained potentials almost agree (usually underestimating some volts, due

		C-antenna	L-antenna
magnetic field strength	B	0.01 T	←
neutral gas density	n_n	2×10^{19} m^{-3}	←
plasma electron density	n_e	1×10^{15} m^{-3}	5×10^{13} m^{-3}
electron temperature	T_e	5 eV	←
ion temperature (estimated)	T_i	0.5 eV	←
electron Larmor radius	r_{Le}	0.7 mm	←
ion Larmor radius	r_{Le}	10 mm	←
Debye length	λ_D	0.5 mm	2 mm
ion sound speed	c_s	2×10^{4} ms^{-1}	←
Alfvén velocity	v_A	7×10^{6} ms^{-1}	3×10^{7} ms^{-1}
electron cyclotron angular frequency	ω_{ce}	2×10^{9} rads^{-1}	←
ion cyclotron angular frequency	ω_{ci}	1×10^{6} rads^{-1}	←
electron-neutral collision frequency	ν_{en}	3×10^{6} s^{-1}	←
ion-neutral collision frequency	ν_{in}	6×10^{4} s^{-1}	←
electron-ion collision frequency	ν_{ei}	5×10^{2} s^{-1}	←

Table 4.1: Typical experimental conditions, measured parameters, and calculated plasma parameters in 13.56 MHz RF experiments in Proto-RT.

to the space charge effects) with the space potential of the plasma, as discussed in chapter 2. The typical space potential during the electrode bias experiment is some 100 volts, and thus the measuring error of some volts can be sufficiently neglected. Because the electron temperature was low ($T_e \sim 5$ eV, measured by a double probe) and the variation of T_e was small throughout the experiments, the gradient of the measured "floating" potential gives a good approximation of the electric field. Together with emissive Langmuir probes and double probes, plane single probes (the tip is 3×3 mm molybdenum plate) were also used to measure electron density and temperature.

In the 13.56 MHz RF experiments, the typical electron number density measured by the Langmuir probe is $n_e = 1\times10^{15}$ m^{-3} and the typical electron temperature is $T_e = 5$ eV. With an applied magnetic field strength of $B \sim 0.01$ T, neutral gas density of $n_n = 2\times10^{19}$ m^{-3} ($P = 4\times10^{-4}$ Torr), and estimated hydrogen ion temperature of $T_i = 0.5$ eV, the calculated plasma parameters are summarized in Table 4.1. In the present parameter region, charged particles in the plasma is magnetized ($\omega_{ce} >> \nu_{kn}$, where k indicates ion or electron) and the neutral collisions exceeds the ion-electron collisions ($\nu_{ei} << \nu_{kn}$).

4.1.2 Force balance of charged particles

In the above parameter region, electromagnetic forces and neutral collisional effects are dominant in determining the motion of charged particles [76]. Because the experiments were carried out in

a pure poloidal magnetic field configuration, a radial electric field yields toroidal rotation of the plasma.

Neglecting the inertia term, the equation of motion for ions and electron in the steady state is

$$qn_{\rm k}(\mathbf{E}+\mathbf{v}_{\rm k}\times\mathbf{B})-\nabla\cdot\mathbf{P}\pm m_{\rm e}n_{\rm e}\nu_{\rm ei}(\mathbf{v}_{\rm e}-\mathbf{v}_{\rm i})-m_{\rm k}n_{\rm k}\nu_{\rm nk}\mathbf{v}_{\rm k}=0. \tag{4.1}$$

When neutral collisions are dominant compared with coulomb collision ($\nu_{ei} << \nu_{nk}$), and electron temperature is as low as $T_e \sim 5$ eV through out the confinement region, the motion of charged particles are decided by Lorentz force, pressure term, and neutral collision term:

$$qn_{\rm k}(\mathbf{E}+\mathbf{v}_{\rm k}\times\mathbf{B})-k_{\rm B}T_{\rm k}\nabla n_{\rm k}-m_{\rm k}n_{\rm k}\nu_{\rm nk}\mathbf{v}_{\rm k}=0. \tag{4.2}$$

When the perpendicular motion (magnetic field is assumed to be $\mathbf{B}=B\hat{\mathbf{z}}$)

$$qn_{\rm k}E_{\rm x}+qn_{\rm k}v_{\rm ky}B-k_{\rm B}T_{\rm k}\frac{\partial n}{\partial x}-m_{\rm k}n_{\rm k}\nu_{\rm nk}v_{\rm kx}=0 \tag{4.3}$$

$$qn_{\rm k}E_{\rm y}-qn_{\rm k}v_{\rm kx}B-k_{\rm B}T_{\rm k}\frac{\partial n}{\partial y}-m_{\rm k}n_{\rm k}\nu_{\rm nk}v_{\rm ky}=0 \tag{4.4}$$

is solved by the velocity, then

$$v_{\rm kx}\left(1+\frac{\omega_{\rm ck}^2}{\nu_{\rm nk}^2}\right)=\frac{q}{m_{\rm k}\nu_{\rm nk}}E_{\rm x}-\frac{k_{\rm B}T_{\rm k}}{m_{\rm k}n_{\rm k}\nu_{\rm nk}}\frac{\partial n}{\partial x}+\frac{\omega_{\rm ck}^2}{\nu_{\rm nk}^2}\left(\frac{E_{\rm y}}{B}-\frac{k_{\rm B}T_{\rm k}}{qB}\frac{1}{n_{\rm k}}\frac{\partial n}{\partial y}\right) \tag{4.5}$$

$$v_{\rm ky}\left(1+\frac{\omega_{\rm ck}^2}{\nu_{\rm nk}^2}\right)=\frac{q}{m_{\rm k}\nu_{\rm nk}}E_{y}-\frac{k_{\rm B}T_{\rm k}}{m_{\rm k}n_{\rm k}\nu_{\rm nk}}\frac{\partial n}{\partial y}+\frac{\omega_{\rm ck}^2}{\nu_{\rm nk}^2}\left(\frac{E_{\rm x}}{B}+\frac{k_{\rm B}T_{\rm k}}{qB}\frac{1}{n_{\rm k}}\frac{\partial n}{\partial x}\right) \tag{4.6}$$

and the perpendicular velocity is given by

$$\mathbf{v}_{\mathbf{k}\perp}=\frac{1}{1+\omega_{\rm ck}^2/\nu_{\rm nk}^2}\left(\frac{q}{m_{\rm k}\nu_{\rm nk}}\mathbf{E}-\frac{k_{\rm B}T_{\rm k}}{m_{\rm k}\nu_{\rm nk}}\frac{\nabla n_{\rm k}}{n_{\rm k}}\right)+\frac{1}{\nu_{\rm nk}^2/\omega_{\rm ck}^2+1}\left(\frac{\mathbf{E}\times\mathbf{B}}{B^2}-\frac{\nabla p_{\rm k}\times\mathbf{B}}{qnB^2}\right). \tag{4.7}$$

When the pressure term is neglected by assuming that the density gradient is relatively small inside the confinement region, $\mathbf{v}_{\mathbf{k}\perp}$ is simplified as

$$\mathbf{v}_{\rm k\perp}=\frac{q\nu_{\rm nk}}{m_{\rm k}\omega_{\rm ck}^2}\mathbf{E}+\frac{\mathbf{E}\times\mathbf{B}}{B^2}, \tag{4.8}$$

here $\omega_{\rm ck}^2/\nu_{\rm nk}^2 \sim 10^5$ (ion), 10^7 (electron) $>> 1$ and therefore small terms in the denominators are also neglected. The first term represents the radial transport of charged particles due to the collisions with neutral molecules in the radial electric field. The second term is the $\mathbf{E}\times\mathbf{B}$ drift motion in the toroidal direction. The relation between radial electric field $E_\perp$ and radial current density $j_\perp$ is given by

$$j_\perp=|q|(n_{\rm i}v_{\rm i}+n_{\rm e}v_{\rm e})=q^2n_{\rm e}\left(\frac{\nu_{\rm ni}}{m_{\rm i}\omega_{\rm ci}^2}+\frac{\nu_{\rm ne}}{m_{\rm e}\omega_{\rm ce}^2}\right)E_\perp. \tag{4.9}$$

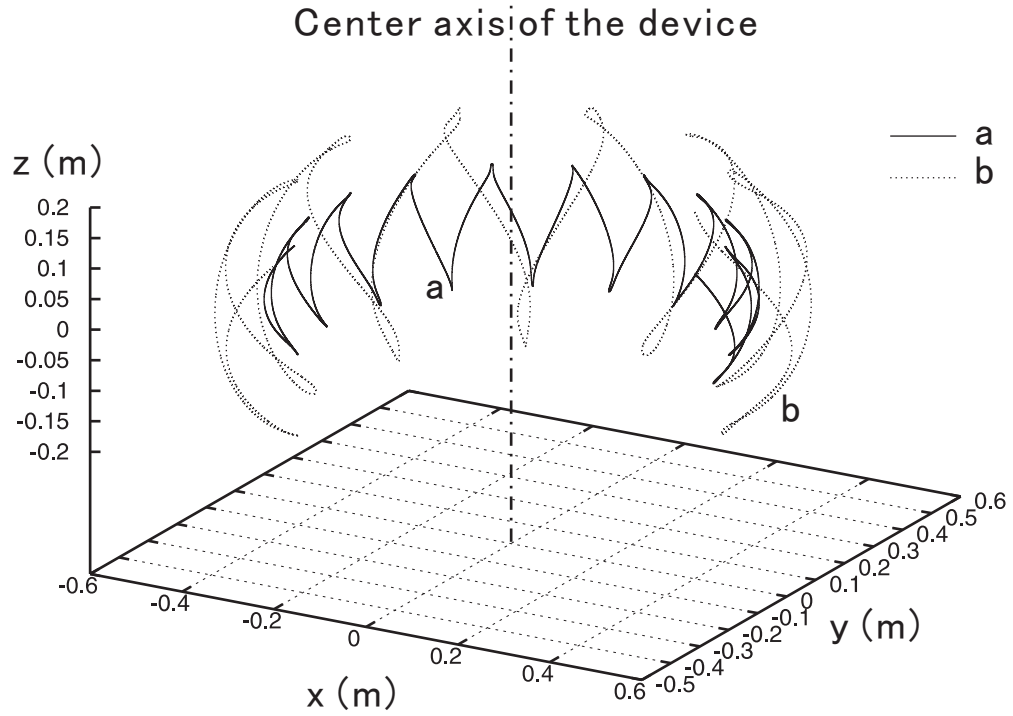

Figure 4.1: Hydrogen ion orbits in the radial electric field and poloidal magnetic field of the Proto-RT. The initial position of the ion is (a) $r = 0.4$ m $z = 0.1$ m and (a) $r = 0.4$ m $z = 0.2$ m, respectively. Charged particles undergo toroidal $\mathbf{E} \times \mathbf{B}$ motion and reflection motion due to magnetic mirror effects.

Under the present experimental conditions, the ion term is dominant, and thus the radial current is transported primarily by ions:

$$j_{\mathrm{r}} \simeq \frac{q^2 n_{\mathrm{e}} \nu_{\mathrm{in}}}{m_{\mathrm{i}} \omega_{\mathrm{ci}}^2} E_{\mathrm{r}} = 1 \times 10^{-3} E_{\mathrm{r}}. \tag{4.10}$$

These relations indicate that when radial electric field is sustained by radial plasma current, $\mathbf{E} \times \mathbf{B}$ drift flow is induced in the plasma in the toroidal direction.

4.1.3 Ion orbit

In the poloidal magnetic field configuration of the internal conductor system, charged particles undergo four kinds of motions: Larmor gyration around magnetic field lines, toroidal rotation due to $\mathbf{E} \times \mathbf{B}$ drift, radial transport due to collisions with neutrals, and bounce motion due to magnetic mirror caused by the inhomogeneous field strength. Including the finite inertia term and realistic magnetic field, the individual motions of ions can be calculated numerically. Figure 4.1 shows the single ion orbit under the influence of DC electric and magnetic fields in the geometry of Proto-RT.

Electrode	material	stainless steel (SUS304)
	power source	DC 2 kV 1 A
	installation	on the internal conductor
	bias against	vessel wall
	advantages	large radial current
Electron injection gun	cathode	LaB_6
	power source	DC 2 kV 1 A
	installation	gun port at $Z = 0$, movable in radial direction
	bias against	anode *or* vessel wall
	advantages	low contamination
Orbit loss	loss mechanism	high energy electrons produced by ECH
(not used in Proto-RT)	advantages	low contamination, self-bias

Table 4.2: Plasma bias methods for the creation of radial electric field.

The ions undergo an $\mathbf{E}\times\mathbf{B}$ drift motion in the toroidal direction, and also the orbit takes a banana-like trajectory due to the magnetic mirror reflection. In the experimentally obtained electric field of $E \sim 10^3$ Vm^{-1} and with a typical magnetic field strength of $B \sim 0.01$ T, the toroidal rotational speed of charged particles by the $\mathbf{E}\times\mathbf{B}$ drift motion is $\sim 1\times10^5$ ms^{-1}. The mean free path of the ion between the collisions with neutral atoms is ~ 1 m, which is comparable to or larger than the machine scale length, and thus the individual motion induces an effective toroidal flow in the plasma.

4.1.4 Plasma bias experiments

As discussed in the previous subsections, in the present geometry and parameter region, the existence of radial electric field across the magnetic surfaces is equivalent to the formation of toroidal $\mathbf{E}\times\mathbf{B}$ flow in a plasma. As for the generation of radial electric field inside the plasma, several techniques could be considered, such as the external electrode bias, electron injection, or loss of fast electrons [52]. In this study, the effects of electrode bias and electron injection into a hydrogen plasma was tested in the Proto-RT device, as summarized in Table 4.2. Experiments were carried out in both capacitively coupled (C-type) and inductively coupled (L-type) operations of 13.56 MHz RF discharges, and experimental results therein are explained in the following sections.

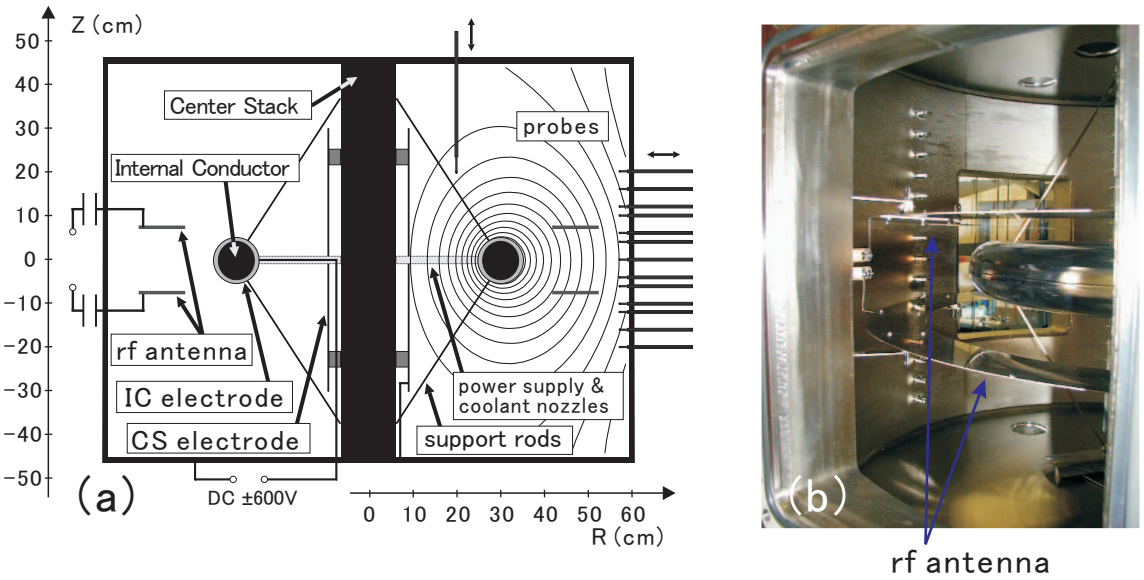

Figure 4.2: (a) Poloidal cross-section of the Proto-RT chamber and magnetic surfaces of the poloidal field configuration. (b) Internal view of the Proto-RT chamber including the C-type RF antenna, taken from a maintenance port.

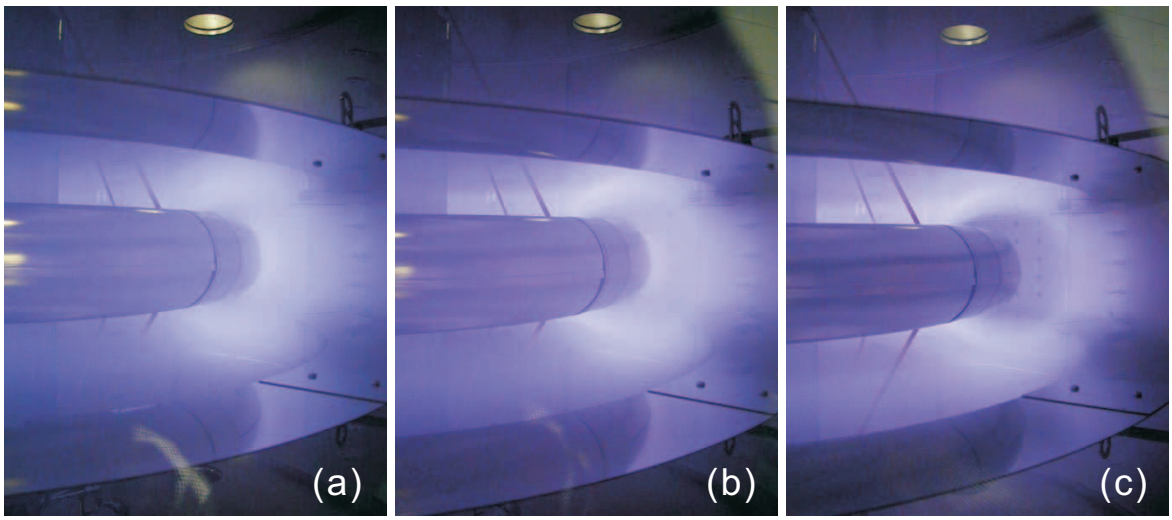

Figure 4.3: Photograph of hydrogen plasma with several kinds of electrode bias. (a) V_{IC} = 0 V, not biased, (b) V_{IC} = −300 V, negatively biased, and (c) V_{IC} = +300V V, positively biased.

4.2 Electrode bias experiment in Proto-RT

4.2.1 Electrode bias in C-type antenna discharge

Potential profiles and electrode current

Diagram and photographic view of the Proto-RT device including the C-type antenna are shown in Fig. 4.2. For the formation of the radial electric field, a DC bias voltage V_{IC} was applied on the IC electrode against the vessel wall. Plasmas are generated by RF power of 100 W in the center null configuration (dipole field coil current I_{IC} = 7 kAT and vertical field coil current I_{VF} = 2.3 kAT) The hydrogen gas pressure is 4×10^{-4} Torr. Distributions of light emission from the plasma are shown in Fig. 4.3 in the variation of applied bias voltage on the IC electrode. In contrast to the distribution when $V_{IC} = 0$ in Fig. 4.3 (b), negative bias induces a bright region near the electrode as shown in Fig. 4.4(a). When the IC electrode is positively biased in Fig. 4.4 (c), dark layer is observed around the electrode. Figure 4.4 shows a current I_{IC} between the IC electrode and the chamber as a function of V_{IC}. The applied magnetic field suppressed the radial current carried by the collisional transport of ions, and a bias voltage up to ±600 V was successfully applied on the IC electrode. As shown in Fig. 4.5, the density distribution of the plasma was modified by the applied bias voltage on the electrode. The displacement of the density profile (~ 2 cm) is much larger than the Debye length ($\lambda_D \sim 0.5$ mm). When the IC electrode, which is located in the confinement region of plasmas, is positively biased, a region of very low density (less than 1% of when $V_{IC} = 0$) is formed around the IC electrode. Figure 4.6 shows the radial profiles of ion saturation current I_{is} in the variation of V_{IC}. Corresponding to the displacement of the stronger light emission region, shown in Fig. 4.3, causes the shift of hydrogen plasma toward the low-space potential region.

The radial potential profiles of plasmas in the variation of V_{IC}, and the two-dimensional potential profiles when $V_{IC} = \pm 600$ V are shown in Figs. 4.7 and 4.8. Potential contours coincide almost exactly with the flux surfaces of poloidal magnetic fields excepting the neighborhood of the rf antennas, and the electric fields are mainly generated in the radial direction. In the potential distribution of the condition $V_{IC} > 0$, a voltage drop was observed in a very limited region near the electrode, which corresponds to the low density region in Fig. 4.5. In contrast, when $V_{IC} < 0$, a smooth potential gradient was generated in the wide range of the confinement region of the plasma between the IC electrode and the vessel wall because the low density region was not formed in these cases.

The profiles of radial electric field strength and the corresponding $\mathbf{E} \times \mathbf{B}$ drift speed obtained from the potential profiles in Fig. 4.7 are shown in Fig. 4.9. Because the rf coupling and density distribution of the plasmas were modified according to the magnetic field strength or background neutral density, it was not a straightforward operation to obtain the parameter dependence of the radial electric field E_r and the radial current I_{IC} between the IC electrode and the vessel wall.

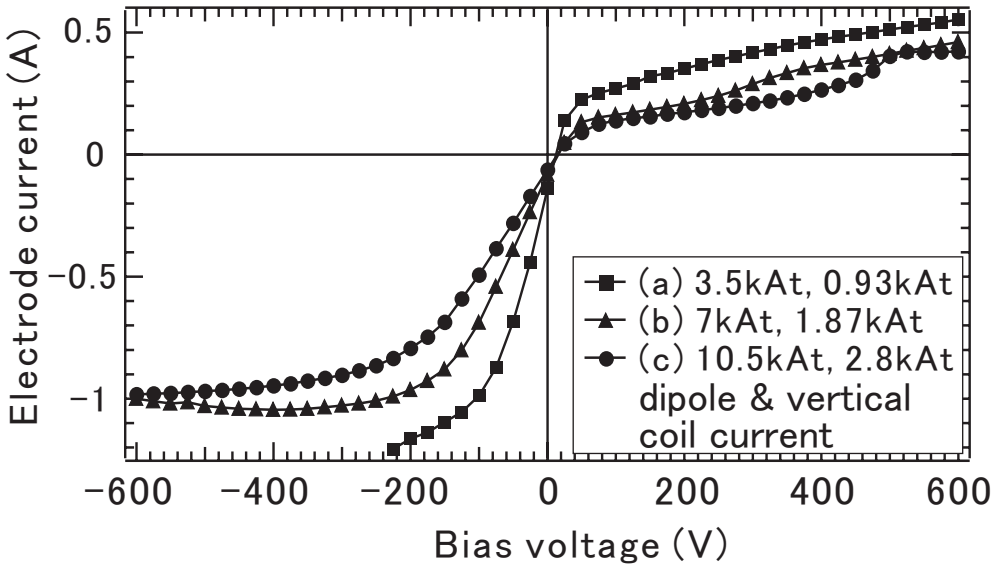

Figure 4.4: Applied voltage on the IC electrode *vs* current between the electrode and chamber wall.

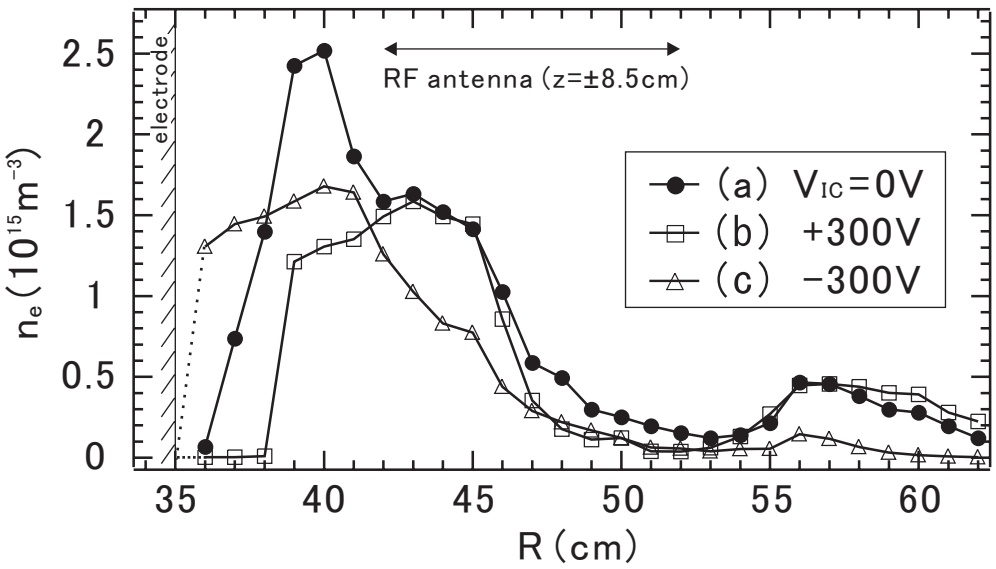

Figure 4.5: Radial profiles of electron number density at z=0, (a) when V_{IC} = 0, the electrode is grounded, (b) positively biased V_{IC} = +300 V, and (c) negatively biased V_{IC} = −300 V.

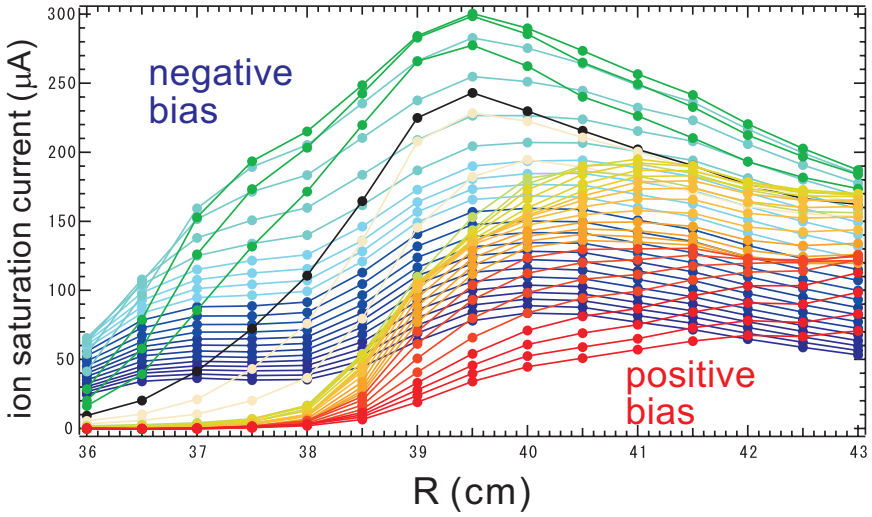

Figure 4.6: Radial profiles of the ion saturation current in the variation of the bias voltage of the IC electrode from $V_{\mathrm{IC}} = -600$ V to +600 V.

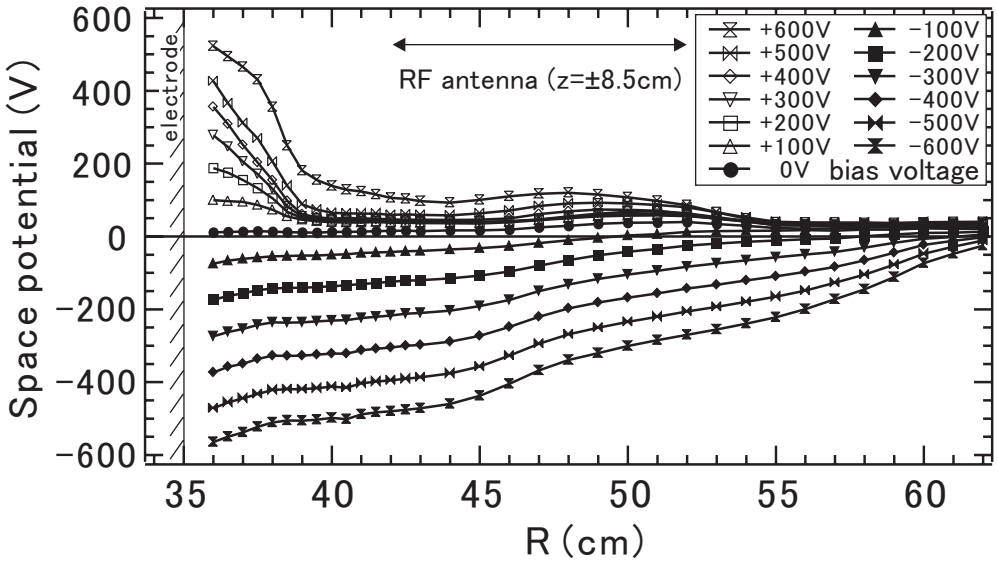

Figure 4.7: Radial potential profiles (floating potentials of emissive Langmuir probes) of plasmas at z=0, with an IC electrode bias voltage of V_{IC} from −600 to +600 V.

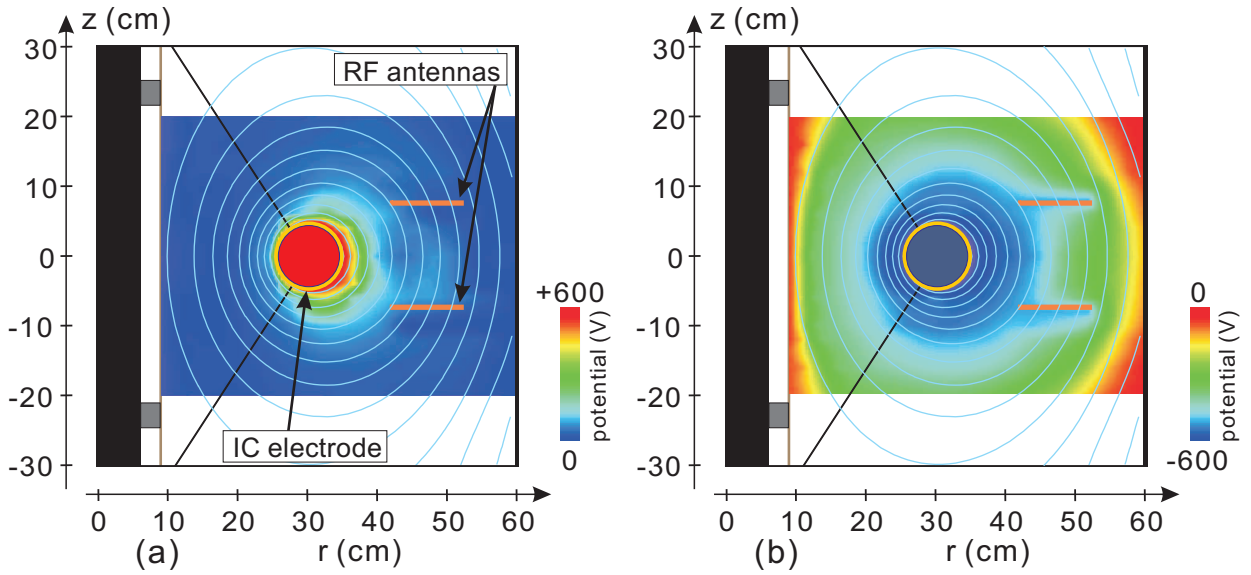

Figure 4.8: (color) Potential distribution of plasmas in the poloidal cross-section of the Proto-RT, (a) when the IC electrode was positively biased (V_{IC} = +600 V), and (b) negatively biased (V_{IC} = −600 V). Thin lines show the poloidal magnetic surfaces.

However, with the surface area of the IC electrode $S_{\mathrm{IC}} = 0.59$ m^2 and by assuming the radial symmetry of plasmas around the IC electrode, the observed $E_{\mathrm{r}} \sim 3$ kVm^{-1} near the IC electrode and $I_{\mathrm{IC}} \sim 1$ A generally agree with the relation between E_{r} and I_{IC} in (Eq. 4.11), suggesting that the observed radial electric field and electrode current are understood as the transport due to the neutral collisions of ions.

Plasma distribution in X-point configuration

By turning the direction of the vertical field coil current, X-point magnetic field configuration is produced, instead of the center null configurations used in the previous sections. These typical magnetic surfaces and profiles of the field strength are shown in Fig. 2.5. Plasma ions are repelled by positively biased electrodes, and especially when magnetic field lines touch the vessel wall in the X-point configurations (Fig. 2.5 (d)), electrode bias induces drastic displacement of the plasma. Figures 4.11 and 4.12 show the distributions of light emission when stronger vertical field is applied. When the R of the X-point is smaller than $\sim$ 55 cm, and thus the last closed magnetic surface does not intersect the RF antenna, plasmas are localized in the closed magnetic surfaces. Potential profiles inside the localized plasmas were not measured, because the insertion of Langmuir probes destroy the distribution of the plasmas.

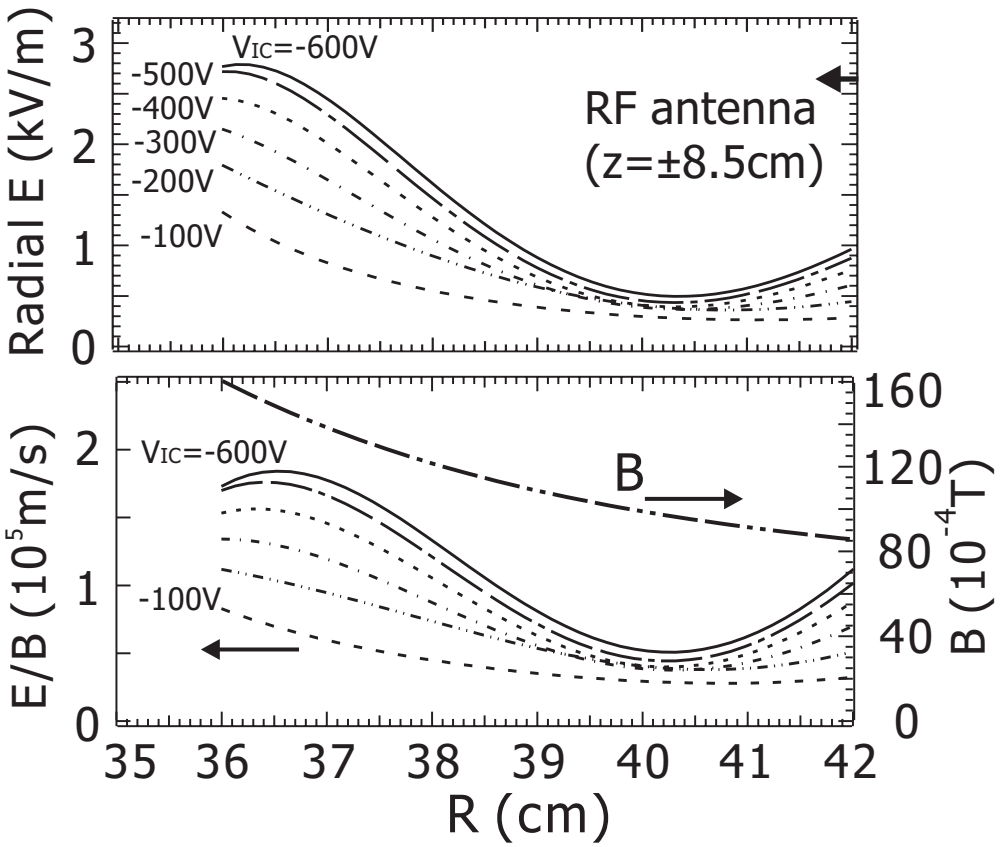

Figure 4.9: Profiles of (a) radial electric field strength and (b) poloidal magnetic field strength B and $\mathbf{E}\times\mathbf{B}$ drift speed at $z = 0$, when the electrode bias voltage was modified from $V_{IC} = -600$ V to -100 V, calculated from the potential distribution in Fig. 4.7.

Disturbance due to C-type antenna

As shown in Fig. 4.2, the C-type antenna is located in the confinement region of the device, and it induced serious disturbance to the potential structures of plasmas. The potential profile of hydrogen plasma, when the IC electrode is grounded, is shown in Fig. 4.13. Due to DC potentials on the antenna and acceleration of particles along magnetic field lines, there exists some asymmetric distorted profiles and it leads to error electric fields. As shown in the figure, the disturbance is of the order of some *tens* of volts. Experiments carried out with L-type antenna will be explained in the next section.

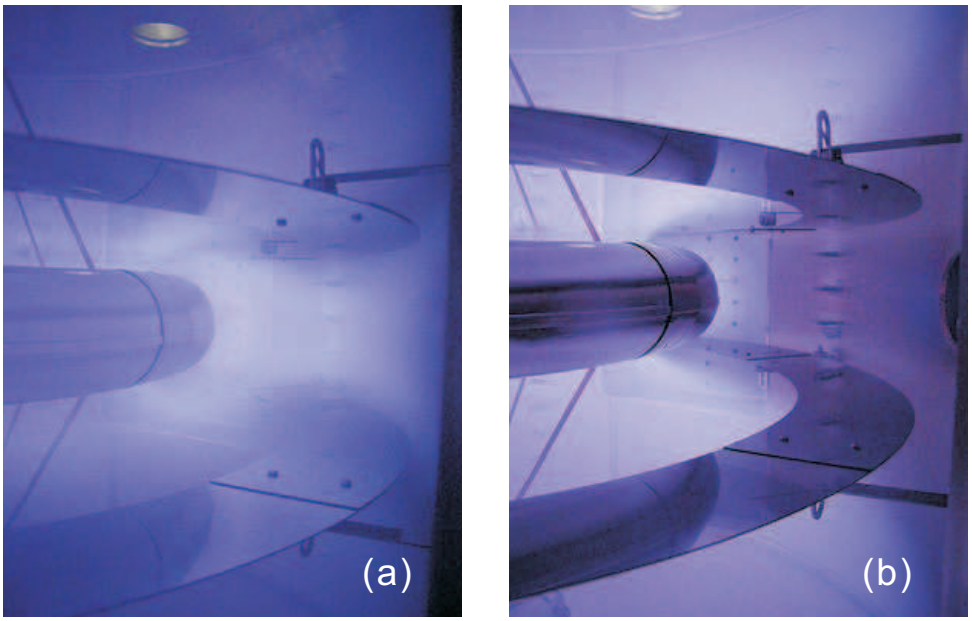

Figure 4.10: Photograph of hydrogen plasma with electrode bias in the X-point magnetic field configuration, when the electrode is (a) negatively biased (V_{IC} = −300 V) and (b) positively biased (V_{IC} = +300 V).

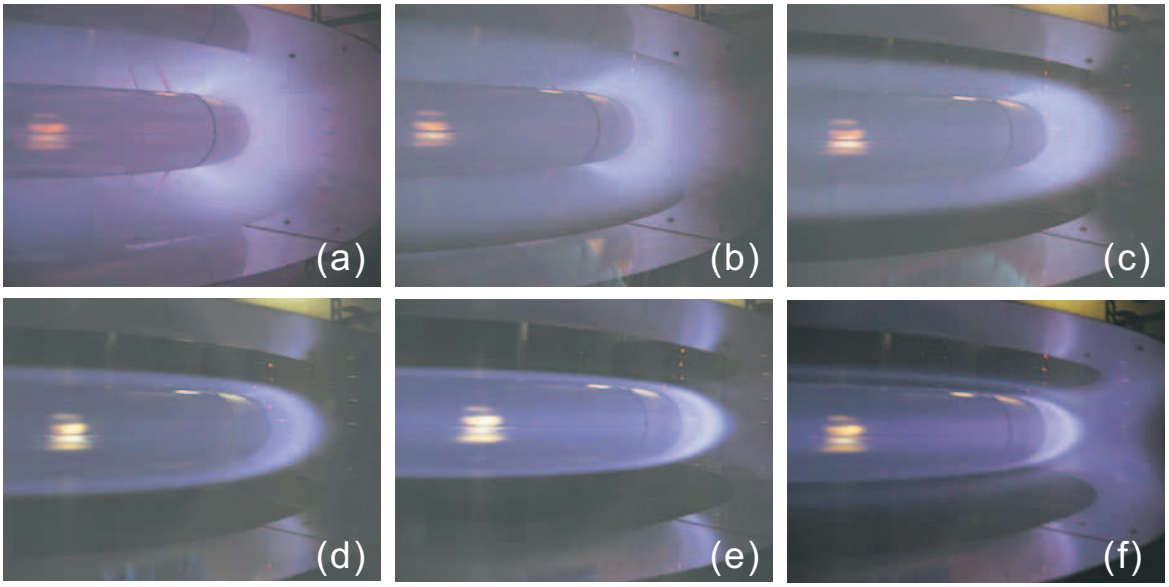

Figure 4.11: Photograph of localized plasma by electrode bias (V_{IC} = −300 V) in the X-point magnetic field configuration. Applied vertical field coil current I_{VF} and X-point positions are, (a) 0 kAT, - cm, (b) 5 kAT, 56.2 cm, (c) 10 kAT, 51.8 cm, (d) 15 kAT, 47.2 cm, (e) 20 kAT, 44.4 cm, (f) 23 kAT, 43.2 cm. Dipole field coil current of I_{IC} = 7 kAT is constant.

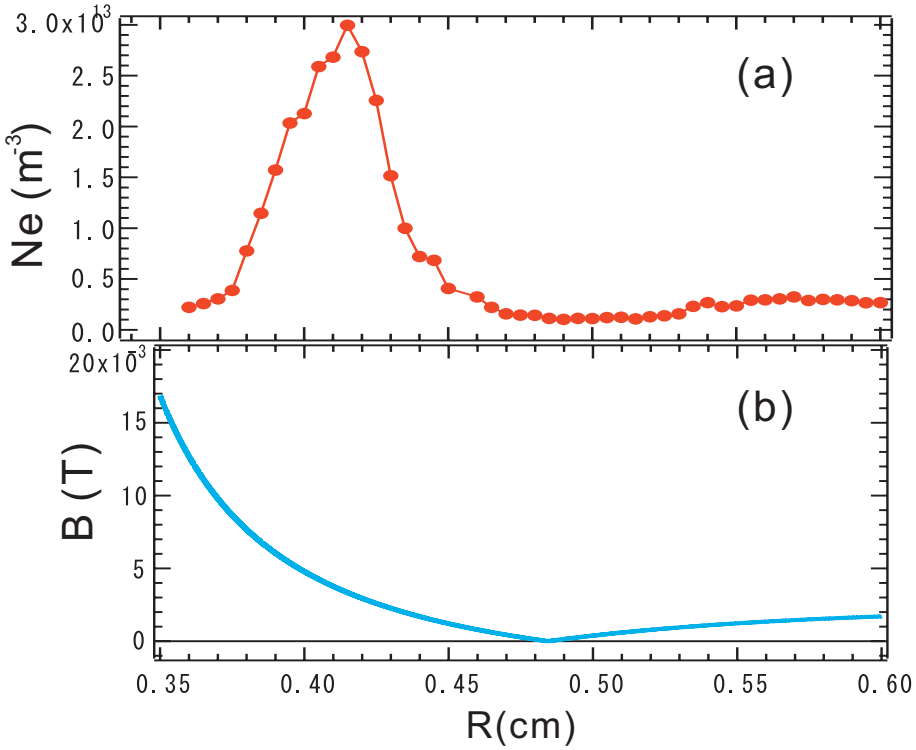

Figure 4.12: (a) Radial electron density at $Z = 0$ and (b) poloidal magnetic field strength in X-point magnetic field configuration.

4.2.2 Experiments in L-type antenna discharge

Potential profiles and radial current

13.56 MHz RF plasma is generated by a L-type antenna and bias experiment was carried out. Although the electron density of the L-coupled plasma is about an order of magnitude smaller than that of C-coupled plasma, the C-type antenna is located inside the confinement region and it leads to the distortion of the radial electric field. Experimental set up of Proto-RT with L-type antenna is shown in Fig. 4.14. In contrast to the C-type antenna (located at $R = 42$ to 52 cm), L-type antenna is located at $R = 53$ cm. It has a loop structure and the volume of the antenna is also smaller than C-type antenna, and thus disturbance to the plasma is supposed to be relatively small. The other experimental conditions: RF input power of ~ 200 W, the typical magnetic field strength of the order of 10^{-2} T, hydrogen pressure of 4×10^{-4} Torr are same as the previous experiment.

The potential profiles of plasmas were measured by emissive Langmuir probes. DC bias voltage V_{IC} was applied on the IC electrode against the vessel wall for the formation of the internal electric field and flow of plasmas. The potential structures of plasmas under the influence of a positively or negatively biased ring electrode are shown in Figs. 4.15 and 4.16. When compared with potential profiles with C-type antenna in Figs. 4.7 and 4.8, distortion of potential structures due to

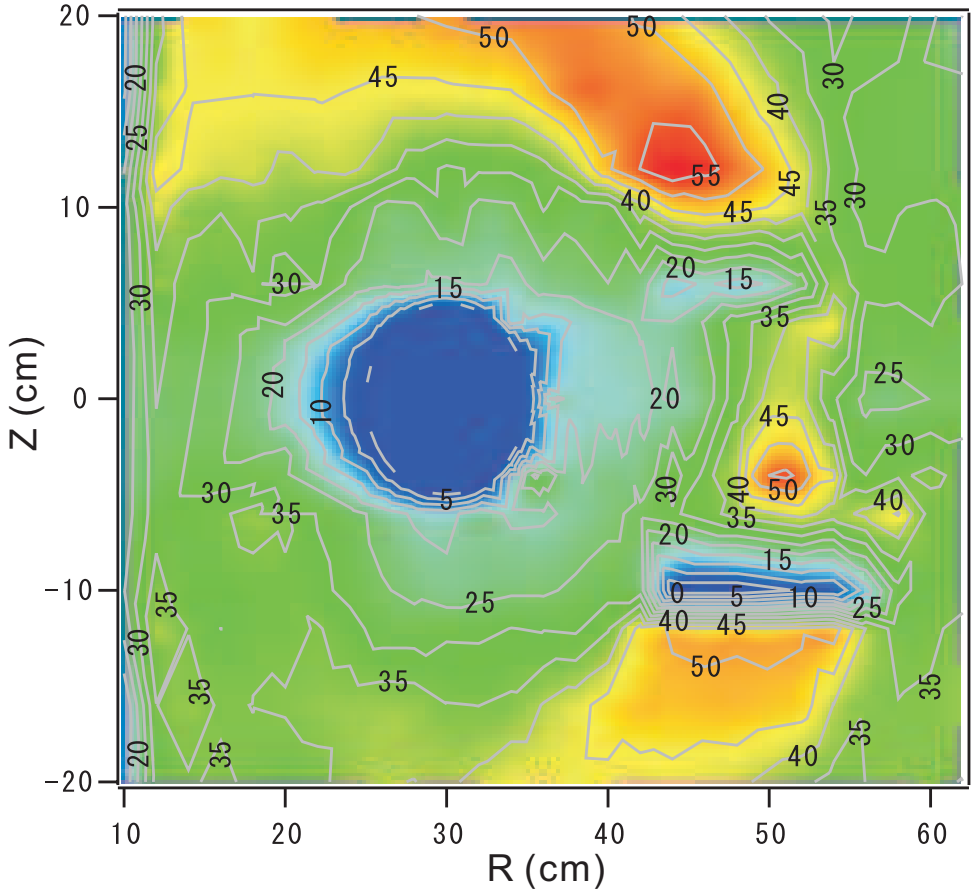

Figure 4.13: Two-dimensional potential profiles with C-antenna when $V_{IC} = 0$.

the RF antenna is drastically improved. Potential contours almost coincide with the flux surfaces of poloidal magnetic fields and the electric field is generated in the radial direction of the toroidal plasmas. When the electrode was negatively biased, internal electric field of up to 2 kVm^{-1} was produced in a broad region between the electrode and the vessel wall. The corresponding toroidal $\mathbf{E}\times\mathbf{B}$ rotational speed is $\sim 10^5$ ms^{-1}. In contrast, when $V_{IC} > 0$, potential gradient was observed in a very limited region near the electrode, and internal electric field was not generated. A current between the IC electrode and vessel wall, I_{IC}, in Fig. 4.17 also shows the strong asymmetry of the response of plasmas against the polarity of the electrode voltage. In the radial distributions of electron density in Fig. 4.19 (the corresponding potential profiles are shown in Fig. 4.18), a density gap is formed around the IC electrode when the IC electrode is positively biased. It leads to limit the current I_{IC} and also results in the observed flat potential profiles when $V_{IC} > 0$.

By substituting the obtained experimental parameters in the L-type antenna discharge into the relation between the radial current and electric field (Eq. (4.9)),

$$j_r \simeq \frac{q^2 \nu_{in} n_e}{m_i \omega_{ci}^2} E_r \sim 3\times 10^{-5} E_r, \tag{4.11}$$

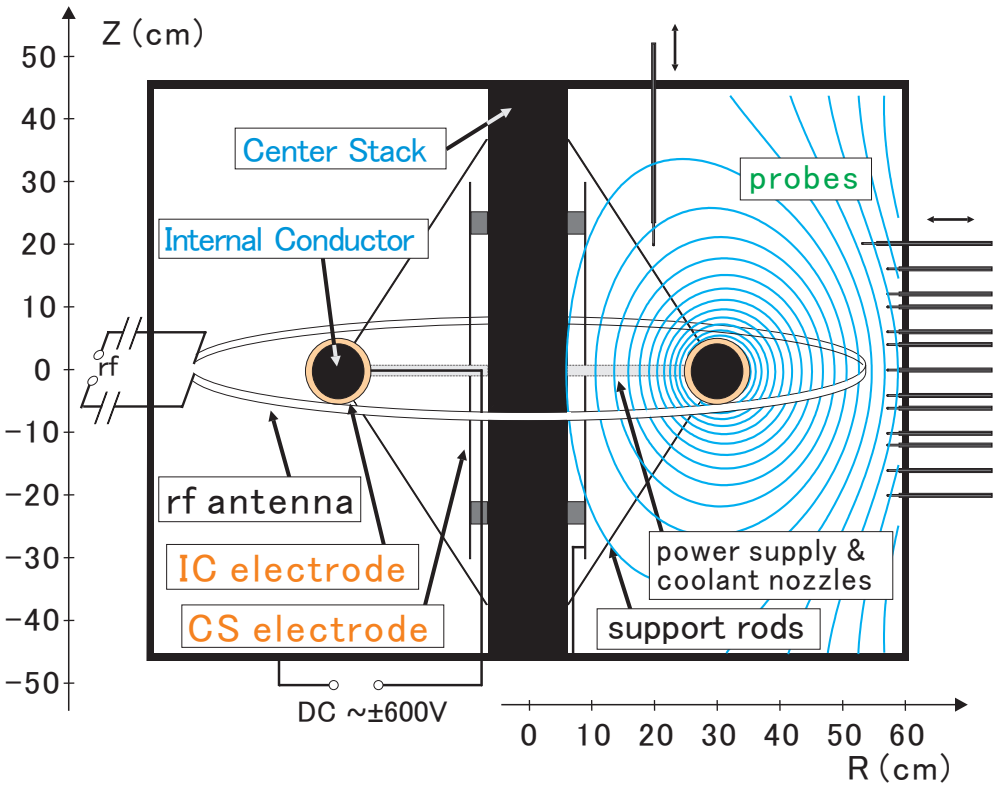

Figure 4.14: Schematic view of the Proto-RT and magnetic surfaces generated by an internal ring coil and external vertical field coils (not seen).

because the first term in Eq. (4.9) is dominant again, and the radial current across the magnetic surfaces is mainly transported by ions.

Because the RF coupling and density distribution of the plasmas are modified according to the magnetic field strength or background neutral density, it was not straightforward to obtain the parameter dependence of the radial electric field E_r and the radial current I_{IC} between the IC electrode and the vessel wall. However, with the surface area of the IC electrode $S_{IC} = 0.59$ m^2 and by assuming the radial symmetry of plasmas around the IC electrode, the observed $E_r \sim 5$ kVm^{-1} near the IC electrode and $I_{IC} \sim 0.3$ A generally agree with the relation between E_r and I_{IC} in Eq. 4.11, indicating the observed radial electric fields and the electrode current are explained as the transport due to the collisions with neutral atoms.

Potential profiles and magnetic surfaces

Figure 4.20 shows the radial potential profiles with negative bias on the IC electrode ($V_{IC} = -100$ to -600 V), in the variation of magnetic field configurations. The corresponding magnetic surfaces are shown in Fig. 2.5. The positions of the last closed surface are also shown in Fig. 4.20 as vertical solid lines. Although certain amount of radial electric field is effectively generated inside

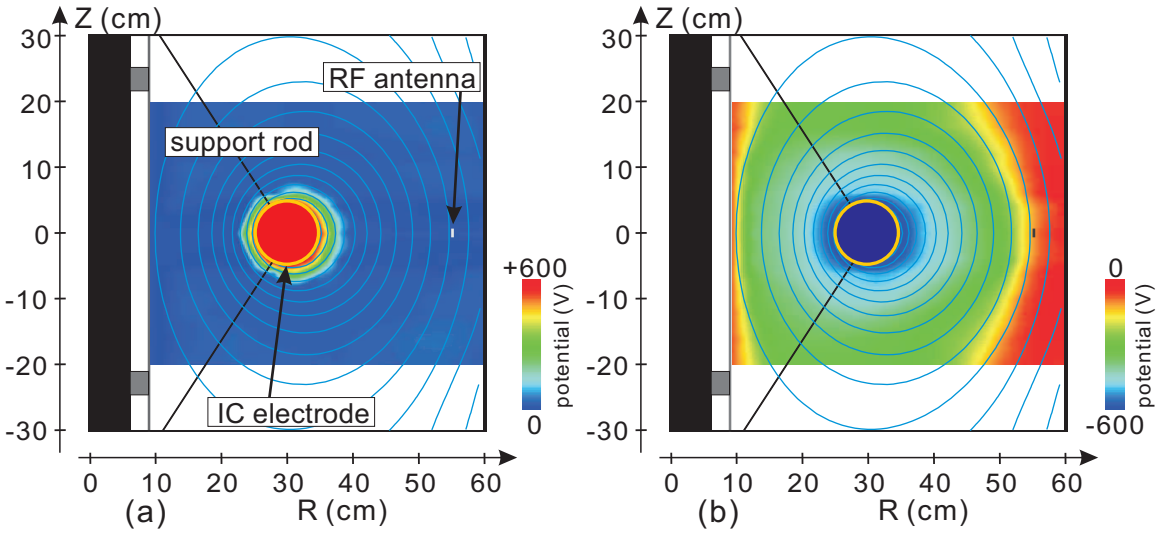

Figure 4.15: Two-dimensional potential profiles of plasmas (floating potentials of emissive Langmuir probes) when the IC electrode was (a) positively biased: V_{IC}=+600 V and (b) negatively biased: V_{IC}=-600 V. Thin lines show the magnetic surfaces.

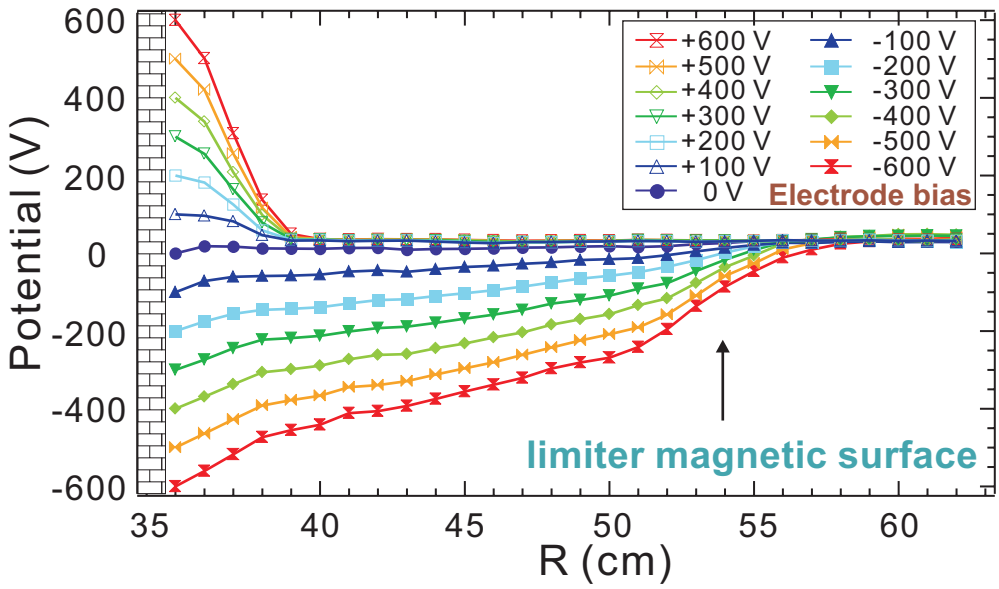

Figure 4.16: Radial potential profiles of plasmas at $Z = 0$, in the variation of IC electrode bias voltage V_{IC} from −600 to +600 V.

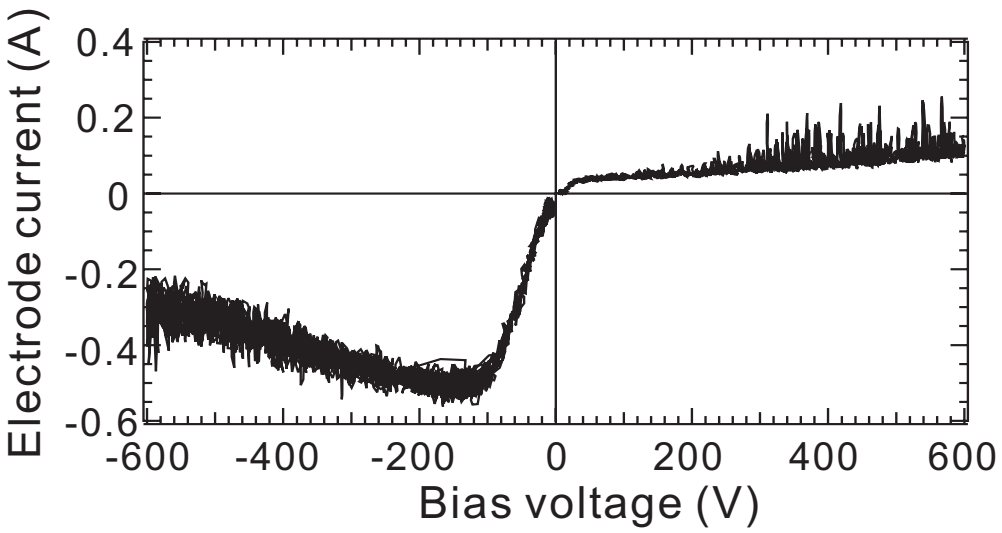

Figure 4.17: IC electrode current *vs* bias voltage. Decrease of the current when $V_{\mathrm{IC}} < -200V$ is due to the difficulty of RF matching.

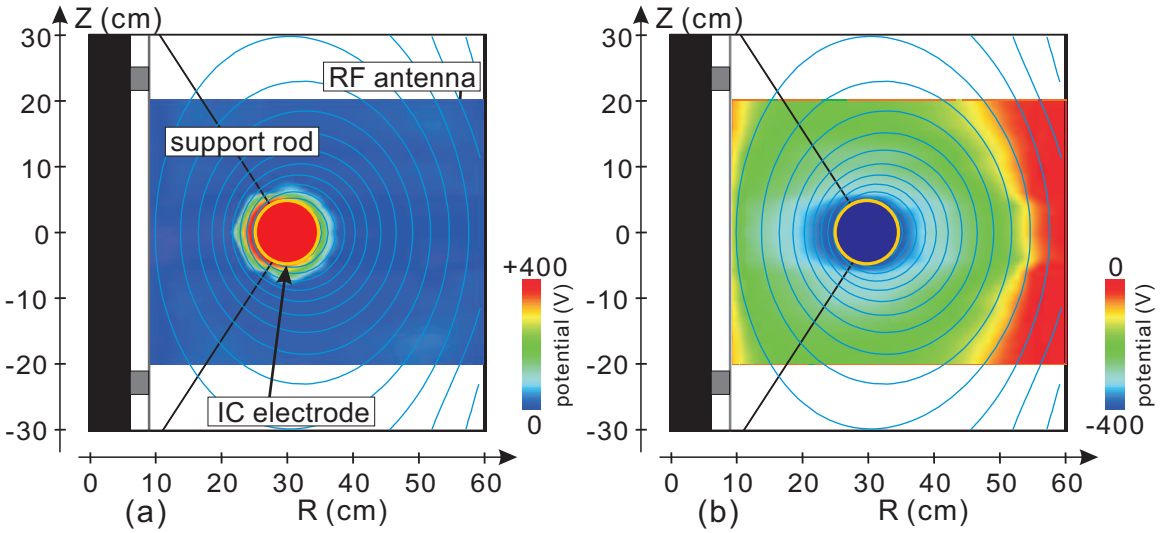

Figure 4.18: (color) Potential distribution of plasmas in the poloidal cross-section of the Proto-RT, (a) when the IC electrode was positively biased (V_{IC} = +400 V), and (b) negatively biased (V_{IC} = −400 V). Thin lines show the poloidal magnetic surfaces.

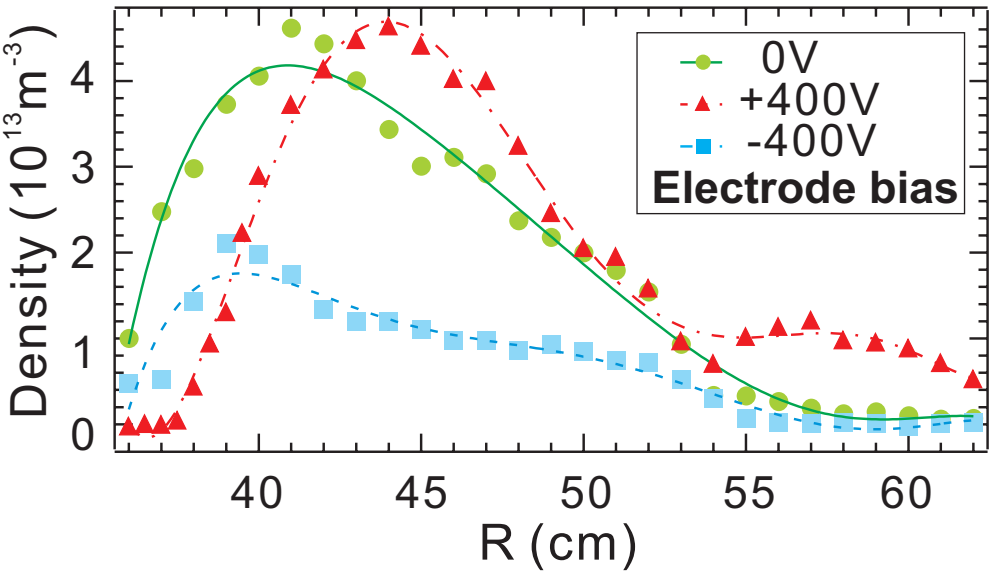

Figure 4.19: Radial electron density profiles.

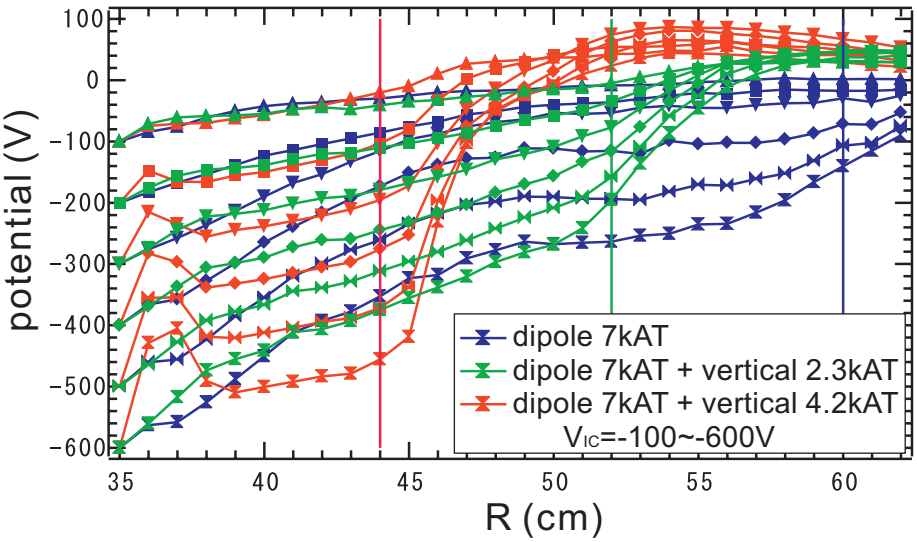

Figure 4.20: Potential structures and several magnetic surfaces.

the confinement region, steep potential gradient is observed near the last closed magnetic surfaces, indicating that the plasmas are confined in the last magnetic surfaces.

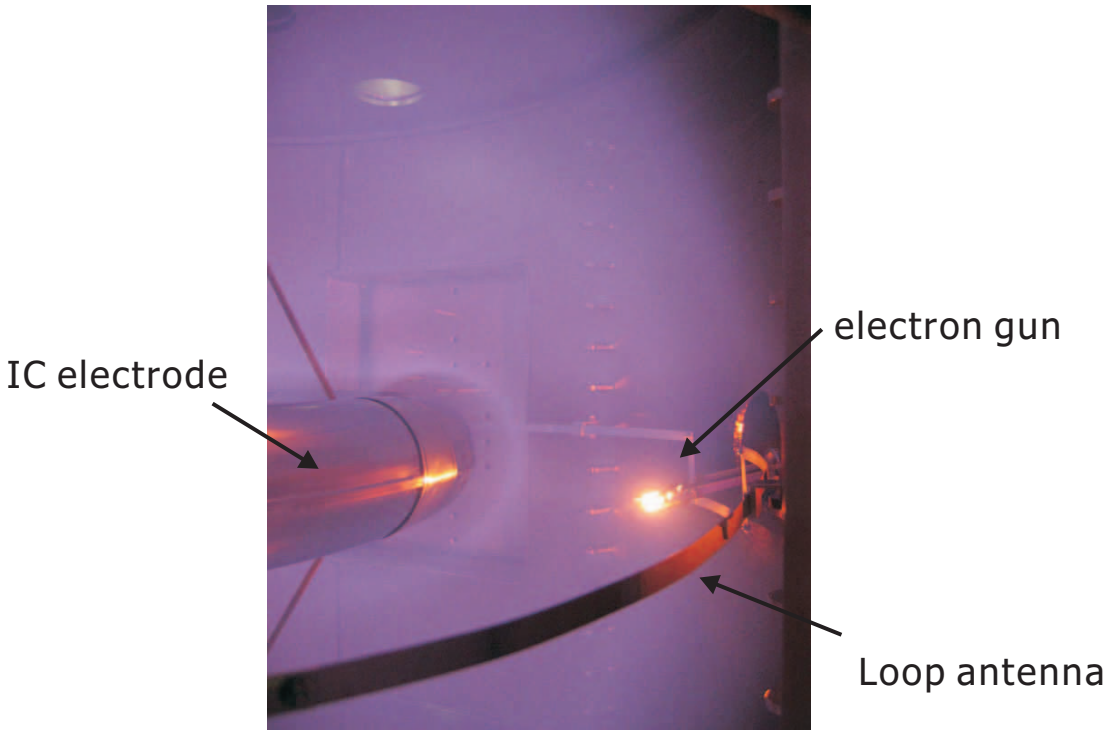

Figure 4.21: Hydrogen plasma generated by an loop (L-type) antenna and the electron gun located at peripheral region of the plasma.

4.3 Plasma bias by electron injection

4.3.1 Electron injection

An alternative way to generate electric field inside the plasma is to inject electrons from outside of the plasma. Compared with electrode biasing, it can reduce the contamination due to the sputtering or evaporation of the electrode, and it might also be advantageous to adopt to hot and dense plasmas. The electron injection experiment was carried out only with the use of L-type antenna, because the C-type antenna is a serious obstacle for the orbits of the injected electrons.

4.3.2 Profiles of space potentials

Figure 4.22 shows the potential profile of a plasma when electrons are injected into the plasma with an acceleration voltage of 1 kV and beam current of 0.2 A. Magnetic field is center null configuration of I_{IC} = 7 kAT and I_{VF} = 2.3 kAT, and the IC electrode is floating (terminated by a 100 MΩ probe). Although a small potential gradient was formed near the electron gun, the potential drop saturated around *zero* and the generated radial electric field remained less than 50 Vm^{-1}. Space potentials and effects of electron injection are shown in Fig. 4.23 in the variation

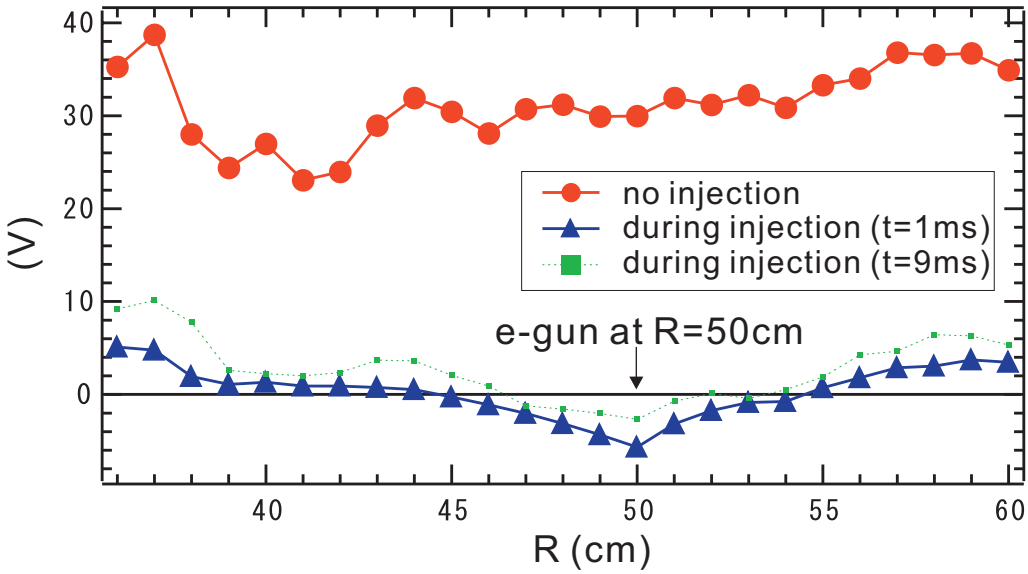

Figure 4.22: Potential profiles in the Proto-RT, with and without the electron injection. The gun is located at R=50 cm and Z=0.

of injected electron beam current. The increase of the acceleration voltage of the electron gun or heating current of the cathode (electron beam current of up to ~ 0.5 A and acceleration voltage of up tp 1.3 kV) does not contribute to form a large potential well inside the plasma.

4.3.3 Loss of electrons

The electron gun structure, located peripheral region of the plasma, could cause the loss of the injected electrons. In order to test the effects of the gun structure, X-point magnetic configuration [82] (I_{IC} = 7 kAT and I_{VF} = 2.3 kAT) was used and electrons are injected from outside of the closed magnetic surfaces. Figure 4.24 shows the radial potential profiles before and during the electron injection. Electrons are injected from (a) outside of the magnetic surfaces, (b) the X-point, and (c) inside the plasma. (Configuration of the magnetic surfaces and probe insertion at $Z = 0$ are shown in Figs. 2.5 and 2.3.) The radial shift of the electron gun does not significantly affect the potential structures in spite of the location of the electron gun. As shown in Fig. 4.25, the effects of the potential of the gun anode is also not related to the plasma potential formation, and thus it is not probable that the gun is the main obstacle for the potential formation.

Assuming that the observed potential drop of ~ 30 V is due to the injected electrons, the charge of the injected and trapped electrons is of the order of 10^{-7} C. From the injected beam current of ~ 1 A, the confinement time of electrons is estimated to be $\tau_e \sim 0.1\,\mu$s. In pure electron experiments in Proto-RT, obtained maximum electron confinement time is $\tau_{pe} \sim 100$ ms and it is much larger than τ_e. Space potential of the plasma and V_{IC}, when electrons are injected into a vacuum (no RF

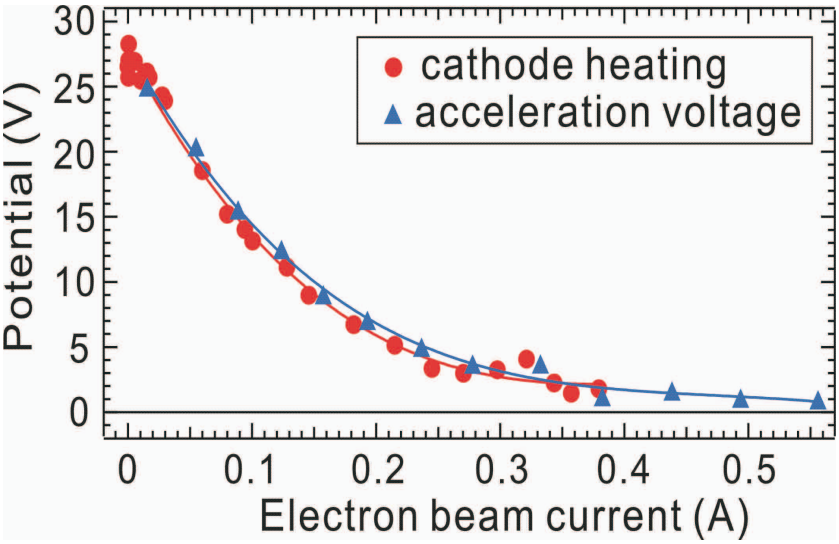

Figure 4.23: Space potential at $R = 40$ cm in the variation of electron injection current. Two curves are the functions of cathode heating current (while acceleration voltage $V_{\rm acc} = 1000$ V= *const.*) and $V_{\rm acc}$ ($I_{\rm fil} = 27$ A=*const.*).

plasmas) vessel, are shown in Fig. 4.26. The absolute values of the space potentials are decreasing function of neutral gas pressure, and no net potential is generated above $P \sim_0 = 5 \times 10^{-5}$ Torr. However, the threshold value show some dispersion due to the effects other than neutral pressures (the difference in Fig. 4.26 (a) and (b) is $V_{\rm IC}$), and it is set by the conditions for the maintenance of plasma discharge, indicating that the trapped electrons cannot coexist with neutral plasmas. In the electrode bias experiment, the electrode is almost axisymmetric, and direction of the plasma current is also aligned in the radial direction. In the present electron gun bias, the direction of the electron motion is not inevitably in the radial direction, and it is possible that the electron beam current does not effectively sustain the radial electric field.

4.4 Summary

The effects of electrode biasing and electron injection into a plasma were examined in an internal conductor device Proto-RT. When the ring electrode was biased, both the electrode current and internal electric fields of the plasmas showed a strong asymmetry according to the polarity of the electrode bias voltage. By using a negatively biased ring electrode, radial electric field of up to ~ 2 kVm^{-1} was generated, and it is consistent with the radial current due to the transport of ions by the collisions with neutral atoms. The corresponding $\mathbf{E} \times \mathbf{B}$ toroidal drift speed is comparable to the ion sound speed. In the experiments of electron injection, potential gradient was not effectively generated due to the electron loss possibly via RF plasmas.

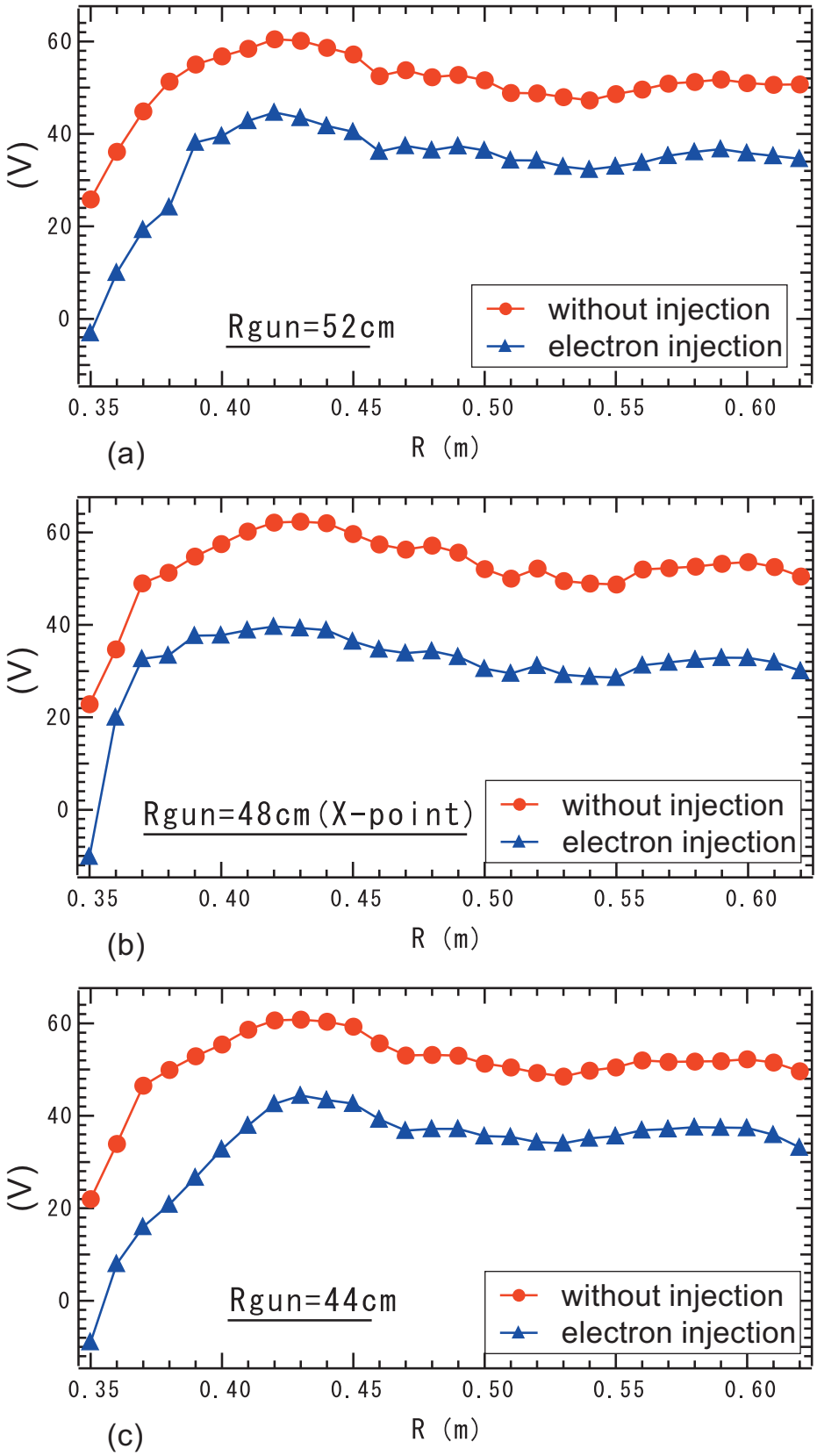

Figure 4.24: Potential profiles during electron injection in X-point magnetic configuration.

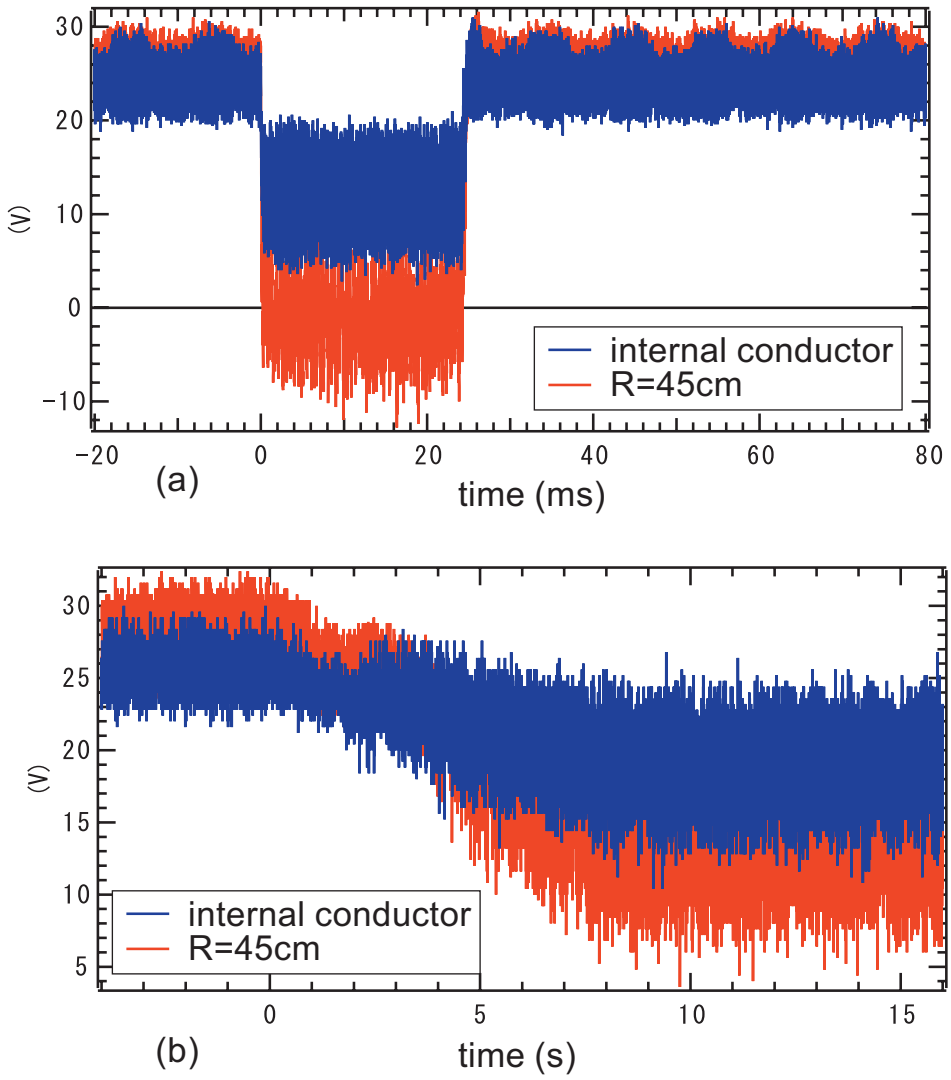

Figure 4.25: Space potential and V_{IC} with cathode bias. The cathode is biased against the vessel wall while the anode is floating. (a) Bias voltage of $V_B = -1000$ V was applied for 24 ms and (a) V_B was gradually changed from 0 to 1200 V in 10 s.

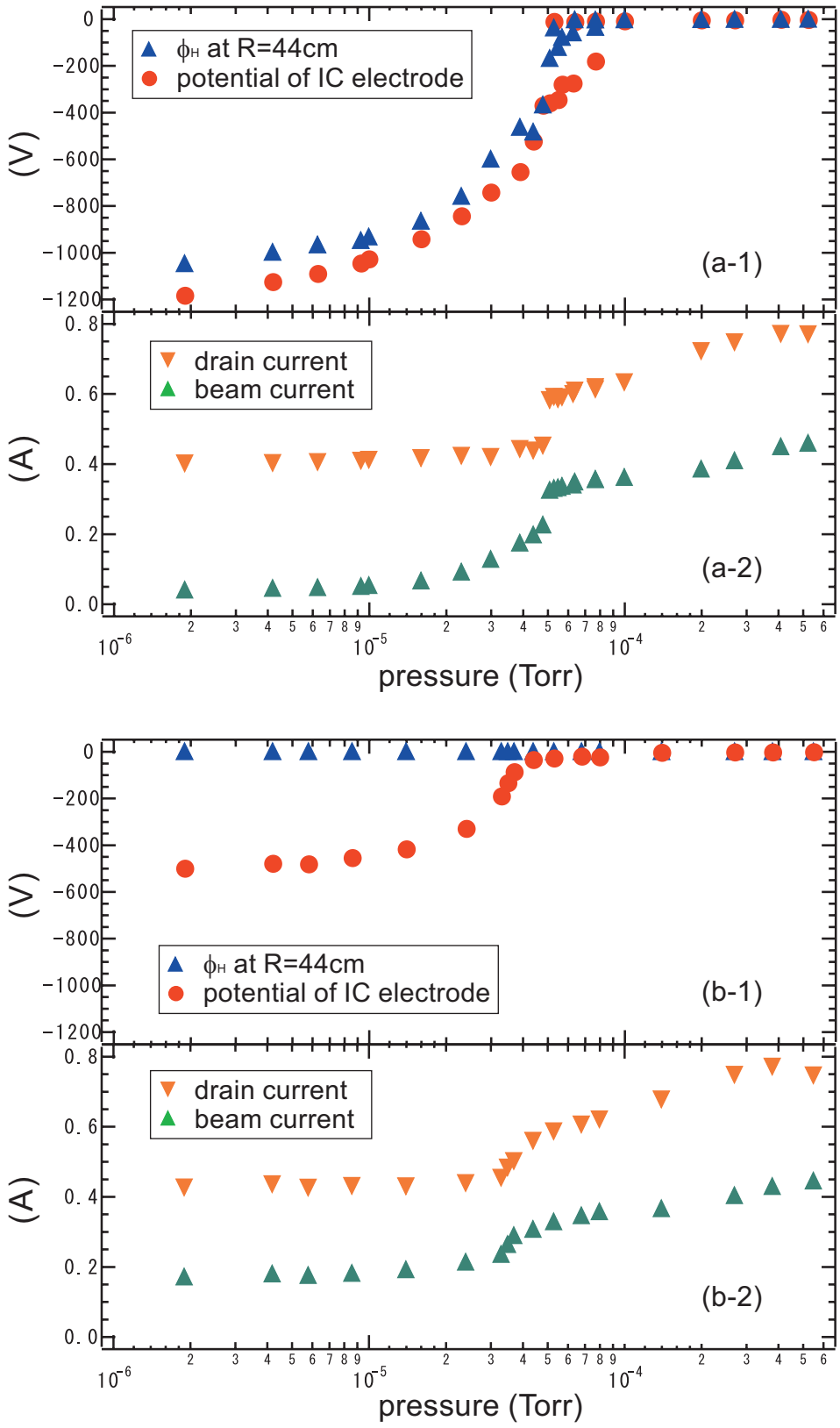

Figure 4.26: (a-1) (b-1) Electrostatic potentials generated by an electron gun as functions of background pressure and (a-2) (b-2) the drain and beam current of the electron gun, without the generation of RF plasmas. The IC electrode is (a) grounded and (b) floating.

Chapter 5

Conclusion

Proto-RT is the first step prototype device for the experimental investigation into the equilibrium and confinement properties of flowing non-neutral plasmas in a toroidal magnetic surface configuration. In order to understand the principle of the confinement of non-neutralized plasmas and control of plasma flow in an internal conductor system, in this study, basic properties of pure-electron and neutral plasmas were investigated with external electrostatic bias. The author took part in the experiments and mainly carried out the part of data acquisition and analysis of the obtained data. The experimental results are summarized as follows:

Long-term stable confinement of a toroidal electron plasma was demonstrated in a magnetic surface configuration. In the initial fluctuating phase, the trapped charge adjusts (diminishes) to enter a quiescent phase, when the potential contours are externally adjusted to the structure of magnetic surfaces. In the present device, we confined electrons with a peak density of an order of 10^{12} m^{-3} and total charge of an order of $\sim 10^{-8}$ C for more than 0.1 s. The confinement time is limited by the collisional effects of the electrons with the remaining neutral gas. The realized confinement configuration would be important as for the applications for the advanced traps of charged particles such as positron-electron plasmas, as well as for the understanding of physical mechanism of plasma equilibria.

In neutral plasma experiment, the effects of electrode biasing and electron injection into a plasma were examined in an internal conductor device Proto-RT. By using a negatively biased ring electrode, radial electric field of up to ~ 2 kVm^{-1} was generated in a broad region between the vessel wall and the electrode. The corresponding toroidal $\mathbf{E}\times\mathbf{B}$ drift speed $\sim 10^5$ ms^{-1} is comparable to the ion sound speed. In contrast, when electrons were injected into a plasma from an electron gun, potential gradient was not effectively generated, due to fast electron loss. Although electric field or flow was successfully generated in the plasma in the Proto-RT, the obtained plasma parameters still remain in an electrostatic range, due to the low electron density of $n_e \sim 10^{15}$ m^{-3}. The Alfvén velocity is two order of magnitude larger than the obtained drift speed of the plasma, v, and thus the effect of the dynamic pressure of plasma flow on β value is negligibly small. An

Machine parameters	magnetic field strength	B	0.01 T
	base pressure	P_{b}	4×10^{-7}Torr (1.4×10^{16} m^{-3})
	filling gas pressure	P_{n}	4×10^{-4}Torr (1.4×10^{19} m^{-3})
Electron plasma	Brillouin limit	n_{B}	5×10^{14} m^{-3}
	electron density	n_{e}	$\sim 1\times10^{12}$ m^{-3}
	(during electron injection)		$\sim 5\times10^{13}$ m^{-3}
	confinement time	τ	0.2 s
Hydrogen plasma	electron density	n_{e}	1×10^{15} m^{-3}
	ion sound speed	c_{s}	2×10^{4} ms^{-1}
	Alfvén velocity	v_{A}	7×10^{6} ms^{-1}
	toroidal flow velocity	v_{t}	2×10^{5} ms^{-1}

Table 5.1: Typical plasma parameters in Proto-RT experiments.

increase in the plasma density, possibly by means of another plasma generation method, will reduce the Alfvén velocity (e.g. plasma density $n_e = 10^{17}$ m^{-3} give a more realistic value of $v_A \sim 10^6$ ms^{-1}) and would make it possible to test the effects of plasma flow on the equilibria in future experiments.

Acknowledgments

I would like to express my deepest gratitude to Prof. YOSHIDA Zensho for his continuous and patient direction. It is great fortunate for me that I could have the opportunity to receive his guidance and generous advices on every occasion in the study and could have the chance to take part in the Proto-RT experiments under his guidance. I am exceedingly thankful for his hearty supervision in the past several years.

I am pleased to acknowledge the instructive guidance and kind encouragement of Prof. OGAWA Yuichi. I got helpful suggestions and hint from his advices at several points in the study. I am grateful to Prof. HIMURA Haruhiko for the guidance, hearty encouragement, and helpful advices on the study including many practical things concerning the experiments and electronics.

For the instructions especially in the experiments, on all about Proto-RT and electronics, I am thankful to Mr. MORIKAWA Junji. I also acknowledge Prof. FUKAO Masayuki for his hearty instructions and comprehensive advices on the diagnostics. All the experiments could never have been carried out without their accurate direction and advices. I also would like to express my gratitude to Dr. NIHEI Hitoshi and Dr. TATSUNO Tomoya for their kind instructions in seminars, advices on the experiments, and encouragement. I am grateful to Dr. OHSAKI Shuichi for the instructions on the thesis and useful advices on the study. I also thank Ms. TONEGAWA Nami for her help in the office works on my general student life.

I also would like to acknowledge Prof. BEREZHIANI Vazha, Prof. SHATASHVILI Nana, and Prof. SALEEM Hamid for their advices and encouragement during their stay in Tokyo.

I am grateful to the other members and former members of the laboratory: to Dr. KONDOH Shigeo for the instructions on the calculations and experiments, to Dr. NAKASHIMA Chihiro for his hearty and kind guidance on every practical thing concerning the experiments at Proto-RT as well as on the numerical calculations. In the use of computers and numerical calculations, I am deeply indebted to Dr. NUMATA Ryusuke. I also would like to thank Dr. VOLPONI Francesco, Dr. ITO Atsushi, and Dr. FURUKAWA Masaru for their help in the calculations as well as for the instructions and advices on the study. I would like to acknowledge the advices on the experiments and encouragement of Dr. OHKUNI Kohtaro. For helpful advices on the experiments during my first year in the Plasma Laboratory, especially for their instructions on electronics, I would like to thank Mr. YAGI Keita and Mr. OZAWA Daisaku. I am grateful to Mr. WAKABAYASHI Hidenori

for the useful discussions and instructions on electric circuits for the electron gun. I am thankful to Mr. HIROTA Makoto, Mr. HORI Dan, and Mr. SHIRAISHI Junya for their instructive advices on the study and encouragement. For the help in the experiments and several useful discussions, I am indebted to Mr. WATANABE Sho and Mr. GOTO Takuya.

This PhD study was carried out owing to the direction, instructions, and encouragement of the aforementioned staffs and students of the Plasma Laboratory and other persons, and I would cordially like to thank all of them for their invaluable attention.

Bibliography

[1] K. Miyamoto: *Plasma Physics for Nuclear Fusion, Second edition* (MIT Press, 1988).

[2] R. C. Davidson: *Physics of Nonneutral Plasmas* (Imperial College Press and World Scientific Publishing Company, London, 2001).

[3] W. Paul: "Electromagnetic traps for charged and neutral particles", Rev. Mod. Phys. **62**, 531 (1990).

[4] M. A. Lieberman and A. J. Lichtenberg: *Principles of Plasma Discharges and Material Processing* (A Wiley-Interscience Publishing, 1994).

[5] M. Amoretti, C. Amsler, G. Bonomi *et al.*: "Production and detection of cold antihydrogen atoms", Nature (London) **419**, 456 (2002).

[6] G. Gabrielse, N. S. Bowden, P. Oxley *et al.*: "Background-free observation of cold antihydrogen with field-ionization analysis of its states", Phys. Rev. Lett. **89**, 213401 (2002).

[7] Y. Yamazaki: "Production of ultra slow antiprotons, its application to atomic collisions and atomic spectroscopy - ASACUSA project", Nucl. Instrum. Methods Phys. Res. B **154**, 174 (1999).

[8] T. M. O'Neil and D. H. E. Dubin: "Thermal equilibria and thermodynamics of trapped plasmas with a single sign of charge", Phys. Plasmas **5**, 2163 (1998).

[9] D. H. E. Dubin and T. M. O'Neil: "Trapped nonneutral plasmas, liquids, and crystals (the thermal equilibrium states)", Rev. Mod. Phys. **71**, 87 (1999).

[10] T. M. O'Neil: "Trapped plasmas with a single sign of charge", Phys. Today **54**, 24 (1999).

[11] A. Mohri, H. Higaki, H. Tanaka, Y. Yamazawa, M. Aoyagi, T. Yuyama, and T. Michishita: "Confinement of nonneutral spheroidal plasmas in multi-ring electrode traps", Jpn. J. Appl. Phys. **37**, 664 (1998).

[12] F. Anderegg, E. M. Hollmann, and C. F. Driscoll: "Rotating field confinement of pure electron plasmas using Trivelpiece-Gould modes", Phys. Rev. Lett. **81**, 4875 (1998).

[13] G. Gabrielse, X. Fei, K. Helmerson, S. L. Rolston, R. Tjoelker, and T. A. Trainor, H. Kalinowsky, J. Haas, and W. Kells : "First capture of antiprotons in a Penning trap: a kiloelectronvolt source", Phys. Rev. Lett. **57**, 2504 (1986).

[14] C. M. Surko, M. Leventhal, and A. Passner: "Positron plasma in the laboratory", Phys. Rev. Lett. **62**, 901 (1989).

[15] R. G. Greaves, M. D. Tinkle, and C. M. Surko: "Creation and uses of positron plasmas", Phys. Plasmas **1**, 1439 (1994).

[16] R. G. Greaves and C. M. Surko: "An electron-positron beam-plasma experiment", Phys. Rev. Lett. **75**, 3846 (1995).

[17] S. J. Gilbert, D. H. E. Dubin, R. G. Greaves, and C. M. Surko: "An electron-positron beam-plasma instability", Phys. Plasmas **8**, 4982 (2001).

[18] R. G. Greaves and C. M. Surko: "Antimatter plasmas and antihydrogen", Phys. Plasmas **4**, 1528 (1997).

[19] G. Gabrielse, D. S. Hall, T. Roach, P. Yesley, A. Khabbaz, J. Estrada, C. Heimann, and H. Kalinowsky: "The ingredients of cold antihydrogen: Simultaneous confinement of antiprotons and positron at 4 K", Phys. Lett. B **455**, 311 (1999).

[20] F. F. Chen: *Plasma Physics for Nuclear Fusion, Second edition* (Plenum Press, 1984).

[21] M. Inutake, T. Cho, M. Ichimura *et al.*: "Thermal barrier formation and plasma confinement in the axisymmetrized tandem mirror GAMMA 10", Phys. Rev. Lett. **55**, 939 (1985).

[22] A. Tsushima, T. Mieno, M. Oertl, R. Hatakeyama, and N. Sato: "Control of radial potential profile and nonambipolar ion transport in an electron cyclotron resonance mirror plasma", Phys. Rev. Lett. **56**, 1815 (1986).

[23] R. F. Ellis, A. B. Hassam, S. Messer, and B. R. Osborn: "An experiment to test centrifugal confinement for fusion", Phys. Plasmas **8**, 2057 (2001).

[24] A. B. Hassam and Y. Huang: "Thermoelectric rotating torus for fusion", Phys. Rev. Lett. **91**, 195002 (2003).

[25] J. Ghosh, R. C. Elton, H. R. Friem, A. Case, R. Ellis, A. B. Hassam, S. Messer, and C. Teodorescu: "Spectroscopic measurements of plasma rotation and ion and neutral atom temperatures in the Meryland centrifugal experiment", Phys. Plasmas **11**, 3813 (2004).

[26] P. M. Valanju and S. M. Mahajan: “Topological symmetry breaking and topological symmetry breaking and creation of magneto Bernoulli creation of magneto Bernoulli states”, Bull. Am. Phys. Soc. **48**, 168 (2003).

[27] J. Fajans: “Non-neutral plasma equilibria, trapping, separatrices, and separatrix crossing in magnetic mirrors”, Phys. Plasmas **10**, 1209 (2003).

[28] E. Gilson and J. Fajans: “Quadrupole induced resonant particle transport in a pure-electron plasma”, Phys. Rev. Lett. **90**, 015001 (2003).

[29] J. Fajans and A. Schmidt: “Malmberg-Penning and minimum-B trap compatibility: the advantages of higher order multipole traps”, Nucl. Instrum. Methods Phys. Res. A **521**, 318 (2004).

[30] A. Mohri and Y. Yamazaki: “A possible new scheme to synthesize antihydrogen and to prepare a polarized antihydrogen beam”, Europhys. Lett. **63**, 207 (2003).

[31] G. S. Janes: “Experiments on magnetically produced and confined electron clouds”, Phys. Rev. Lett. **15**, 135 (1965).

[32] J. D. Daugherty and R. H. Levy: “Equilibrium of electron clouds in toroidal magnetic fields”, Phys. Fluids **10**, 155 (1967).

[33] J. D. Daugherty, L. Grodzins, G. S. Janes, and R. H. Levy: “New source of highly stripped heavy ions”, Phys. Rev. Lett. **20**, 369 (1968).

[34] R. H. Levy, J. D. Daugherty, and O. Buneman: “Ion resonance instability in grossly non-neutral plasmas”, Phys. Fluids **12**, 2616 (1969).

[35] J. D. Daugherty, J. E. Eninger, and G. S. Janes: “Experiments on the injection and containment of electron clouds in a toroidal apparatus”, Phys. Fluids **12**, 2677 (1969).

[36] J. Benford, B. Ecker, and V. Bailey: “Injection and control of intense relativistic electron beams in a torus”, Phys. Rev. Lett. **33**, 574 (1974).

[37] P. Gilad, B. R. Kusse, and T. R. Lockner: “Trapping of intense relativistic electron beams in toroidal geometry”, Phys. Rev. Lett. **33**, 1275 (1974).

[38] A. Mohri, M. Masuzaki, T. Tsuzuki, and K. Ikuta: “Formation of a non-neutral relativistic-electron-beam ring in a toroidal magnetic field”, Phys. Rev. Lett. **34**, 574 (1975).

[39] W. Clark, P. Korn, A. Mondelli, and N. Rostoker: “Experiments on electron injection into a toroidal magnetic field”, Phys. Rev. Lett. **37**, 592 (1976).

[40] K. Avinash: "On toroidal equilibrium of non-neutral plasma", Phys. Fluids B **3**, 3226 (1991).

[41] P. I. John: "Physics of toroidal electron clouds", Plasma Phys. Control. Fusion **34**, 2053 (1992).

[42] P. Zaveri, P. I. John, K. Avinash, and P. K. Kaw: "Low-aspect-ratio toroidal equilibria of electron clouds", Phys. Rev. Lett. **68**, 3295 (1992).

[43] S. S. Khirwadkar, P. I. John, K. Avinash, A. K. Agarwal, and P. K. Kaw: "Steady state formation of a toroidal electron cloud", Phys. Rev. Lett. **71**, 4334 (1993).

[44] M. R. Stoneking, P. W. Fontana, R. L. Sampson, and D. J. Thuecks: "Electron plasmas in a "partial" torus", Phys. Plasmas, **9**, 766 (2002).

[45] M. R. Stoneking, P. W. Fontana, R. L. Sampson, and D. J. Thuecks: "Electron plasma confinement in a partially toroidal trap", in *Non-Neutral Plasma Physics IV* (AIP Conference Proceedings Volume **606**, 2002), 671.

[46] M. R. Stoneking, M. A. Growdon, M. L. Milne, and R. T. Peterson: "Millisecond confinement and observation of the m=1 diocotron mode in a toroidal electron plasma", in *Non-Neutral Plasma Physics V* (AIP Conference Proceedings Volume **692**, 2003), 310.

[47] M. R. Stoneking, M. A. Growdon, M. L. Milne, and R. T. Peterson: "Poloidal $\mathbf{E}\times\mathbf{B}$ drift used as an effective rotational transform to achieve long confinement time in a toroidal electron plasma", Phys. Rev. Lett. **92**, 095003 (2004).

[48] L. Turner: "Brillouin limit for non-neutral plasma in inhomogeneous magnetic fields", Phys. Fluids B **3**, 1355 (1991).

[49] L. Turner and D. C. Barns: "Brillouin limit and beyond: a route to inertial-electrostatic confinement of a single-species plasma", Phys. Rev. Lett. **70**, 798 (1993).

[50] T. M. O'Neil and R. A. Smith: "Stability theorem for a single species plasma in a toroidal magnetic configuration", Phys. Plasmas **1**, 2430 (1994).

[51] S. M. Crooks and T. M. O'Neil: "Transport in a toroidally confined pure electron plasma", Phys. Plasmas **3**, 2533 (1997).

[52] Z. Yoshida *et al.*: "Toroidal magnetic confinement of non-neutral plasmas", H. Himura *et al.*: "Confinement of nonneutral plasmas in the Prototype Ring Trap device", C. Nakashima *et al.*: "Experiments on pure electron plasma confined in a toroidal geometry", Y. Ogawa *et*

al.: “Design of a toroidal plasma confinement device with a levitated super-conducting internal coil”, in *Non-Neutral Plasma Physics III*, edited by John J. Bollinger, Ross L. Spencer, and R. C. Davidson (American Institute of Physics Conference Proceedings Volume **498**, New York, 1999), 397.

[53] Z. Yoshida *et al.*: “Relaxed states in plasmas: non-neutral and diamagnetic plasmas”, H. Himura *et al.*: “Proposed non-neutralized two-fluid plasma experiment”, H. Himura *et al.*: “Flowing electron plasmas as modified current source”, C. Nakashima *et al.*: “Injection of electrons into a toroidal trap using chaotic orbits near magnetic null”, Y. Ogawa *et al.*: “Design of a toroidal device with a high temperature superconductor coil for non-neutral plasma trap”, in *Non-Neutral Plasma Physics IV*, edited by F. Anderegg, L. Schweikhard, and C. F. Driscoll (American Institute of Physics Conference Proceedings Volume **606**, New York, 2002), 641.

[54] T. S. Pedersen and A. H. Boozer: “Confinement of nonneutral plasmas on magnetic surfaces”, Phys. Rev. Lett. **88**, 205002 (2002).

[55] T. S. Pedersen: “Numerical investigation of two-dimensional pure electron plasma equilibria on magnetic surfaceds”, Phys. Plasmas **20**, 334 (2003).

[56] T. S. Pedersen, A. H. Boozer, J. P. Kremer, and R. Lefrancois: “Confinement of plasmas of arbitrary neutrality in a stellarator”, Phys. Plasmas **11**, 2377 (2004).

[57] T. S. Pedersen, J. P. Kremer, and A. H. Boozer: “Confinement of non-neutral plasmas in the Columbia Non-neutral Torus experiment”, in *Non-Neutral Plasma Physics V* (AIP Conference Proceedings Volume **692**, 2003), 302.

[58] J. P. Kremer, T. S. Pedersen, N. Pomphrey, W. Reiersen, and F. Dahlgren: “The status of the design and construction of the Columbia Non-neutral Torus”, in *Non-Neutral Plasma Physics V* (AIP Conference Proceedings Volume **692**, 2003), 320.

[59] T. S. Pedersen, A. H. Boozer, W. Dorland, J. P. Kremer, and R. Schmitt: “Prospects for the creation of positron-electron plasmas in a non-neutral stellarator”, J. Phys. B: At. Mol. Opt. Phys. **36**, 1029 (2003).

[60] A. H. Boozer: “Stability of pure electron plasmas on magnetic surfaces”, Phys. Plasmas **11**, 4709 (2004).

[61] H. Himura, H. Wakabayashi, M. Fukao, and CHS group: “Experimental investigation of helical non-neutral plasmas”, in *Non-Neutral Plasma Physics V* (AIP Conference Proceedings Volume **692**, 2003), 293.

[62] H. Wakabayashi, H. Himura, M. Fukao, and Z. Yoshida: "Parameter dependence of inward diffusion on injected electrons in helical non-neutral plasmas", in *Non-Neutral Plasma Physics V* (AIP Conference Proceedings Volume **692**, 2003), 332.

[63] H. Himura, H. Wakabayashi, M. Fukao *et al.*: "Observation of collisionless inward propagation of electrons into helical vacuum magnetic surfaces via stochastic magnetic fields", Phys. Plasmas **11**, 492 (2004).

[64] H. Himura, H. Wakabayashi, M. Fukao, M. Isobe, S. Okamura, H. Yamada,: "Experiments on injecting electrons into helical magnetic field configuration", IEEE Trans. Plasma Sci. **32**, 510 (2004).

[65] S. M. Mahajan and Z. Yoshida: "Double curl Beltrami flow: diamagnetic structure", Phys. Rev. Lett. **81**, 4863 (1998).

[66] Z. Yoshida and S. M. Mahajan: "Variational principles and self-organization in two-fluid plasmas", Phys. Rev. Lett. **88**, 095001 (2002).

[67] L. C. Steinhauer and A. Ishida: "Relaxation of a two-specie magnetfluid", Phys. Rev. Lett. **79**, 3423 (1997).

[68] H. Y. Guo, A. L. Hoffman, K. E. Miller, and L. C. Steinhauer: "Flux conversion and evidence of relaxation in a high-β plasma formed by high-speed injection into a mirror confinement structure", Phys. Rev. Lett. **92**, 245001 (2004).

[69] S. Ohsaki: "Hall effect on relaxation process of flowing plasmas", Phys. Plasmas **12**, 032306 (2005).

[70] S. Ohsaki: "Hall effect on equilibrium, stability and wave spectrum of magnet-fluid plasmas", PhD thesis, Department of Advanced Energy, Graduate School of Frontier Sciences, University of Tokyo (2004).

[71] F. Wagner, G. Becker, K. Behringer *et al.*: "Regime of improved confinement and high beta in neutral-beam-heated divertor discharges of the ASDEX tokamak", Phys. Rev. Lett. **49**, 1408 (1982).

[72] R. J. Taylor, M. L. Brown, B. D. Fried *et al.*: "*H*-mode behavior induced by cross-field currentsin a tokamak", Phys. Rev. Lett. **63**, 2365 (1989).

[73] V.Erckmann, F. Wagner, J. Baldzuhn *et al.*: "*H* mode of the W 7-AS stellarator", Phys. Rev. Lett. **70**, 2086 (1993).

[74] N. Ohyabu, K. Narihara, H. Funaba *et al.*: "Edge thermal transport barrier in LHD discharges", Phys. Rev. Lett. **84**, 103 (2000).

[75] S. Inagaki, S. Kitajima, M. Takayama, E. Nakamura, T. Yoshida, and H. Watanabe: "Influence of biased electrode on plasma confinement in the Tohoku University Heliac", Jpn. J. Appl. Phys. **36**, 3697 (1997).

[76] M. Okabayashi and S. Yoshikawa: "Measurement of the dc plasma electric resistivity perpendicular to the magnetic surface", Phys. Rev. Lett. **29**, 1725 (1972).

[77] A. Hasegawa: "A dipole field fusion reactor", Comments Plasma Phys. Contr. Fusion **11**, 147 (1987).

[78] A. Hasegawa, L. Chen, and M. Mauel: "A D-^{3}He fusion reactor based on a dipole magnetic field", Nucl. Fusion **31**, 125 (1991).

[79] S. Kondoh and Z. Yoshida: "Toroidal magnetic confinement of non-neutral plasma", Nucl. Instrum. Meth. Phys. Res. A **382**, 561 (1996).

[80] S. Kondoh: "Application of magnetic separatrix for a charged-particle trap using an internal conductor", Master's thesis, Department of Quantum Engineering and System Sciences, Graduate School of Engineering, University of Tokyo (1997).

[81] C. Nakashima and Z. Yoshida: "Application of RF electric field to a charged-particle trap in toroidal geometry", Nucl. Instrum. Meth. Phys. Res. A **428**, 284 (1998).

[82] C. Nakashima, Z. Yoshida, H. Himura, M. Fukao, J. Morikawa, and H. Saitoh: "Injection of electron beam into a toroidal trap using chaotic orbits near magnetic null", Phys. Rev. E **65**, 036409 (2002).

[83] C. Nakashima: "Development of a method for producing toroidal non-neutral plasmas", PhD thesis, Department of Quantum Engineering and System Sciences, Graduate School of Engineering, University of Tokyo (2002).

[84] H. Saitoh *et al.*: "Long-time confinement of toroidal electron plasmas in Proto-RT", in *Non-Neutral Plasma Physics V*, edited by M. Schauer, T. Mitchell, and R. Nebel (American Institute of Physics Conference Proceedings Volume **692**, New York, 2003), 293.

[85] S. Kondoh, T. Tatsuno, and Z. Yoshida: "Stabilization effect of magnetic shear on the diocotron instability", Phys. Plasmas **8**, 2635 (2001).

[86] T. Uchida: "Application of radio-frequency discharged plasma produced in closed magnetic neutral line for plasma processing", Jpn. J. Appl. Phys. **33**, L43 (1994).

[87] H. Asakura, K. Takemura, Z. Yoshida, and T. Uchida: "Collisionless heating of electrons by meandering chaos and its application to a low-pressure plasma source", Jpn. J. Appl. Phys. **36**, L4493 (1997).

[88] Z. Yoshida, H. Asakura, H. Kakuno, J. Morikawa, K. Takemura, S. Takizawa, and T. Uchida: "Anomalous resistance induced by chaos of electron motion and its application to Plasma Production", Phys. Rev. Lett. **81**, 2458 (1998).

[89] H. Saitoh, Z. Yoshida, and C.Nakashima: "Equilibrium of a non-neutral plasma in a toroidal magnetic shear configuration", Rev. Sci. Instrum. **73**, 87 (2002).

[90] H. Saitoh, Z. Yoshida, H. Himura, J. Morikawa, and M. Fukao: "Potential structure of a plasma in an internal conductor device under the influence of a biased electrode", Phys. Plasmas **11**, 3331 (2004).

[91] H. Saitoh, Z. Yoshida, C. Nakashima, H. Himura, J. Morikawa, and M. Fukao: "Confinement of pure-electron plasmas in a toroidal magnetic-surface configuration", Phys. Rev. Lett. **92**, 255005 (2004).

[92] H. Saitoh, Z. Yoshida, and S. Watanabe: "Stable confinement of toroidal electron plasma in an internal conductor device Proto-RT", submitted to Phys. Plasmas.

[93] A. J. Peurrung, J. Notte, and J. Fajans: "Observation of the ion resonance instability", Phys. Rev. Lett. **70**, 295 (1993).

[94] J. Fajans: "Transient ion resonance instability", Phys. Fluids B **5**, 3127 (1993).

[95] J. H. Malmberg and C. F. Driscoll: "long-time confinement of a pure electron plasma", Phys. Rev. Lett. **44**, 654 (1980).

[96] H. M. Mott-Smithand I. Langmuir: "The theory of collectors in gaseous discharges", Phys. Rev. **28**, 727 (1926).

[97] F. F. Chen: "Electric Probe", in *Plasma Diagnostic Technique*, (Academic Press Inc., 1991).

[98] N. Hershkowitz: "How Langmuir Probe Work", in *Plasma Diagnostics - Discharge Parameters and Chemistry* (Academic Press Inc., 1989).

[99] H. Himura, C. Nakashima, H. Saitoh, and Z. Yoshida: "Probing of flowing electron plasmas", Phys. Plasmas **8**, 4651 (2001).

[100] H. Himura, C. Nakashima, H. Saitoh, Z. Yoshida, J. Morikawa, and M. Fukao: "Flowing electron plasmas as modified current source", in *Non-Neutral Plasma Physics IV* (AIP Conference Proceedings Volume **606**, 2002), 661.

[101] R. F. Kemp and J. M. Sellen, Jr.: “Plasma potential measurements by electron emissive probes”, Rev. Sci. Instrum. **37**, 455 (1966).

[102] J. R. Smith, N. Hershkowitz, and P. Coakley: “Inflection-point method of interpreting emissive probe characteristics”, Rev. Sci. Instrum. **50**, 210 (1979).

[103] U. Flender, B. H. N. Thi, K. Wiesemann, N.A. Khromov, and N. B. Kolokolov: “RF harmonicsuppression in Langmuir probe measurements in RF discharges”, Plasma Sources Sci. Technol. **5**, 61 (1996).

[104] M. Y. Ye and S. Takamura: “Effect of space-charge limited emission on measurements of plasma potential using emissive probes”, Phys. Plasmas **7**, 3457 (2000).

[105] K. Ura *et al.*: “*Electron and Ion Beam Handbook*”, (in Japanese, Nikkan Kogyo Shimbun Co., Tokyo, 1998).